1992

Magnetic properties of high-T[subscript c] superconductors

Junho Gohng
Iowa State University

Order Number 9223928

Magnetic properties of high-T_c superconductors

Gohng, Junho, Ph.D.

Iowa State University, 1992

U·M·I
300 N. Zeeb Rd.
Ann Arbor, MI 48106

Magnetic properties of high-T_c superconductors

by

Junho Gohng

A Dissertation Submitted to the

Graduate Faculty in Partial Fulfillment of the

Requirements for the Degree of

DOCTOR OF PHILOSOPHY

Department: Physics and Astronomy
Major: Solid State Physics

Approved:

Signature was redacted for privacy.

In Charge of Major Work

Signature was redacted for privacy.

For the Major Department

Signature was redacted for privacy.

For the Graduate College

Iowa State University
Ames, Iowa

1992

TABLE OF CONTENTS

CHAPTER 1. INTRODUCTION

A series of studies have been carried out in this research, in an effort to broaden the understanding of the magnetic properties of high-T_c superconductors, in the areas of reversible magnetization, free energy and flux creep. These properties represent characteristics of superconductors at various regions on the H-T plane, as discussed later in this chapter (Section 1.2).

Although the term "superconductor" may have come from the zero electrical resistance of the superconducting materials, superconductors have intrigued many for their unique magnetic properties. Perfect diamagnetism is one of the most fundamental properties of these materials. Especially, with the discovery of high-T_c superconductors, magnetic properties of these new materials have been extensively studied lately.

Due to the extreme type-II ($\kappa >> 1$, where κ is the Ginzburg-Landau parameter) nature of these high-T_c materials, their behaviors in the magnetic fields are often classified into three categories according to the intensities of applied fields: the low field ($H < H_{c1}$), the high field ($H > H_{c2}$), and the intermediate field ($H_{c1} << H << H_{c2}$) regions. Since for most of high-T_c superconductors the upper critical field H_{c2} ranges at hundreds of tesla and the lower critical field H_{c1} at 1 % of tesla range, and since it is experimentally difficult to (if not impossible) to access H_{c2} area of magnetic field for these materials except for the temperature in the vicinity of T_c, the magnetic properties in the intermediate field region have become the area of prime interest. This category also includes the area of reversible magnetization where valuable information regarding critical fields and

some of the other basic parameters like κ and λ can be calculated from magnetization data.

Most of high-T_c materials exhibit pinning behavior due to the defects, such as impurities and inhomogeneity in the material, working as pinning sites. These defects interact with flux lines, in the mixed state, and introduce irreversible magnetization behavior. Flux creep (magnetic relaxation) is an interesting example of the irreversible magnetization behavior.

The outline of this dissertation is as following. In the first two chapters, historical background as well as some of the basic properties of superconductivity are reviewed, and some of the important theories related to the scope of this research is summarized. In chapter 3, experimental details including the sample preparations, grain alignment and grain size control is discussed. In chapter 4, the results for the four major subjects of this research is discussed. Specific conclusions are: (a) The rounding in M vs T curves is a reflection of thermodynamic fluctuation near T_c and gives the specific heat jump data which agrees with direct calorimetric measurements. (b) A comparison of grain-aligned small single crystals and melt-textured samples show same free energy and specific heat jump in spite of their quite different material structure and pinning strength. (c) Fitting the magnetization data to Hao-Clem model allows the derivation of the fundamental quantities such as order parameter and its field and temperature dependency as well as the critical fields. (d) The grain size effect on magnetization reduces the free energy as the average grain size D decreases, due to the role of twin spacing d which varies as $d \propto \sqrt{D}$.

1.1. A Brief Review of Superconductivity

The superconductivity was first discovered in mercury by Kammerlingh Onnes [Onnes, 1911] in the early 20th century, but until the recent discovery of oxide high-T_c superconductors, it was a strictly low temperature phenomenon. In spite of the continued searches and discoveries of numerous superconducting materials, the highest transition temperature of superconductors remained as low as 23.4 for the Nb_3Ge compound until the discovery of oxide superconductors. In 1986, J. G Bednorz and K. A. Müller [Bednorz and Müller, 1986] observed superconductivity in a lanthanum barium copper oxide at 35 K, and from this discovery the subject of high-T_c superconductivity has begun.

Two Types of Superconductors

After the discovery of superconductivity, Onnes observed that the superconductivity disappears if a sufficiently large current is applied through the conductor, or the sample is placed in a magnetic field above a certain value. The phase diagram for a typical simple type-I superconductor is shown in Fig. 1.1. Typical examples of type-I superconductors are single element superconductors like In, Pb, Sn, etc. It should be realized that superconductivity is not a rare phenomenon; about half the metallic elements fall in to the category of superconductors.

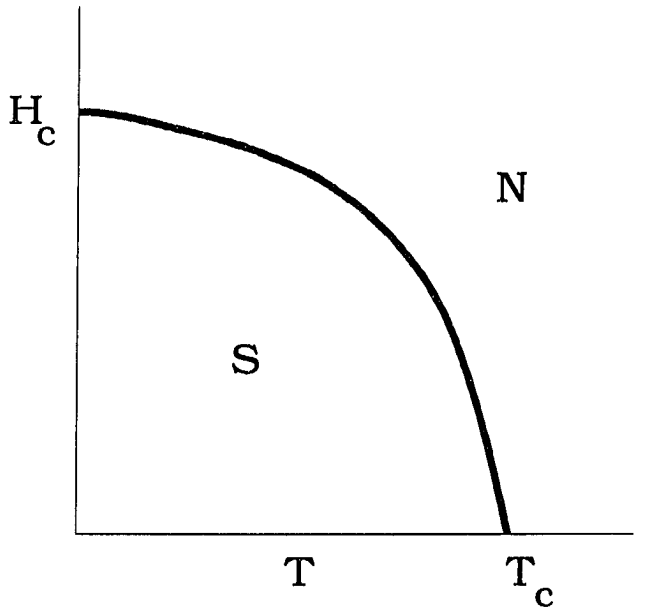

Fig. 1.1 Phase diagram of a type-I superconductor, showing (S) Superconducting and (N) Normal regions

22 years after the first discovery of superconductivity, Meissner and Ochsenfeld measured the flux distribution outside the superconductors (Pb and Sn) and found that the superconductors became perfectly diamagnetic. The flux is forced out of the interior of a superconductor, even if it had been cooled in a magnetic field [Meissner and Ochsenfeld, 1933]. This phenomenon, known as Meissner effect, distinguishes the superconductors as perfect diamagnetic materials rather than just perfect conductors, a term often used to classify superconductors before the discovery of Meissner effect. As shown in Fig 1.1, type-I superconductors exhibit the perfect Meissner effect when the applied field is below the critical field H_c. The critical field is related to the free energy difference between the normal state and the superconducting state in zero field. Note that the values of H_c approaches zero in a continuous fashion. This reflects the fact that superconductivity is, in fact, a second order phase transition. A second order

transition has two important characteristics. First, at the transition there is no latent heat. Second, there is a jump in specific heat. Due to this reason, much of early studies and understandings in superconductivity have been derived from measurements of their specific heat.

Compared to type-I superconductors, a qualitatively different behavior is exhibited by type-II superconductors, as shown in Fig. 1.2. Type-II superconductors still show perfect diamagnetism or Meissner effect at sufficiently low field, where the field is screened from the interior of the material. Above a critical field (lower critical field), H_{c1}, however, there is a partial penetration of the field, while the material itself remains superconducting.

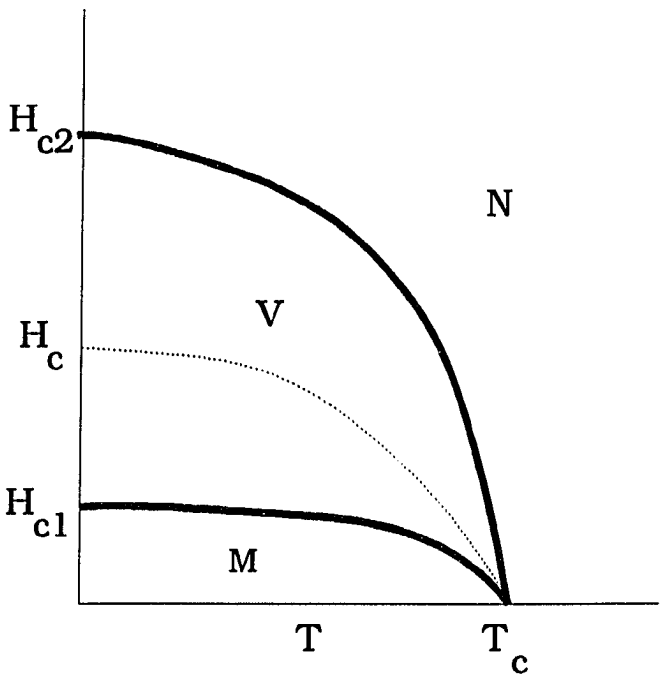

Fig. 1.2 Phase diagram for a type-II superconductor, showing the (M) Meissner, (V) Vortex or mixed state, (N) Normal regions

The field increasingly penetrates the material as the applied field gets increased, until finally the superconductivity is destroyed above the second critical field (upper critical field), H_{c2}. The magnetization vs applied curves of type-I and type-II superconductors are shown in Fig. 1.3. Unlike type-I superconductors, magnetization of a type-II superconductor does not drop to zero abruptly, but gradually decreases to zero as the field increases past H_{c1} and the flux lines move closer toward each other until the field reaches to H_{c2}. When the field is reduced the magnetization shows reversible properties for both ideal type-I and type-II superconductors, as in Fig. 1.3(a) and 1.3(b), respectively.

The basic mechanism responsible for the superconductivity is essentially the same for both type-I and type-II superconductors. The distinction lies in the spatial variation of two competing contributions to the free energy. The first is the magnetic contribution governed by λ, and the second is the condensation energy by ξ. As a result, however, the behavior in magnetic field is qualitatively quite different. It was Abrikosov who first showed that the magnetic behavior of a superconductor is controlled by the value of Ginzburg-Landau parameter $\kappa = \lambda/\xi$, where λ and ξ are London penetration depth and coherence length respectively [Abrikosov, 1957]. With his work, he predicted two uniquely different types of magnetic properties exists depending on κ values. According to the Ginzburg-Landau theory, a superconductor with $\kappa < 1/\sqrt{2}$ is classified as a type-I superconductor, and $\kappa > 1/\sqrt{2}$ as a type II superconductor.

For the type-II superconductors with $\kappa > 1/\sqrt{2}$, there exists a fairly wide magnetic field region of the mixed state (vortex state) where the surface energy between normal and superconducting states becomes negative. This is due to the normal state cores, or magnetic fluxes, that exist in forms of isolated filaments

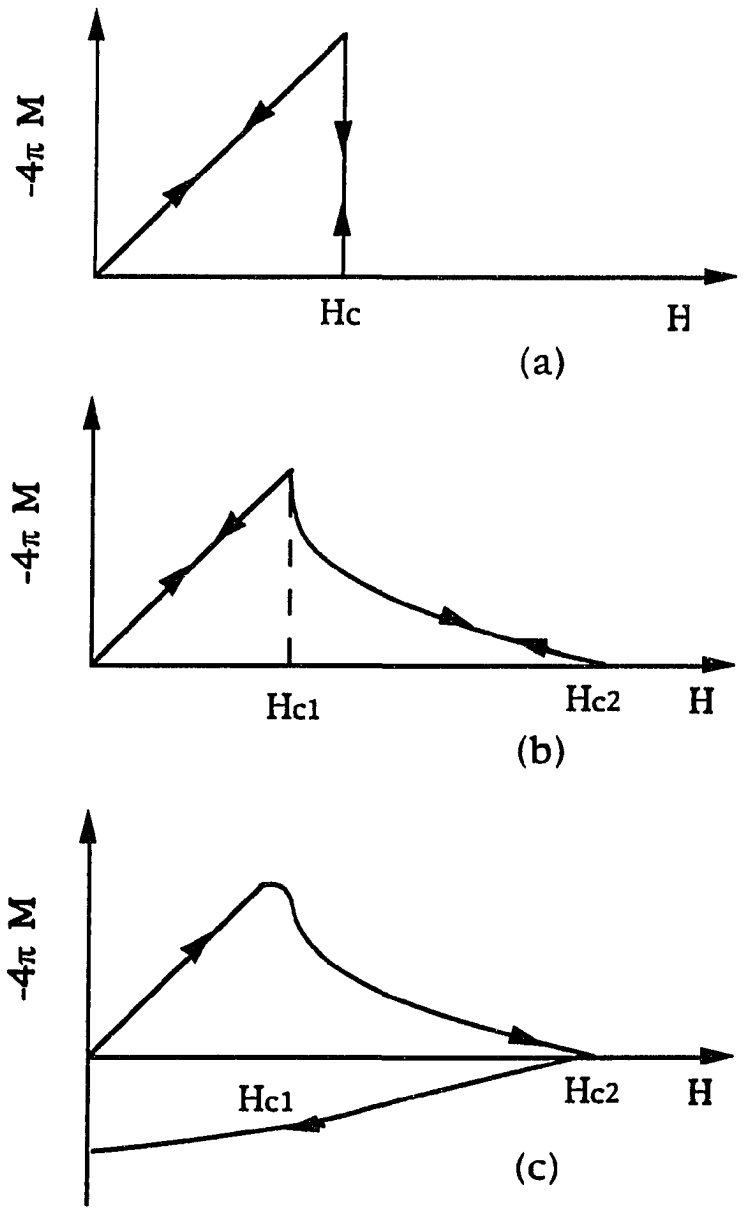

Fig. 1.3 Magnetization vs. applied fields for (a) type I, (b) ideal type II, and (c) non-ideal type II (hard) superconductors.

called fluxoids, flux line, or vortex along the direction of the applied field H that falls into the range of $H_{c1} < H < H_{c2}$. Fig. 1.4 shows the structure of an Abrikosov vortex. Each fluxoid contains the basic unit of one magnetic flux quantum $\Phi_o = hc/2e$. When a superconductor is placed in a magnetic field, the screening current which circulated to cancel the flux inside must flow within the surface layer. As a result, the magnetic flux density does not fall abruptly to zero at the boundary but dies away within the distance from the surface where the screening currents are flowing. This distance is called penetration depth. Likewise, for each vortex, the vortex current with a radius $\lambda(T)$ encircles each flux line as a result of a gradient of the local magnetic flux and the current interacts with the magnetic field produced by nearby vortices. This interaction results in flux line repelling each other and these flux lines eventually organize themselves in a triangular lattice, called as Abrikosov lattice. The lower critical field H_{c1} is related to λ by the relation

$$H_{c1} = \frac{\varphi_0}{4\pi\lambda^2}\ln\kappa \qquad (1.1)$$

The behavior of type-II superconductors in an applied field can be described as follows. At fields $H < H_{c1}$, a type-II superconductor exhibits the perfect diamagnetism, the energy of an isolated flux line being greater than the reduction in field energy that would occur if the flux line entered the superconductor. At fields greater than H_{c1}, flux lines begin to enter into the superconductor. The flux lines approach with increasing field and the equilibrium flux line density can be determined by the interactions between flux lines as they come together. At sufficiently high field the flux line cores eventually overlap and the

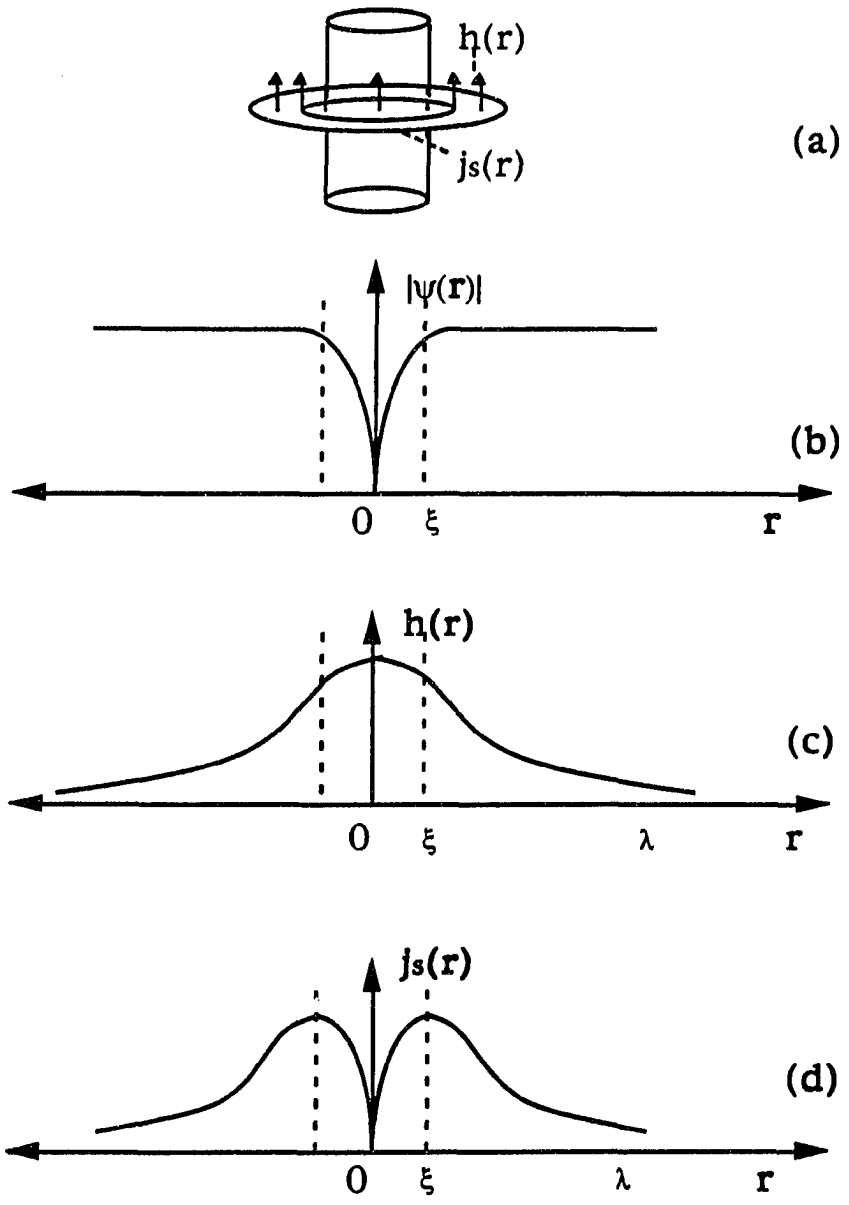

Fig. 1.4 Structure of an isolated Abrikosov vortex with $\kappa > 1/\sqrt{2}$, showing (a) a vortex, (b) wave function, (c) local magnetic field, and (d) supercurrent

superconductivity disappears when the order parameter is reduced to zero everywhere inside the superconductor. This field defines the upper critical field H_{c2}, and it is related to the coherence length ξ by

$$H_{c2} = \frac{\varphi_0}{2\pi\xi^2}. \qquad (1.2)$$

The flux lines exhibit some of the most unique properties of type-II superconductors, especially in the transport properties of these superconductors.

Non-ideal Superconductors and Flux Pinning

In real superconducting materials, there always are defects, in forms of impurities, inhomogeneities, etc. In many cases these defects work as pinning centers to pin the flux lines. The interaction between the pinning sites and flux lines also leads to the irreversible magnetization behavior. Since most of the superconductors have defects, these superconductors with pinning sites are called as non-ideal superconductors or hard superconductors as opposed to the ideal superconductors with no pinning sites.

Fig. 1.3(c) illustrates the magnetic behavior of an non-ideal superconductor. Compared to the rather sharp drop of magnetization near H_{c1} for an ideal superconductor, a non-ideal superconductor does not have a sharply defined lower critical field H_{c1}. Furthermore, the decreasing field follow different path from traced in the original increasing field. This magnetic hysteresis is a characteristic of a non-ideal superconductor. And when the applied field is reduced to zero, there remains some magnetization in the sample, showing the trapped flux. These characteristics of non-ideal superconductors do not

necessarily occur at the same time, however. Impurities and inhomogeneity in the sample tend to exhibit poorly defined lower critical field, while defects involving large number of atoms, such as particles of another substance or dislocations tend to give rise to hysteresis and trapped flux. These characteristics of non-ideal superconductors are of considerable importance in understanding the nature of superconductivity, and cover especially attractive areas in the studies of high-T_c superconductors.

Another important feature of non-ideal superconductors, especially in the area of applications, can be seen with an applied current. The pinning sites in the non-ideal superconductors cause the critical current J_c by hindering the displacement of vortex lines. In case of ideal type II superconductors, fields larger than H_{c1} nucleate vortices inside the sample, which move under the Lorentz force from an external current [Bardeen and Stephen, 1965]. This motion in the flux will create a voltage according to the Faraday's law and the zero resistance would be lost. In the non-ideal superconductors, however, as Anderson [Anderson, 1962; Anderson and Y. B. Kim, 1964] suggested, the critical current is reached only when the Lorentz force on the flux lines is balanced by the pinning force. Therefore, the critical current density becomes the extrinsic quantity determined mainly by the pinning properties of material. This is of great technological importance, because it is directly related to fabricating the high quality superconducting wire, and various ways of introducing most effective pinning to enhance J_c have been under study by many.

While magnetic hysteresis in superconductors was observed in 1930s [Keeley et al., 1934; de Haas and Casimir-Jonker, 1935], it took almost 30 years until its mechanism to irreversible magnetization was successfully explained by

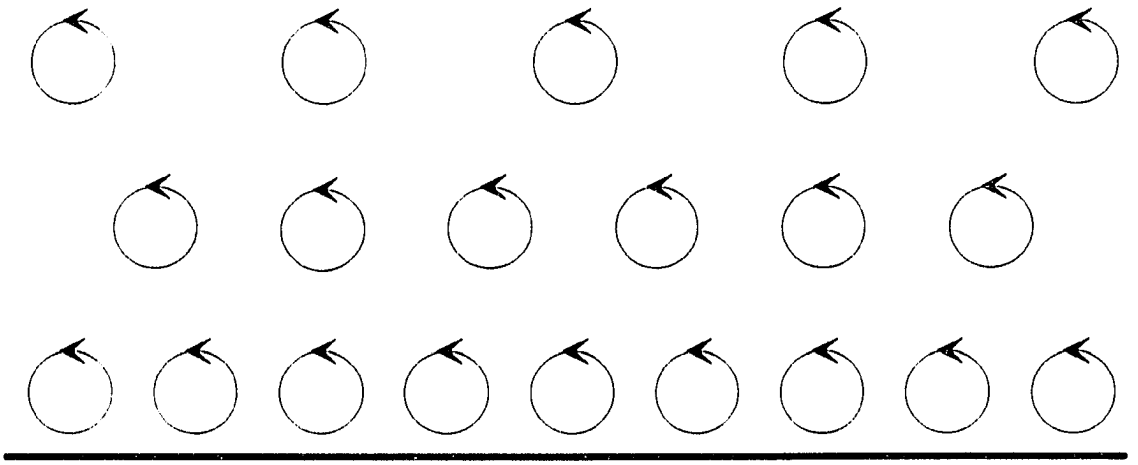

Fig. 1.5 Illustration of the flux-line distribution near the surface when pinning prevents the flux lines freely moving into the material

Bean's model [Bean, 1962]. In the irreversible region of applied field just above H_{c1}, the effect of pinning tends to hold back the flux near the surface, causing the gradient of the flux density as shown in Fig. 1.5. From the Ampere's law $\nabla \times \mathbf{H} = 4\pi\mathbf{J}/c$, the field gradient causes the current flowing perpendicular to the direction of field. As can be seen in Fig. 1.5, this current arises because when there is a variation in the flux line density the currents from neighboring rows do not cancel. The Bean model assumes that the effect of pinning is to determine a maximum gradient of flux density, hence the maximum current J_c.

It should be noted that the flux distribution at any point on an irreversible magnetization curve is in a metastable state. The flux is held back by pinning centers present from reaching the equilibrium distribution, which correspond to a point on the reversible curve. However, due to the thermal energy of the flux

lattice, they are in a state of vibration, and as the time passes it is expected to shake itself from one pinned configuration to another one, which is somewhat closer to the equilibrium state. The change of flux distribution in time was first confirmed experimentally by Kim et al. [Kim et al., 1962], who showed that the vortex trapped in a hollow cylinder of an irreversible type II decayed. They also showed the trapped flux was a linear function of $\ln t$. This phenomenon is called flux creep and the theory of flux creep in irreversible type II superconductors was first given by Anderson [Anderson, 1962].

1.2 High-T_c Superconductors

Following the discovery of first high-T_c superconductor $La_{2-x}Ba_{2-x}Cu0_{4-y}$, subsequent efforts to raise T_c were carried out successfully, and Wu et al. were the first to find a material that can be superconducting above the liquid nitrogen [Wu et al., 1987], which turned to be $YBa_2Cu_3O_{7-\delta}$, with T_c of around 93 K. This discovery has significant meaning, since it promised to open the way for many new applications which were not economically attractive, and as a result, caused more efforts were made in search for the new high-T_c superconductors.

Soon after the discovery of these superconductors, two families of compounds were discovered with even higher value of T_c. The first among these discoveries was by Maeda et al. [Maeda et al., 1988] for the Bi-Sr-Ca-Cu-O compound with a T_c up to 120 K. This was soon followed by the discovery of a group of superconductors with similar structures, known as Tl-Ba-Ca-Cu-O compounds [Sheng and Herman, 1988], with a T_c up to around 125 K. Though each of these high-T_c superconductors has its own characteristics, they share a

common factor: the superconducting state seems to be based on holes in the CuO_2 planes. Still, the presence of anisotropy, the granular structure, and the higher operating temperature result in quite different characteristic parameters relative to conventional superconductors.

While the La, Bi, and Tl compounds contain planes of Cu and O atoms, the Y compounds [Greedan et al., 1987; Beno et al., 1987] have both CuO_2 planes and CuO chains. Fig. 1.6 shows structures of $YBa_2Cu_3O_{7-\delta}$ and $Bi_2Sr_2CaCu_2O_y$ for a comparison. A great deal of work has focused on the roles of these plains and chains in the YBCO materials. It is now believed that the CuO_2 planes contain the carriers responsible for the supercurrents. The chains act as electron reservoirs that control the density of carriers either by changing the oxygen stoichiometry or by other types of doping. There is a tendency for the oxygen atom vacancies to line up along the a or b axis to perform CuO chains in the adjacent rows, and the $YBa_2Cu_3O_{7-\delta}$ compounds with $0 < \delta < 1$ tend to have ordered arrays of completely oxygen deleted chains [Kubo et al., 1988; Hodeau et al., 1988; Fleming et al., 1988].

A series of Bi or Tl compounds that are related but having different stacking sequences can be obtained with varying stoichiometry, which leads to varying numbers of Cu-O planes in the crystal's unit cell. For each new Cu-O plane, an adjacent Ca-O planes is also introduced. The general chemical formula for the Bi and Tl compounds is $B_yA_2Ca_{n-1}Cu_nO_x$, where B is Bi or Tl, A is Sr for the Bi compound and Ba for the Tl compound, n is the number of Cu-O layers per unit cell: n=1, 2, 3, 4 ... [Haldar et al., 1988]. The subscript y is 1 or 2 for the Tl compounds, denoting single or double adjacent of Tl-O, and it is 1 for Bi compounds. By increasing n, T_c is raised to 120 K for Bi a compound and to 125

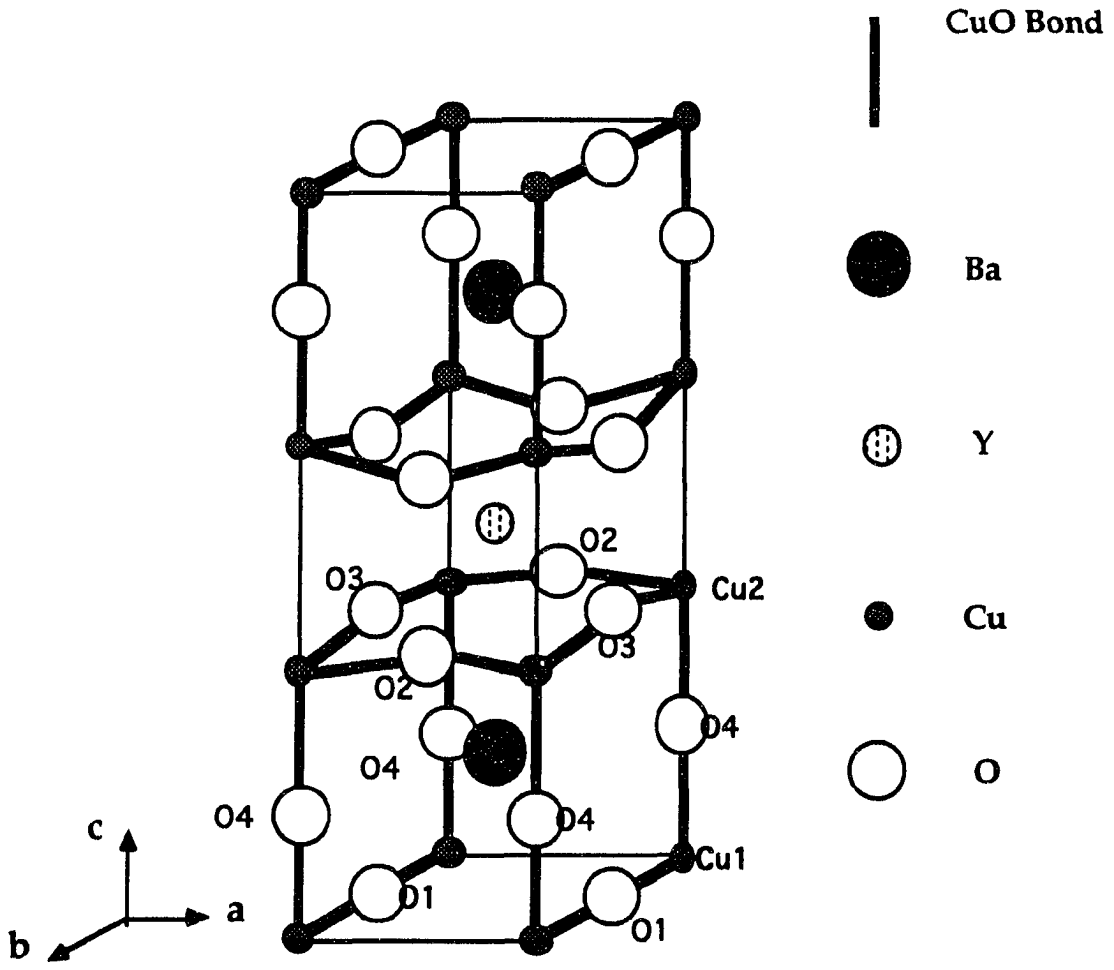

T_c = 93 K	$\xi_{ab}(0)$ = 15-17 Å
a = 3.8591 Å	$\xi_c(0)$ = 3-5 Å
b = 3.9195 Å	$\lambda_{ab}(0)$ = 1400 Å
c = 11.8431 Å	$\lambda_c(0)$ > 7000 Å

Fig. 1.6 Crystal structure and characteristic values; (a) $YBa_2Cu_3O_{7-\delta}$

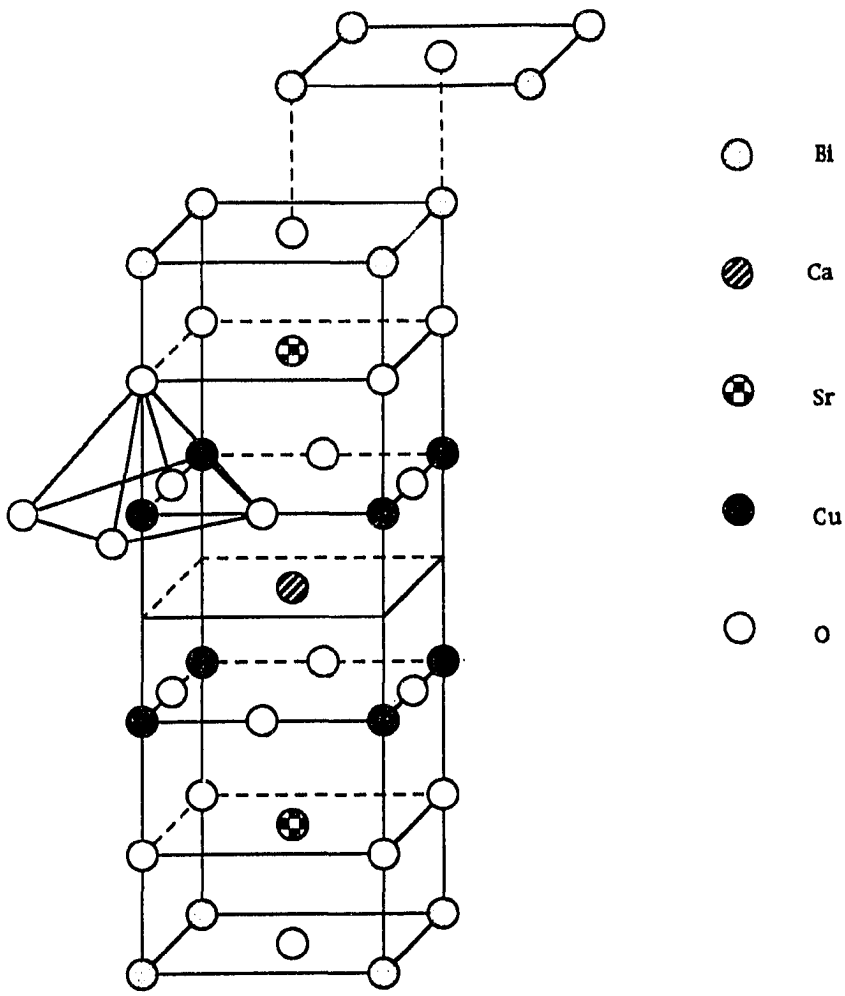

T_c = 85 K

a = 3.814 Å

c = 30.52 Å

$\xi_{ab}(0)$ = 27 Å

$\xi_c(0)$ = 0.5 Å

$\lambda_{ab}(0)$ = 2500 Å

$\lambda_c(0)$ > 10,000 Å

Fig. 1.6 (continued) (b) $Bi_2Sr_2CaCu_2O_y$

K for Tl a compound.

Some of the most fundamental properties of these high-T_c superconductors are the following: high T_c, short coherence length, and large spatial anisotropy. When the high T_c is high, it means many types of excitations, like phonons, are present in the upper operating temperature range of the superconductivity. The presence of these excitations is expected to affect some of the properties of these new compounds, such as T_c, the critical current density J_c, etc.

The short coherence length, ξ, of high-T_c superconductors leads to several unusual properties. In these materials, the reported values of $\xi(T)$ at $T << T_c$ typically ranges between 0.5 and 30 Å, depending on the crystallographic direction of the electron momentum, the substance, the type of experiment, and the model for analyzing the data. In the conventional superconductors, ξ is typically on the order of 1000 Å, unless it is decreased by alloying or defects. Because ξ is much shorter than the electromagnetic penetration depth in high-T_c superconductors, they are all extreme type II superconductors ($\kappa >> 1$). Therefore, they form magnetic vortices when exposed to a high magnetic field, and they have extremely high upper critical field H_{c2} values. This short coherence length also implies that the superconducting properties will be very sensitive to small scale structural and chemical imperfections than in conventional superconductors, since the coherence length is about the same order of the size of a crystal unit cell (See Fig. 1.6).

The large anisotropy exhibited by the new superconductors raises fundamental questions. The theory of superconductivity in the conventional superconductors are almost all nearly isotropic and for the case of highly anisotropic superconductors, the theory is still in an early stage of development.

Fig. 1.7 illustrates the magnetic phase diagram for the high-T_c

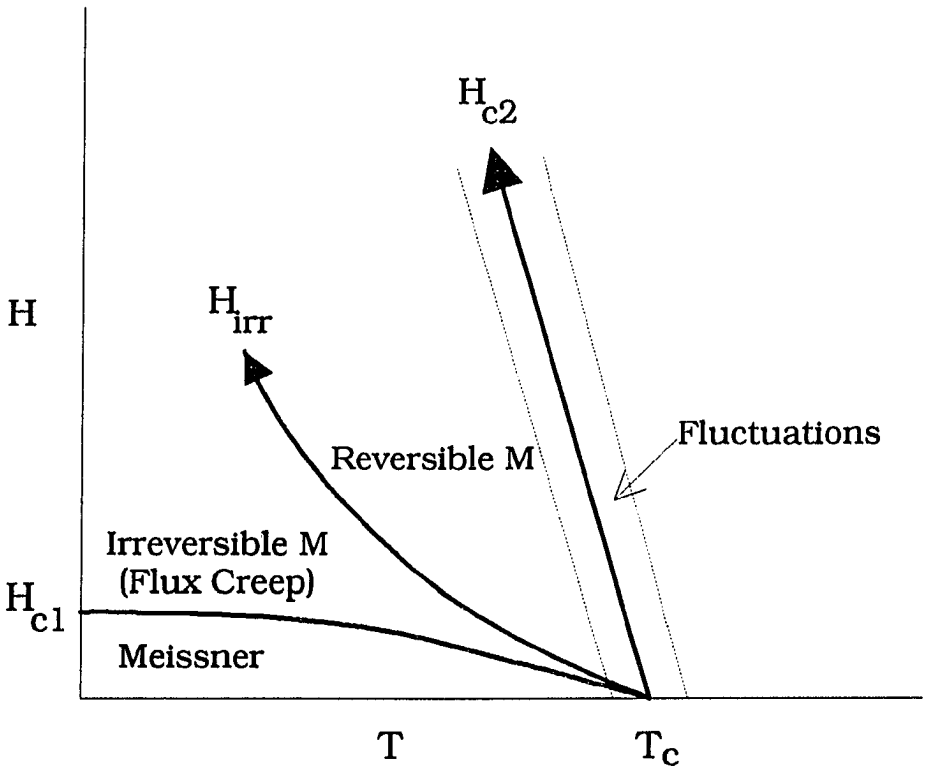

Fig. 1.7 Magnetic phase diagram for high-T_c superconductors

superconductors. Each area in the diagram displays unique properties, such as flux creep, reversible magnetization, fluctuations. For the high-T_c superconductors, there is a reasonably well defined range of H and T where the magnetization data are thermodynamically reversible and fit existing theory rather well. The vortex structure of a type-II superconductor has been exclusively studied for the cases of low and high magnetic field since the pioneering work by Abrikosov [Abrikosov, 1957] based on the Ginzburg-Landau equations. However, due to the large values of H_{c2} in the high-T_c superconductors, high field result of Abrikosov is valid only for temperatures in the vicinity of T_c and is usually dominated by the fluctuation effects [Lee et al., 1989]. On the other hand, there also exists a broad region of intermediate field $H_{c1} << H << H_{c2}$ in which the magnetization studies have been done extensively. Unfortunately, in this field region, the Ginzburg-Landau equations cannot be solved in closed form. Recently, Hao and Clem [Hao et al., 1991; Hao and Clem, 1991] proposed a model based on a variational method to attack this problem and extended this model to include an energy term from suppression of the order parameter in the vortex core as well as an anisotropy term, which resulted in a very accurate description of reversible magnetization when H is parallel to one of the principal axis.

A direct application of the Hao-Clem model can be found in determining the critical fields and the Ginzburg-Landau parameter, κ, at a given temperature. There has been an ambiguity in determining these quantities from experimental data. Even for the upper critical field of $YBa_2Cu_3O_{7-\delta}$, where there is a certain degree of general agreement, confusion still exists among published results. A few of the excellent studies in this category include the works done by Welp et al. [Welp et al., 1989] and Hao et al. [Hao et al., 1991]. They agree fairly well between

different samples and Welp et al.[Welp et al., 1991] also reported that they got a similar result of $-dH_{c2}/dT$ = 1.9 T/K from their analysis based on simplified form of Hao et al.'s equation [Hao et al., 1991] that displays logarithmic field dependence.

A direct determination of the thermodynamic critical field, H_c, from the relation [Saint et al., 1969]

$$\int_0^{H_{c2}} MdH = -\frac{H_c^2}{8\pi} \tag{1.3}$$

is difficult, because fluctuations make it difficult to know where the upper limit of the integral should be. For the high-T_c superconductors, the upper limit has to be further extended beyond H_{c2} to take into account the flux exclusion related with fluctuations at H_{c2} and even considerably higher field. It is difficult to access this high field region for magnetization measurements. Therefore, this method is useful only near T_c, where H_{c2} is a relatively small value. An alternate way to determine H_c is a more indirect method of determining H_{c2} and κ, and then calculating H_c from the simple relationship of

$$H_{c2} = \sqrt{2}\kappa H_c. \tag{1.4}$$

This, however, adds another problem of determining κ in addition to already difficult task of determining H_{c2}. A successful application of the Hao-Clem model allows κ and H_c to be found as fitting parameters to an equation which is a variational solution for an extreme type II superconductor, where the Ginzburg-Landau parameter satisfies the condition $\kappa >> 1$, in the intermediate field region.

CHAPTER 2. THEORETICAL REVIEW

2.1. Free Energy and Specific Heat Jump

In classical superconductors, such as Sn and In [Mapother, 1962], it is well established that the onset of superconductivity is a second-order phase transition and that reversible thermodynamics can be used to relate magnetization data to specific-heat data. First, the change in free energy (Gibbs free energy) G is related to the magnetic field H by

$$dG = -SdT + VdP - MdH, \tag{2.1}$$

where S is the entropy, V is the volume, P is the pressure, and M is the magnetization [Pippard, 1960]. Therefore, at constant temperature T and constant pressure P, the difference in free energy can be written as

$$G_H(T) - G_0(T) = -\int_0^H M dH', \tag{2.2}$$

where M is the equilibrium magnetization and H' is a dummy variable of integration. A full free energy surface over a field-temperature (H-T) plane can be mapped out according to the above equation. Once the free energy is determined, the change in specific heat with increasing magnetic field is given from the curvature of the free energy surface G_H-G_0 with respect to temperature along lines of constant H. In thermodynamics of a reversible system, the specific heat is defined as

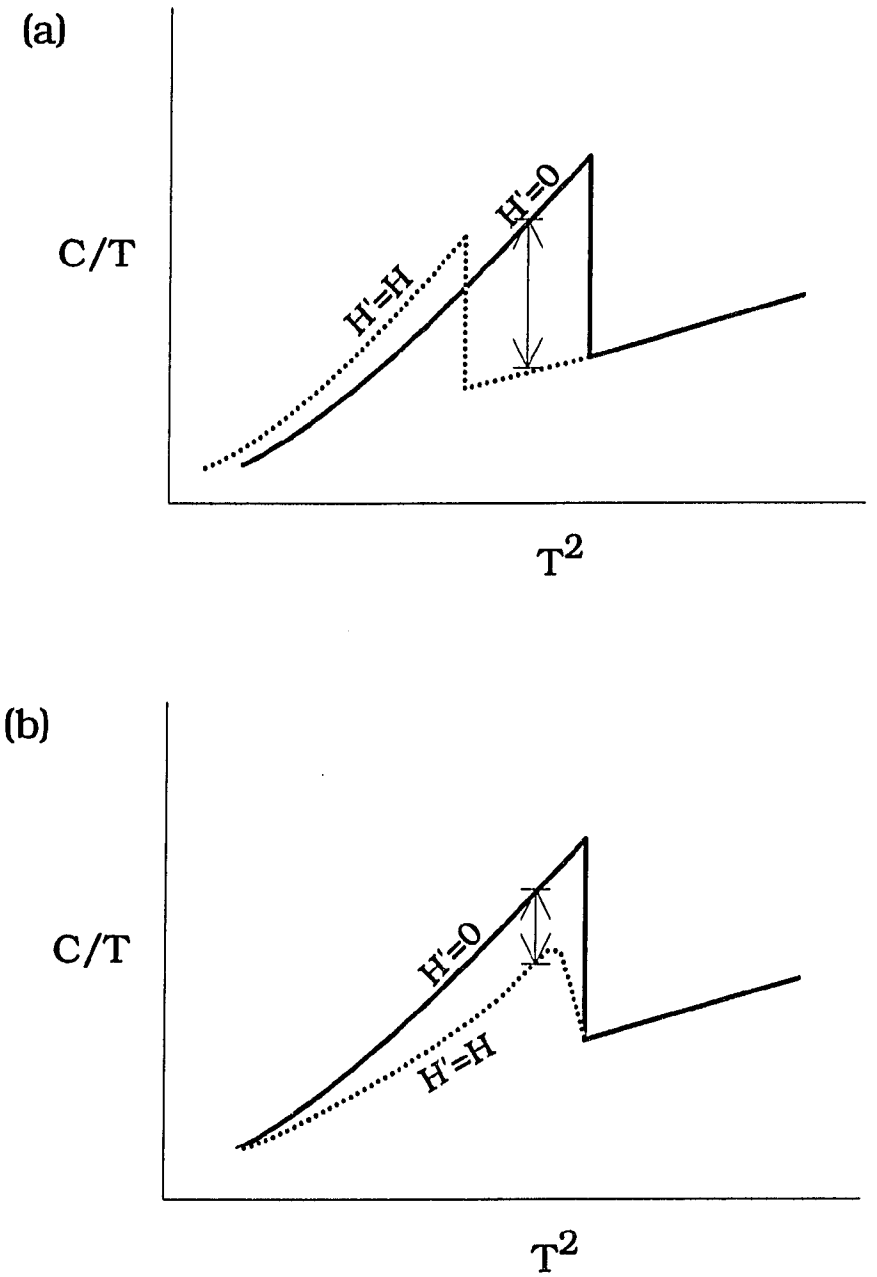

Fig. 2.1 The specific heat jump (shown as arrows) for (a) conventional and (b) high-T_c superconductors

$$C_p = \left(\frac{dQ}{dT}\right)_p = T\left(\frac{\partial S}{\partial T}\right)_p . \tag{2.3}$$

Therefore, from equations (2.1) and (2.3), the change in specific heat between the fields H' = 0 and H'= H is given as

$$C_0 - C_H = T\left[\frac{d^2(G_H(T) - G_0(T))}{dT^2}\right]. \tag{2.4}$$

The usual minus sign does not appear in this equation, because C_0 and C_H are interchanged in accord with the way specific-heat jump data are usually plotted. It is to be noted, however, that this equation provides only the difference in specific heat (specific heat jump) but not the absolute specific values. As shown in Fig. 2.1, while the onset temperature of the specific heat jump for a conventional superconductor gets suppressed with the increasing field, for the high-T_c superconductors it appears to be independent of the field and the increasing field seems to reduce only the magnitude of the specific heat jump.

2.2. Critical State Models and Flux Creep

Bean Critical State Model

The non-ideal type-II superconductors exhibit magnetic hysteresis as a result of flux pinning caused by various defects, as discussed in the earlier chapter. To explain this magnetic behavior, Bean [Bean, 1962] proposed the critical state model in which the fluxoids are distributed throughout the sample in

such a way that the Lorentz force is balanced by the pinning force and the fluxoids are in equilibrium positions.

When the initial applied field is below H_{c1}, the flux penetrates the sample only within the thickness of the London penetration depth λ. As the field increases above H_{c1}, the magnetic field starts to penetrate the material in form of fluxoids. The fluxoids nucleate in the London penetration layer, and then move toward inside of the material until they are pinned by defects. As more and more fluxoids file up, some fluxoids overcome this defect and move further inside the material, until finally the fluxoid distribution reaches the equilibrium condition. This final state is called the critical state. At this stage, the current density is identical to the critical current density, J_c, and it satisfies the condition

$$\nabla \times \mathbf{B}(\mathbf{r}) = \frac{4\pi}{c}\mathbf{J}_c(\mathbf{r}). \tag{2.5}$$

The magnetic hysteresis in non-ideal superconductors is related by the history of the applied field. The critical state model simplifies the problem so that only the phenomenological quantities need to be considered with Maxwell's equations and appropriate boundary conditions. The magnetic hysteresis is related with a microscopic parameter, the critical current density J_c. Since the hysteresis systematically varies with the field and temperature, J_c is generally a function of both field and temperature in the critical state model. The Bean model, however, is the simplest case in that it assumes J_c is field independent. More sophisticated critical state models incorporate the field dependency of J_c into the model [Kim et al., 1962; Fietz et al., 1964; Irie and Yumafuji, 1967]. Recently, M. Xu et al. [M. Xu et al., 1990] proposed a generalized critical state model which

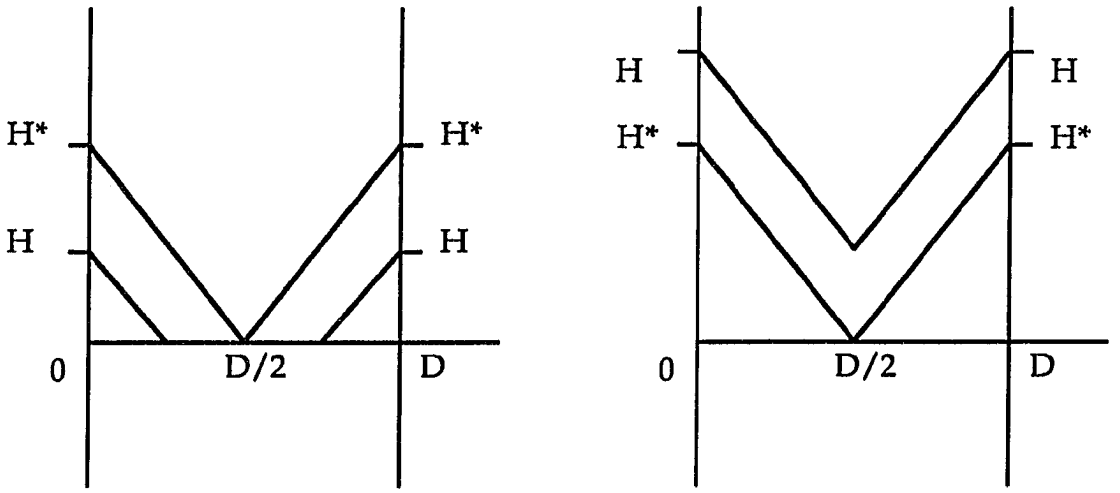

Fig. 2.2 The local field profile for an infinitely long slab with a with D based on Bean's critical state model: (a) partial penetration; (b) full penetration. The schematic is only for the increasing field

reduces to the models listed above in the appropriate limits.

As discussed above, the Bean model assumes that the critical current density is only a function of temperature:

$$J_c[B(x),T] = J_c(T), \tag{2.6}$$

where B(x) is the local magnetic induction. In high fields and in a critical state, the one dimensional form of Ampere's law $\partial H/\partial x = 4\pi J_c/c$ becomes

$$\frac{\partial B}{\partial x} = \frac{\partial B}{\partial H}\frac{\partial H}{\partial x} \approx \frac{4\pi}{c} J_c, \tag{2.7}$$

since $\partial B/\partial H \approx 1$ at high fields. Fig. 2.2 displays the field distribution for an infinitely long slab with thickness D, when the field parallel to the plane of the slab and H_{c1} is assumed to be negligibly small. Under these assumptions one can obtain a linear dependence of the local field B(x) with a position x as shown in the figure.

The average magnetic induction is defined as an average of the local field B(x) over the sample,

$$\langle B \rangle = \frac{2}{D}\int_0^{D/2} B(x)dx. \tag{2.8}$$

By the definition of magnetic induction $\langle B \rangle = H + 4\pi M$, the magnetization is related with the applied field. And the magnetic hysteresis is the difference between the magnetizations for the increasing (M_+) and Decreasing (M_-) fields. As shown in Fig. 2.3, the hysteresis in the field region $H^* \le H \le H_m - 2H^*$ (where H^* is the full-penetration field defined as $H^* = 2\pi J_c D/c$ and H_m is the maximum applied field) is given as

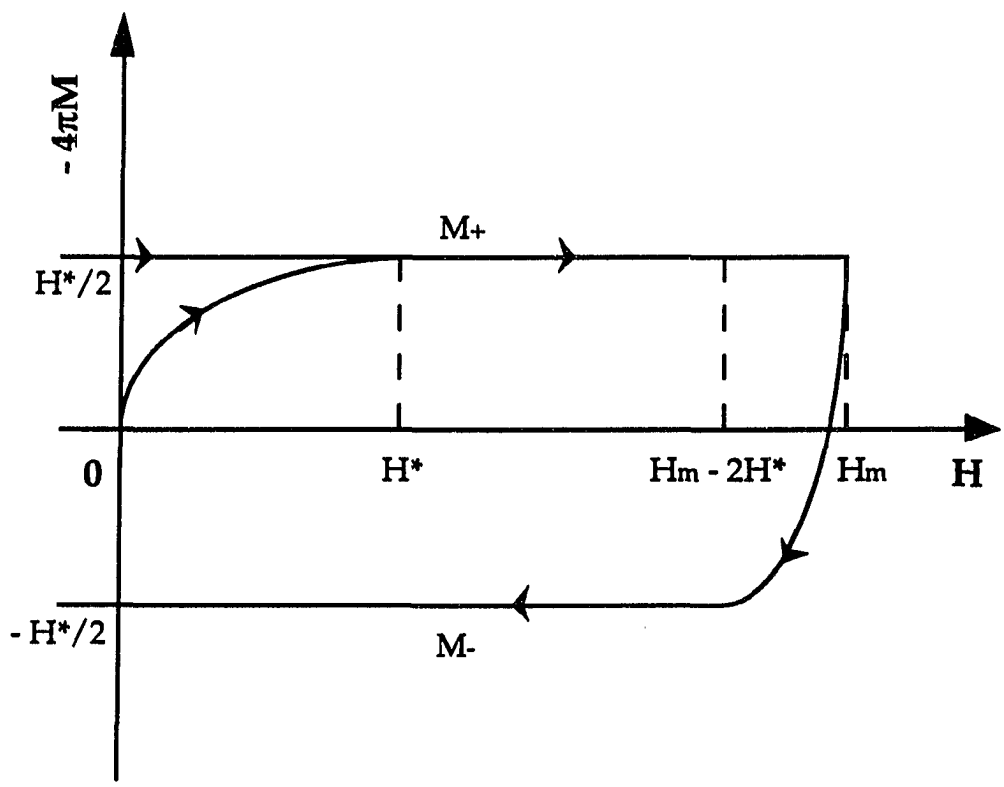

Fig 2.3 The hysteresis loop according to the Bean's model with the field independent J_c

$$\Delta(4\pi M) = 4\pi(M_- - M_+) = H^* = \frac{2\pi D}{c} J_c \qquad (2.9)$$

In practical units (gauss, A/cm^2, and cm), above equation is written as

$$\Delta(4\pi M) = \frac{\pi D}{5} J_c. \qquad (2.10)$$

Likewise, in the case of a long cylinder, the relation between the hysteresis and J_c can be calculated as

$$\Delta(4\pi M) = \frac{8\pi R}{3c} J_c, \qquad (2.11)$$

or in practical units,

$$\Delta(4\pi M) = \frac{4\pi R}{15} J_c. \qquad (2.12)$$

Above equations imply that the critical current density can be inductively estimated from the hysteresis data, and the higher J_c values are resulted from the higher hysteresis as a result of the defects of the sample that work as pinning sites.

Anderson-Kim Model

Extending the Bean's critical state model, in which a field independent J_c is assumed, Anderson and Kim [Anderson, 1962; Anderson and Kim, 1964] introduced a model with a field dependent J_c that has the form of

$$J_c(T,B(x)) = \frac{J_c(T)}{1+|B(x)|/H_0(T)}\ , \qquad (2.13)$$

where H_0 is a material parameter with the dimension of magnetic field which can be determined experimentally. Anderson showed that J_c is limited at finite temperature by thermal activation of bundles of fluxoids over flux pinning cites such as defects and impurities [Anderson, 1962]. This model predicts a logarithmic time decay in J_c with time, which was observed in measurements by Kim et al [Kim et al., 1962]. In other words, J_c will eventually decay to zero but it would take extremely long time for this to happen.

For conventional superconductors the size of this bundle is on the order of 100 ~ 1000 Å, which is about the size of penetration depth λ (which is larger for high-T_c superconductors) and one fluxoid bundle typically contains order of 100 fluxoids. When a bundle of fluxoids encounter a defect in the material, there will be a difference in the free energy between the superconducting bulk material and the normal defect. For simplicity, if the normal defect volume is assumed to be d^3 and assuming that the entire bundle is pinned, the difference in free energy is

$$\Delta F_{max} = F_n - F_s = \frac{H_c^2}{8\pi} d^3. \qquad (2.14)$$

In most cases it is not likely that the entire bundle of fluxoids is pinned. Therefore, Anderson introduced a parameter p which is effective fraction of pinning. If the bundle is pinned over the distance r, then $p \sim d^2/\lambda^2$. In this case, the difference in the free energy becomes

$$\Delta F = p\Delta F_{\max} = p\frac{H_c^2}{8\pi}d^3. \tag{2.15}$$

In the critical state, the Lorentz force per unit volume is $\mathbf{J}_c \times \mathbf{B}/c$. If this is integrated over the volume of the bundle d^3, the contribution to the free energy by the Lorentz force is the product of Lorentz force and the hopping distance

$$F_L = -J_c B d^4/c = -J_c \Phi d^2/c, \tag{2.16}$$

where the area is assumed to be d^2, so the flux $\Phi = n\Phi_o$ (where n is an integer, and Φ_o is the flux quantum). Therefore, the actual free energy in this case is given as

$$\Delta F = p\frac{H_c^2}{8\pi}d^3 - J_c \Phi d^2/c. \tag{2.17}$$

The free energy difference can be identified as the pinning potential of the superconductor. Under no driving force (no current, no fields), the pinning potential $U = pH_c^2 d^3/8\pi \equiv U_o$. When external field or current is applied to the superconductor, the pinning potential is modified by the Lorentz contribution U_L, given as $U_L = J_c \Phi d^2/c$. Fig. 2.4 shows the pinning potential at various strengths of applied currents for the periodic pinning centers.

For the thermal activation of the fluxoid bundle, Anderson proposed the hopping rate is given by

$$\begin{aligned} \text{hop. rate} &= R_o \exp(-\Delta F/kT) \\ &= R_o \exp\left[-(F_o - q\alpha)/kT\right], \end{aligned} \tag{2.18}$$

where $q\alpha$ is the Lorentz force term with $\alpha = JB$ and q is a constant. In this theory

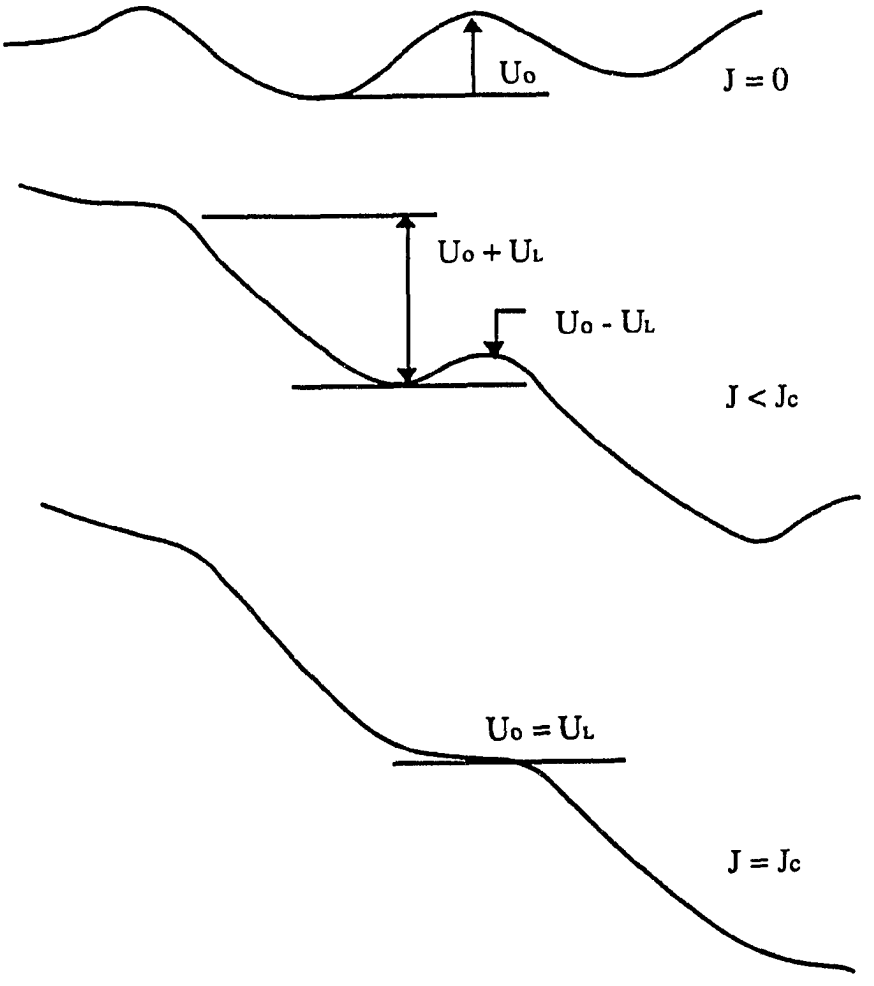

Fig. 2.4 Illustration of the pinning potential at various Lorentz driving force. The top curve shows the unperturbed U_o, and the bottom curve shows depinning as the Lorentz term rises to match U_o

there is no precise "critical state," since the creep in Eq. (2.18) continues at any value of $\alpha = JB$. The critical state observed in the Kim et al.'s Nb-Zr tube experiments [Kim et al., 1962] represents only a quasi-equilibrium state at which the creep rate falls below an observable limit.

As in any activation process, the rate is expected to be logarithmic in time and this follows simply from the fact that the Eq. (2.18) can be rewritten in the form

$$\frac{\partial \alpha}{\partial t} \propto \exp\left(\frac{q\alpha}{kT}\right) \tag{2.19}$$

which has a solution

$$\alpha = \text{const.} - (kT/q)\ln t. \tag{2.20}$$

Beasley-Labusch-Webb Model

Beasley et al. [Beasley, Labusch and Webb, 1969] proposed a model which is essentially based on the model of Anderson and Kim with a more accurate Lorentz force expression of the form

$$F = \frac{1}{c}\mathbf{J} \times \mathbf{B}\frac{\partial H(B)}{\partial B}. \tag{2.21}$$

This model, called as Beasley-Labusch-Webb model or simply as Beasley model, starts with an expression for the flux density **D**, which is the amount of flux per unit length and time that crosses a line perpendicular to **B** and $\nabla\mathbf{B}$

$$\mathbf{D} = -\frac{\nabla \mathbf{B}}{|\nabla \mathbf{B}|} B\omega v_o e^{-U(B,\nabla B)/kT}, \tag{2.22}$$

where ω is the average distance moved in a flux jump and the thermal activation term shows the dependence of U on fields and gradients (hence, currents).

With the condition for the conservation of the flux

$$\frac{\partial B}{\partial t} = -\nabla \bullet \mathbf{D}, \tag{2.23}$$

and assuming that $U = U_o - |F|VX << kT$ (where V is the activation volume and X is the pinning length), Beasley et al. derived the expression for the flux creep rate $R \equiv d\Phi/d\ln t$ that gives the average of

$$R_{av} = \frac{\pi}{3} kT\rho^3 \frac{4\pi}{10} \frac{J_c}{U_o}. \tag{2.24}$$

This equation can be related to the average magnetization M, which is the observable quantity in our study, using the relations $\Phi = B(\pi\rho^2)$ and $B = H + 4\pi M$, and defining the flux creep rate $S \equiv dM/d\ln t$ gives

$$U_o = kT \frac{\rho J_c}{30S}. \tag{2.25}$$

This allows the material sensitive parameter U_o to be expressed in terms of the experimentally measurable quantities S and J_c. Here, it is to be noted that U_o in Beasley model does not represent the true barrier height U_p. As shown in Fig. 2.5, U_o represents the J = 0 intercept of the tangential line to the true non-linear pinning potential on the U vs. J plane. Therefore, it approaches to U_p only under

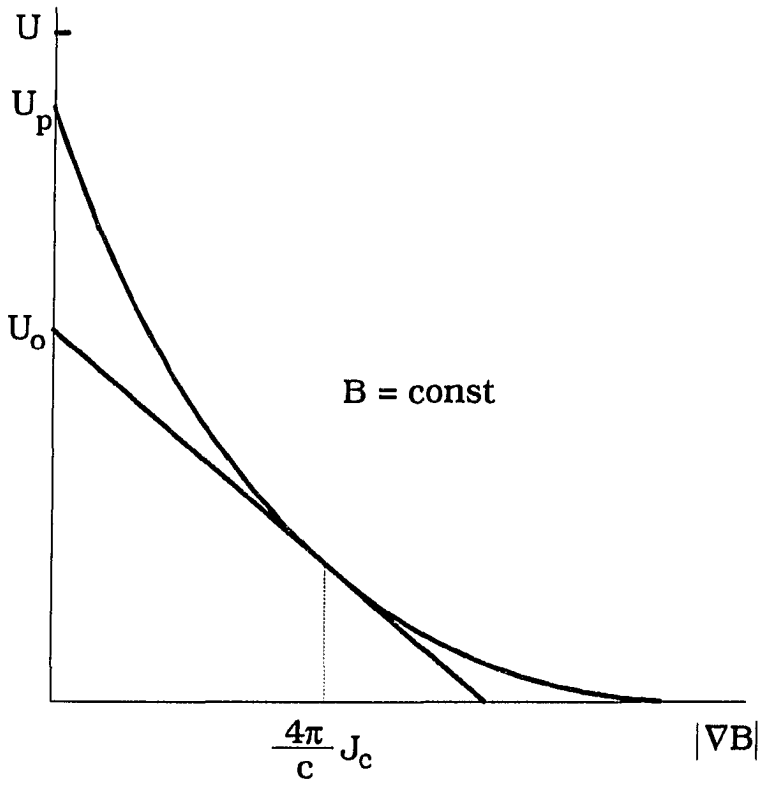

Fig. 2.6 Illustration showing the effective pinning potential U_o in the Beasley model and the actual barrier height U_p. The curve represents the actual dependence of U on J_c and the line represents Beasley's linear approximation

the low driving force, and the discrepancy increases as the driving force gets larger ($U >> U_o$).

2.3 Critical Fields Calculations from Various Models.

High Field Limit ($H \approx H_{c2}$)

In the high field region near the upper critical field H_{c2}, the superconducting order parameter is small and the Ginzburg-Landau (GL) equations can be linearized. Abrikosov showed in this high field limit the magnetization is given as [Abrikosov, 1957]

$$-4\pi M = \frac{H_{c2}(T) - H}{\left(2\kappa^2 - 1\right)\beta_A} \tag{2.26}$$

where β_A is a vortex lattice dependent parameter (for a hexagonal lattice β_A = 1.16). In GL theory, the temperature dependence of H_{c2} is

$$H_{c2} = \frac{\Phi_o}{2\pi\xi^2(T)} = \frac{\Phi_o}{2\pi\xi^2(0)}(T - T_c), \tag{2.27}$$

and, therefore, M(T,H) is linear in both T and H. This suggests that a linear extrapolation of M(H) or M(T) data will determine $H_{c2}(T)$.

Welp et al. [Welp et al., 1989] first applied this model to $YBa_2Cu_3O_7$ (YBCO) and estimated the linear temperature dependence of H_{c2} with slopes dH_{c2}/dT = -1.9 T/K for the H parallel to c axis and -10 T/K for H perpendicular to c axis. This model provides a simple method to calculate H_{c2} from magnetization

measurements. However, for most high-T_c superconductors including YBCO show a field dependence of the slope dM/dT in contrast to the equation (2.26) that gives the field independent dM/dT. It is also to be noted that this equation is valid only in a temperature region very close to T_c, where the linear magnetization behavior is altered due to the fluctuation effects near T_c.

Intermediate Field ($H_{c1} << H << H_{c2}$)

London model In the intermediate field region of $H_{c1} << H << H_{c2}$ the fluctuation effects are negligibly small and mean field theory is applicable. While the GL equation cannot be solved in closed form due to its non-linearity in this region, the London model has provided good phenomenological description of extreme type-II ($\kappa >> 1$) superconductors. This model, first introduced by Abrikosov [Abrikosov, 1957], has been remaining as the most extensively used tool in the intermediate field region.

According to the London model, the magnetization is predicted as

$$-4\pi M = \frac{H_{c1}}{2\ln\kappa}\ln\left(\frac{\beta H_{c2}}{H}\right) \qquad (2.28)$$

where β is a factor that depends on the cut-off in the vortex lattice sums and is of order unity. Equation (2.28) predicts a logarithmic dependence of M on H which agrees with recent experimental results [Kogan et al., 1988; Mitra et al., 1989; Tuominen et al., 1990]. However, as pointed out by Hao and Clem [Hao and Clem, 1991], Eq. (2.28) excludes the contributions from the vortex cores due to the depression of order parameters to zero at the vortex centers. As a results, the London model description of magnetization is quantitatively incorrect.

Hao-Clem model As an alternative way of solving this problem, Hao and Clem [Hao et al., 1991] proposed solving the GL equation numerically in the intermediate field region with the GL free energy density F, defined as the volume average of the GL free energy functional [Ginzburg and Landau, 1950; Fetter and Hohenberg, 1969] of the form

$$F = F_{core} + F_{em}, \tag{2.29}$$

where F_{core} is the energy related with the vortex cores which are the condensation energy and the kinetic energy associated with gradients in the magnitude of the order parameter, and F_{em} is the electromagnetic energy including the kinetic energy of the supercurrent and the magnetic field energy. Along with the order parameter trial function of the form

$$f = \frac{\rho}{\sqrt{\rho^2 + \xi_v^2}} f_\infty \ , \tag{2.30}$$

above free energy contributions were calculated by Hao et al. [Hao et al., 1991] as

$$F_{core} = \frac{1}{2}\left(1 - f_\infty^2\right)^2 + \frac{B\kappa\xi_v^2 f_\infty^2}{2}\left[\left(1 - f_\infty^2\right)\ln\left(\frac{2}{B\kappa\xi_v^2} + 1\right) + \frac{f_\infty^2}{2 + B\kappa\xi_v^2}\right] + \frac{Bf_\infty^2\left(1 + B\kappa\xi_v^2\right)}{\kappa\left(2 + B\kappa\xi_v^2\right)^2} \tag{2.31}$$

and

$$F_{em} = B^2 + \frac{Bf_\infty K_0\left(\xi_v\sqrt{f_\infty^2 + 2B\kappa}\right)}{\kappa\xi_v K_1\left(f_\infty\xi_v\right)}. \tag{2.32}$$

Here f_∞ and ξ_v are the variational parameters that minimize the total free energy which, for extreme type-II superconductors ($\kappa >> 1$), is given in good approximation as

$$f_\infty^2 = 1 - \left(\frac{B}{\kappa}\right)^4, \tag{2.33}$$

and

$$\xi_v^2 = \frac{2}{\kappa^2}\left[1 - 2\left(1 - \frac{B}{\kappa}\right)^2 \frac{B}{\kappa}\right]\left[1 + \left(\frac{B}{\kappa}\right)^4\right]. \tag{2.34}$$

The thermodynamic magnetic field H is given by

$$H = \frac{1}{2}\frac{dF}{dB} = \frac{1}{2}\left(\frac{\partial F}{\partial B}\right)_{f_\infty, \xi_v}, \tag{2.35}$$

and the result is

$$H = \frac{\kappa f_\infty^2 \xi_v^2}{2}\left[\frac{1 - f_\infty^2}{2}\ln\left(\frac{2}{B\kappa\xi_v^2} + 1\right) - \frac{1 - f_\infty^2}{2 + B\kappa\xi_v^2} + \frac{f_\infty^2}{\left(2 + B\kappa\xi_v^2\right)^2}\right] + \frac{f_\infty^2\left(2 + 3B\kappa\xi_v^2\right)}{2\kappa\left(2 + B\kappa\xi_v^2\right)^3}$$
$$+B + \frac{f_\infty}{2\kappa\xi_v K_1(f_\infty\xi_v)}\left[K_0\left(\xi_v\sqrt{f_\infty^2 + 2B\kappa}\right) - \frac{B\kappa\xi_v K_1\left(\xi_v\sqrt{f_\infty^2 + 2B\kappa}\right)}{\sqrt{f_\infty^2 + 2B\kappa}}\right] \quad . \tag{2.36}$$

The Eq. (2.36) along with the relation $B = H + 4\pi M$ provides us M(H). Therefore, magnetization measurement data can be fit to the Eq. (2.36) to estimate H_c and κ as fitting parameters. Note that H_c is introduced in the fitting, since the Eq. (2.36) is given in dimensionless units where the magnetic field H is scaled in units of $\sqrt{2}H_c = \kappa\Phi_o/2\pi\lambda^2$. This equation does not change its form for the different

orientation of the fields in the anisotropic case, as long as the κ in the equation is treated as an anisotropic parameter. Since the magnetization data was taken with H parallel to c axis in the present study, the fitting gives κ_c.

CHAPTER 3. EXPERIMENT

3.1. Sample Preparation

Most high-T_c superconductors have high anisotropy, but magnetization measurement of a bulk-polycrystalline sample provides information only as the angular average of the various properties of these materials, due to the random orientation of grains. It would be desirable, however, to have the detailed angular dependence of quantities. In the study of a highly anisotropic material such as $YBa_2Cu_3O_{7-\delta}$, the ideal sample would be a large single crystal that is perfectly oxygenated throughout the material and free of all defects. Unfortunately, such a sample has never been made (is extremely difficult to make) because the diffusion rates of oxygen are not very fast. The practical alternatives of making a high quality large single crystal is the grain-alignment of millions of smaller crystals that can be easily oxygenated. There are various ways of achieving grain-alignment, but texturing and grain-aligning in a medium are the two most widely used methods. In this work, most of the measurement was done on grain-aligned $YBa_2Cu_3O_{7-\delta}$. samples. For the flux free energy surface and flux creep studies, melt-textured $YBa_2Cu_3O_{7-\delta}$ was also used for the comparison between the two materials. In this section, procedures for making these samples will be discussed.

Grain-Aligned $YBa_2Cu_3O_{7-\delta}$

Polycrystalline $YBa_2Cu_3O_{7-\delta}$ A 20 g batch of polycrystalline $YBa_2Cu_3O_{7-\delta}$ sample was prepared from appropriate amounts of well dried

mixture of high purity carbonates and oxides of 99.999 % $BaCO_3$, Y_2O_3 and 99.99 % CuO (in wt. %). Drying was done at 400 °C for 10 hours just before weighing to form a stoichiometric mixture of the starting materials. The mixture was hand-ground in the air with an agate mortar and pestle, pressed to pellets and sintered at relatively low temperature of 890 °C (to keep the CO_2 partial pressure low) for 16 hours. After the initial sintering, the sample went through regrinding and sintering process 10 times for extra homogeneity of the sample. Final sintering was done at 975 °C followed by the oxygenation steps at 600 °C and 450 °C for 48 hours each. X-ray powder diffraction data of this sample show clean $YBa_2Cu_3O_{7-\delta}$ peaks with no traces of second phases. The final bulk material has an average grain size of 37.5 μm determined by a linear-intercept method [Exner, 1972] using images from an optical microscope.

Grain-alignment of $YBa_2Cu_3O_{7-\delta}$ For the grain-alignment, these pellets of bulk $YBa_2Cu_3O_{7-\delta}$ are ground to a powder of 20 - 40 μm with the average of around 30 μm, which is only slightly smaller than bulk average size. This is because the grain boundaries are mechanically weaker and grains tend to break off easily at grain boundaries. The grain-alignment was done following the similar procedure reported earlier by Farrell et al. [Farrell et al., 1987].

To start with, the $YBa_2Cu_3O_{7-\delta}$ powder is mixed in a low viscosity and low magnetic susceptibility epoxy called Epotek 301, which had been outgassed previously in vacuum under a heat-lamp. This outgassing process greatly reduces micro air bubbles in the epoxy that have negative effects on the grain-alignment. The mixture of $YBa_2Cu_3O_{7-\delta}$ and Epotek 301 is then placed in a teflon mold and held in an 8 T magnetic field for 10 hours while the epoxy is hardened. Due to the anisotropy in the susceptibility, the tiny single-crystal grains orient themselves

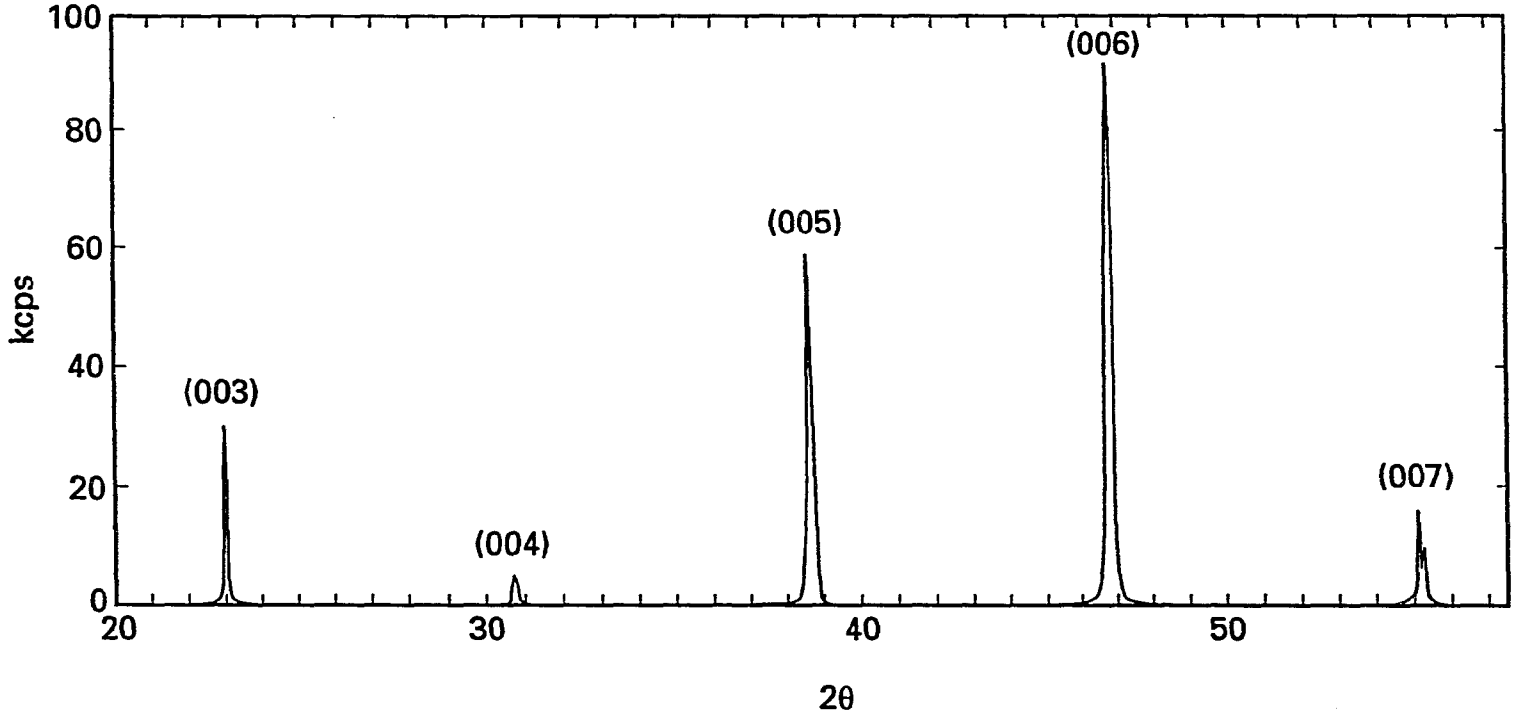

Fig. 3.1 X-ray diffraction pattern of the grain-aligned YBCO showing single crystal like characteristic peaks

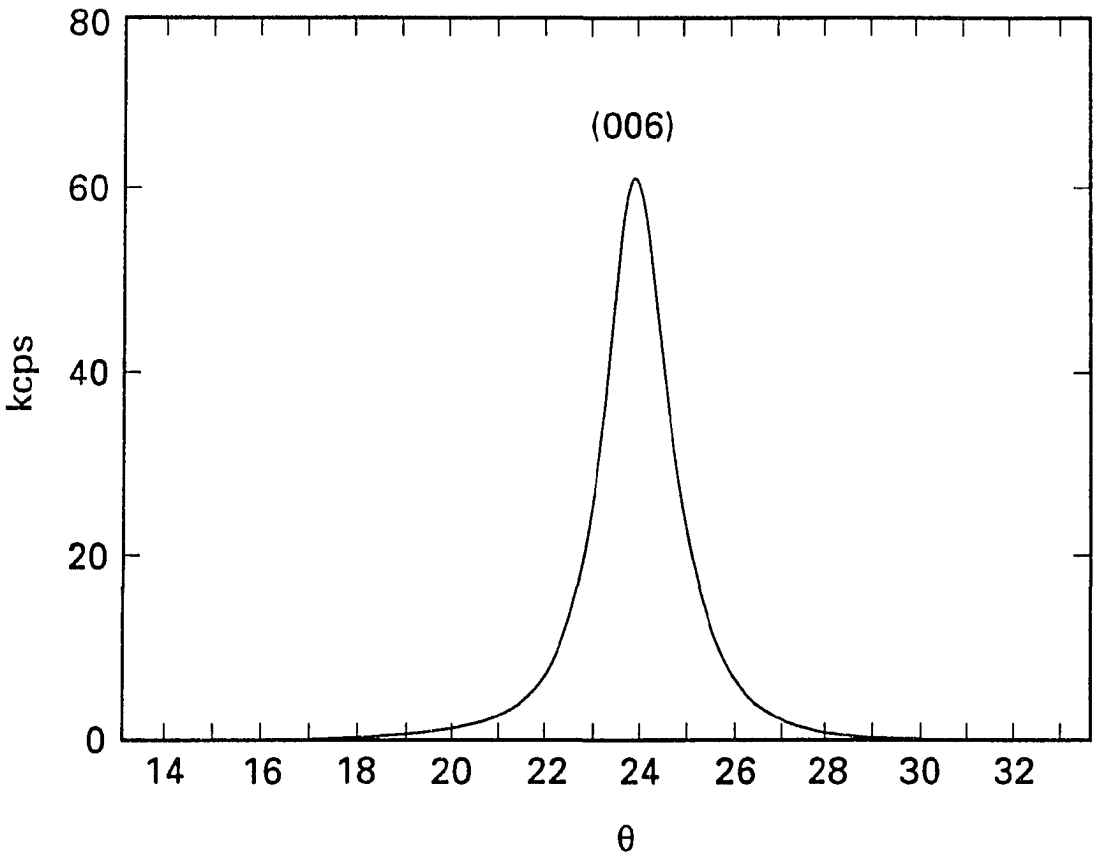

Fig. 3.2 X-ray diffraction data for the (006) peak with the FWHM value of 1.7° shows successful grain alignment

with the c-axes parallel to the magnetic field. Since epoxy separates virtually all of the single-crystal grains, the magnetization measurement data will be taken on an oriented assembly of single crystal grains. The resulting sample has the $YBa_2Cu_3O_{7-\delta}$/epoxy mass ratio of 63.8 % and its net $YBa_2Cu_3O_{7-\delta}$ mass is 40.6 mg. Effectiveness of this grain-alignment can be checked from a x-ray diffraction pattern. For this purpose, a flat-plate sample was made from the mixture at the same time. The x-ray diffraction data show single crystal-like sharp peaks (Fig. 3.1) with a full-width-at-half-maximum (FWHM) of 1.7 ^{o} for the (005) and (006) peaks (Fig. 3.2), indicating the grain-alignment was a success. Magnetization measurements show T_c value of this sample determined from the onset temperature of M vs. T at 5 Oe is 92.5 ± 0.1 K.

Melt-textured $YBa_2Cu_3O_{7-\delta}$

One purpose of these experiments is to compare the free energy surfaces of grain-aligned with the previously published single crystal and also with the melt textured material that are similar in many ways to large single crystals. Solidification from the melt has been found to be an effective way to produce high temperatures superconductors that are highly textured and have relatively high critical current densities. Textured $YBa_2Cu_3O_{7-\delta}$ samples by melt processing (melt-textured $YBa_2Cu_3O_{7-\delta}$) were made by P. J. McGinn for the comparative study of magnetic properties between grain-aligned and melt-textured $YBa_2Cu_3O_{7-\delta}$ samples. The melt-texturing processes was first developed by Jin et al. [Jin et al. 1988, 1989], in which the term "melt-texturing" describing their pioneering directional solidification process. The procedure to make a melt textured sample

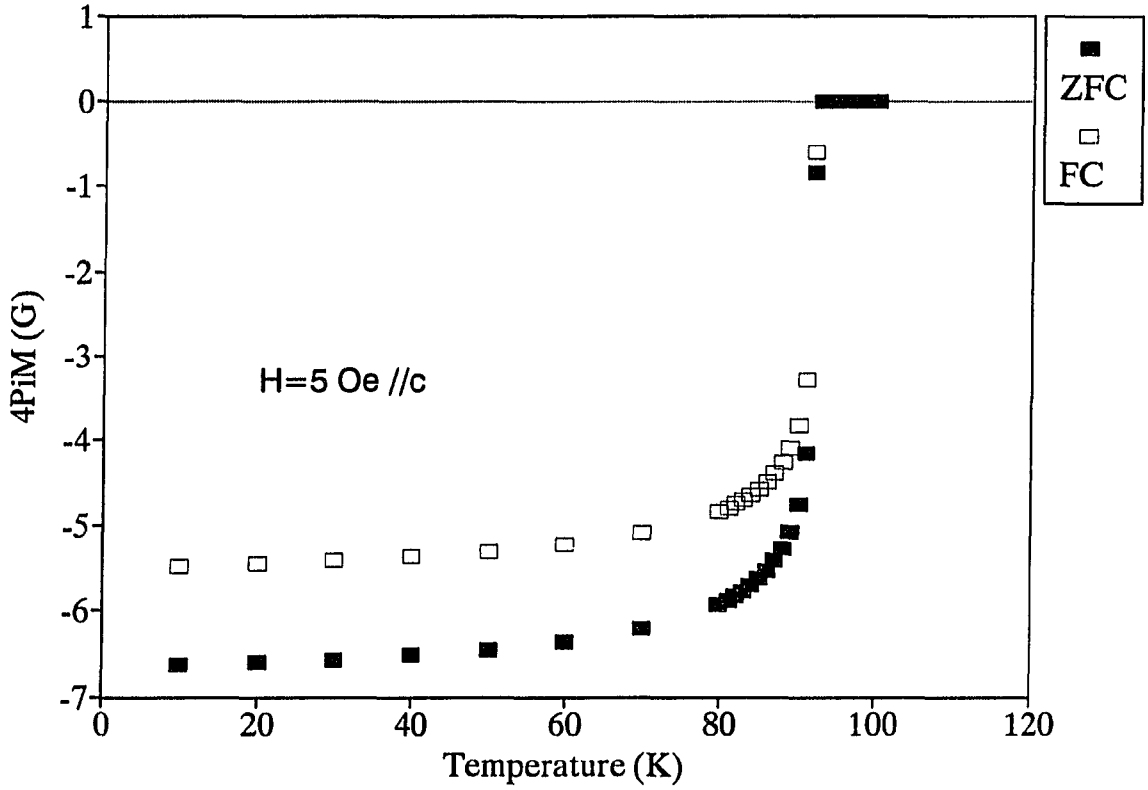

Fig. 3.3 Low-field magnetization vs. temperature plot; (a) grain-aligned YBCO

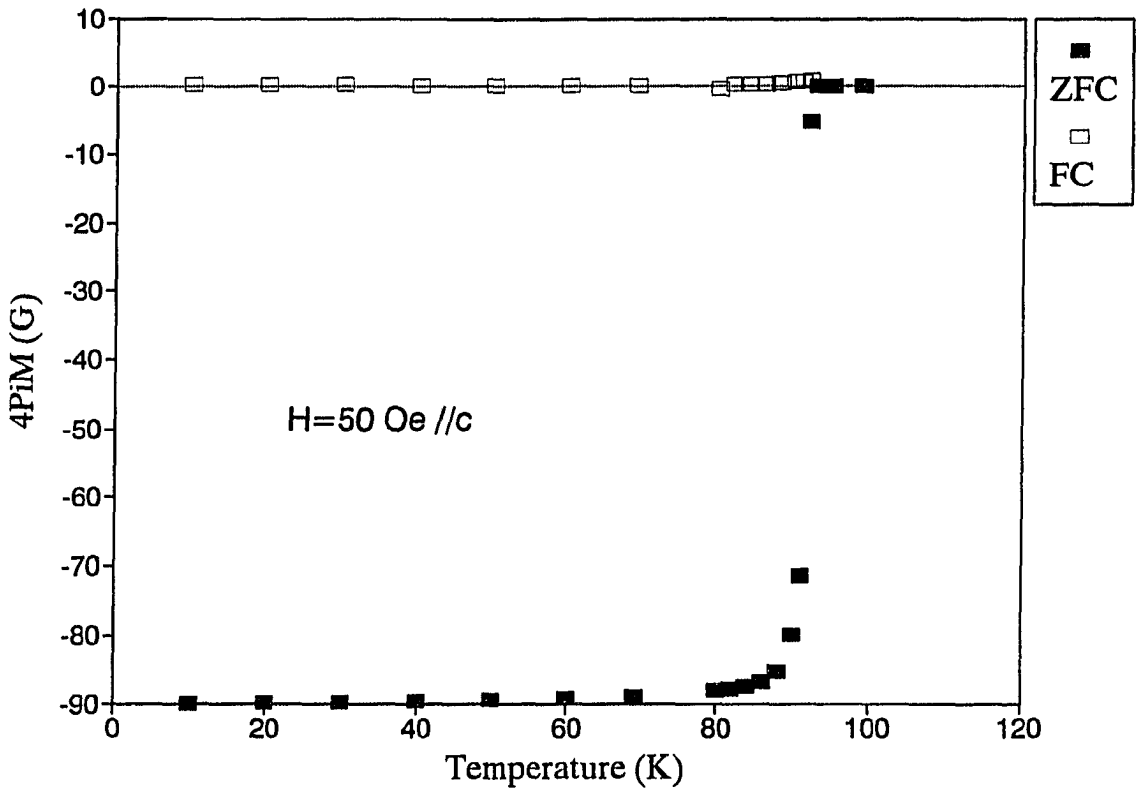

Fig. 3.3 (continued) (b) melt-textured YBCO

involves the heating of bulk $YBa_2Cu_3O_{7-\delta}$ above its peritectic decomposition temperature of 1010 °C where it will decompose to Y_2BaCuO_5 and a liquid phase consisting of $BaCuO_2$ + CuO. By slowly cooling (1 °C/hr.) from 1010 °C to approximately 900 °C, the $YBa_2Cu_3O_{7-\delta}$ will nucleate and grow. More detailed procedures for the melt texturing of $YBa_2Cu_3O_{7-\delta}$ can be found elsewhere [McGinn et al., 1992]. The sample used in this work is in the shape of a canted cylinder, where the a-b planes are off the wire axis by approximately 45 degrees. It is about 2 mm long and has the diameter of 0.6 mm. Its T_c, estimated from M vs. T measurements at 5 Oe field, is 92.0 ± 0.1 K. Although this sample was sent to us pre-oxygen-annealed, additional annealing was done in the flowing oxygen for 20 days at 450 °C to ensure full oxygenation. Magnetization drops off sharply as the sample is rotated off from the H // c orientation for this sample; therefore, mounting the sample with good alignment is important for the comparison with the grain-aligned sample. Fig. 3.3a and Fig 3.3b compare the low field magnetization vs. temperature data for the grain-aligned and the melt textured $YBa_2Cu_3O_{7-\delta}$ samples. Notice the FC magnetization values of the melt-textured YBCO data is suppressed to near zero showing a sign of strong pinning.

3.2. Grain Size Control in $YBa_2Cu_3O_{7-\delta}$

One of the goals of this work was to study the changes in superconducting properties as the twin plane spacing is systematically altered. To prepare samples having the twin spacing, d, range from 50 to 200 nm, we utilized the fact that twin spacing is related to grain size, D, as $d \propto \sqrt{D}$ [Arlt et al., 1985; Shaw et al., 1989]. Grain-aligned $YBa_2Cu_3O_{7-\delta}$ samples with different average grain sizes were made

to study the effect of twin spacing on the free energy and the specific heat jumps. The procedure for making each sample is exactly identical to that of making a grain-aligned $YBa_2Cu_3O_{7-\delta}$ sample as discussed in the earlier section, except for one factor: the final sintering temperature. The average grain size of $YBa_2Cu_3O_{7-\delta}$ increases with the increasing sintering temperature and its temperature dependence have been reported by No et al. and Chumbley et al [No et al., 1989; Chumbley et al., 1989].

Based on these earlier studies, four different final sintering target temperatures were set to produce $YBa_2Cu_3O_{7-\delta}$ samples with different average grain sizes. The same batch of bulk $YBa_2Cu_3O_{7-\delta}$ sample, pre-sintered 10 times in the air at 890 °C, was divided into 4 groups and each group was sintered once more at a different target temperature, under flowing oxygen. Each group was held at the target sintering temperature for 16 hours followed by the slow cooling at 15 °C/hr rate to 600 °C. There it was hold for oxygenation for one to two days under flowing oxygen, and then furnace cooled to the room temperature, which is approximately a cooling rate of 5 °C/min for the tube furnace we have used. After the final sintering, all four samples were put into another oxygenation step at 450 °C for 48 hours to ensure full oxygenation.

Average grain sizes of the final products were evaluated using the linear-intercept method, based on optical microscope pictures taken under the polarized light source. Fig. 3.4 and Fig. 3.5 display photos of these samples. One can easily see that the anisotropy of the grain shape, as well as the size, increases as the final sintering temperature increases. The resulting average grain size values with respect to the final sintering temperatures are close to the results of earlier studies, as shown in table 3.1.

Fig. 3.4 Optical micrograph of YBCO final sintered at 930 °C

Fig. 3.5 Optical micrographs of YBCO final sintered at (a) 958 °C (top), and (b) 975 °C (bottom). The bars represent 250 μ

Table 3.1 Temperature vs. Average grain size: The comparison

Temperature	Chumbley et al.	This work
930 °C	4.0 μm	3.3 μm
945 °C	16.0 μm	12.7 μm
958 °C	28.0 μm	26.8 μm
975 °C	42.0 μm	37.5 μm

3.3. Magnetization Measurements

SQUID Magnetometer

Quantum Design MPMS (Magnetic Property Measurement System) is a commercial SQUID (Superconducting QUantum Interference Device) magnetometer system. It consists of a superconducting magnet housed in a liquid helium dewar for generating magnetic fields up to 5.5 T, a SQUID and sample chamber in its center, vacuum system, temperature controlling unit to maintain the desired sample temperature between 2 to 400 K, accompanying electronics and an HP computer interfaced for the integrated control of the system at the software level. This equipment provides means for very sensitive measurements of magnetic moments.

Scan length and field inhomogeneity of the magnetometer are the factors that require special attention for accurate magnetization measurements. It has been known that, due to the practical limitations of the solenoid, the magnetic field strength changes slightly along the travel length of the sample. Table 3.2

Table 3.2 Field variation vs. scan length for SQUID MPMS

Scan length (cm)	Field variation (%)
1.0	0.001
2.0	0.005
3.0	0.048
4.0	0.19
6.0	1.4
8.0	5.8

shows the variation of the field with respect to the scan length, specified in the Quantum Design MPMS manual.

As it was pointed out [Y. Xu et al., 1989; Lichtenberger, 1991], the field gradient can read to erroneous results of magnetic moment measurements if hysteretic effects are present. For reversible magnetization measurements, the error is proportional to the field change, so the effect is small. For the hysteresis measurements, the sample can undergo minor hysteresis loops as the sample travels through the SQUID coils due to the inhomogeneous field. Since the value of applied field H is much larger than the magnetization, even small inhomogeneities in the field can lead to a significant error and causes the M vs H curve to decrease at the Meissner slope [Togano et al., 1991], as shown in Fig. 3.6. Therefore, all reversible magnetization measurements were done with no longer than 4 cm scan length. Especially, for the flux creep measurements, 3 cm scan length was used where the field variation along the scan length remains less than 0.05 %.

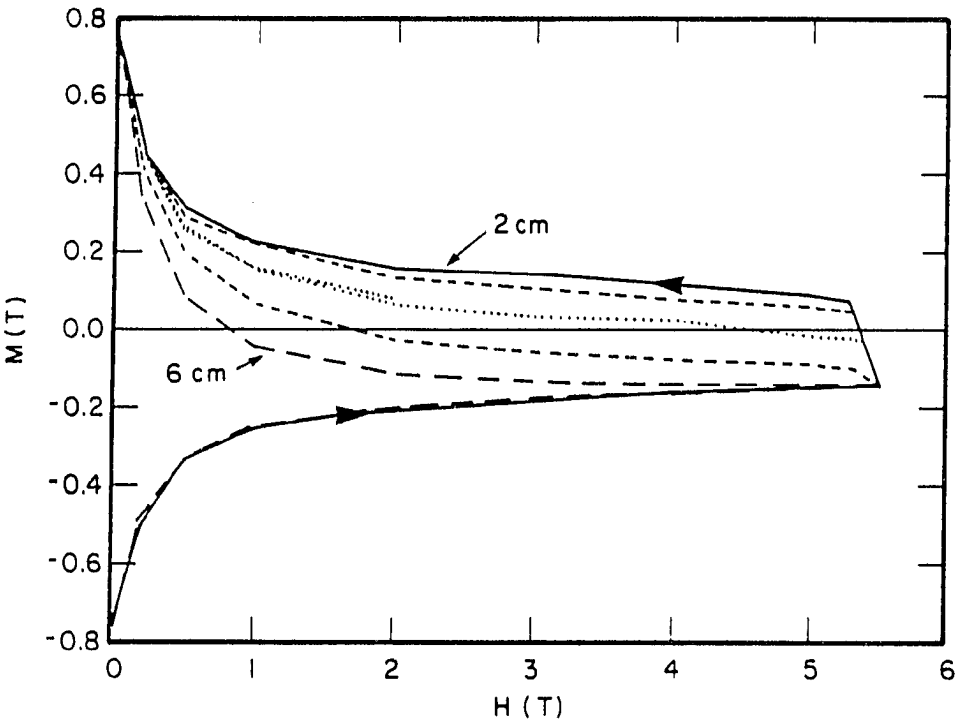

Fig. 3.6 Dependence of ΔM on scan length at 10 K. The scan lengths are 2, 3, 4, 5, and 6 cm with ΔM increasing monotonically as the scan length increases (Togano et al.)

Another problem to be addressed is the instability of the magnetic field at the early stage after applying the field. When a large magnetic field is applied, the actual magnetic field strength increases gradually to reach the set value as the superconducting magnet is being charged by the power supply. There are two magnetic field setting options in the MPMS, which are STANDARD and NO OVERSHOOT. STANDARD mode allows the magnet to reach the set field in shorter time, but then it overshoots the value until it finally reach the target field. For most magnetization measurements, the history of applied magnetic field affect the outcome and this standard setting is not desirable. With NO OVERSHOOT setting, the field does not overshoot the target temperature, but it typically requires about 100 secs till the field reaches the target value. For both setting methods, magnetic field decreases slightly (typically order of 0.01 % of target value) until as long as 20 mins after the field was applied, as it was checked with a flux meter by Steve Sanders of Ames Laboratory, and the Hall probe measurement by another group [Y. Xu et al., 1989] also reported the instability in early 15-30 mins after the magnetic field is applied. This is supposed to be caused by the drift in the superconducting magnet itself and typically it causes the change in the magnetic field by as much as 2 gauss or about 0.01 % of applied field at high field (> 1 T) settings until the field is saturated to a constant value.

Magnetization Measurements

Among various magnetization measurement sequences, Magnetization vs. Temperature (M vs T) measurements form the major part of the experiments. A typical M vs T sequence consists of Zero Field Cooled (ZFC) and Field Cooled(FC) measurements. Due to the nature of the MPMS, temperature control of the

warming up sequence is much more stable than the cooling down sequence. Therefore, both ZFC and FC sequences were measured with the temperature warming up. Magnetization vs. Applied field (M vs H) sequence were used for magnetic field hysteresis measurements. But for the easier background subtraction, in some cases, a series of M vs H measurements were done at various applied fields, the background magnetization was subtracted, and then converted into M vs H data. Magnetization vs time measurements were done for the flux creep measurements.

In all cases, remnant field from the earlier sequence can add to the new field, causing the actual applied field value differ from the target field value. To prevent this remnant field effect, a degaussing sequence was set between each high field magnetization sequences. The degaussing sequence set the magnetic field to 4 T, - 4T, and then 0 T at oscillatory (standard) field setting, effectively removing any remnant field to below 1 gauss level.

3.4. Background Magnetization Subtraction

The paramagnetic impurity background magnetization is quite common for $YBa_2Cu_3O_{7-\delta}$ materials, and most of $YBa_2Cu_3O_{7-\delta}$ used in this study also showed a small paramagnetic background. This background can effectively be subtracted by fitting the normal-state magnetization vs. temperature (M vs T) data from 100 to 260 K to a Curie-Weiss type magnetization functions of the form $M(T) = M_1 + M_2 / (\Theta - T)$, and then subtracting the extrapolation of these functions. Fig. 3.7 shows the normal-state M vs T background data for grain-aligned (H // c) $YBa_2Cu_3O_{7-\delta}$. The difference this correction makes at 82 K and 2 T from

subtracting constant background value at T = 100 K is about 0.3 gauss out of a typical magnetization of 25 gauss. The magnetization data and figures in the following chapters of this thesis reflect this background subtraction.

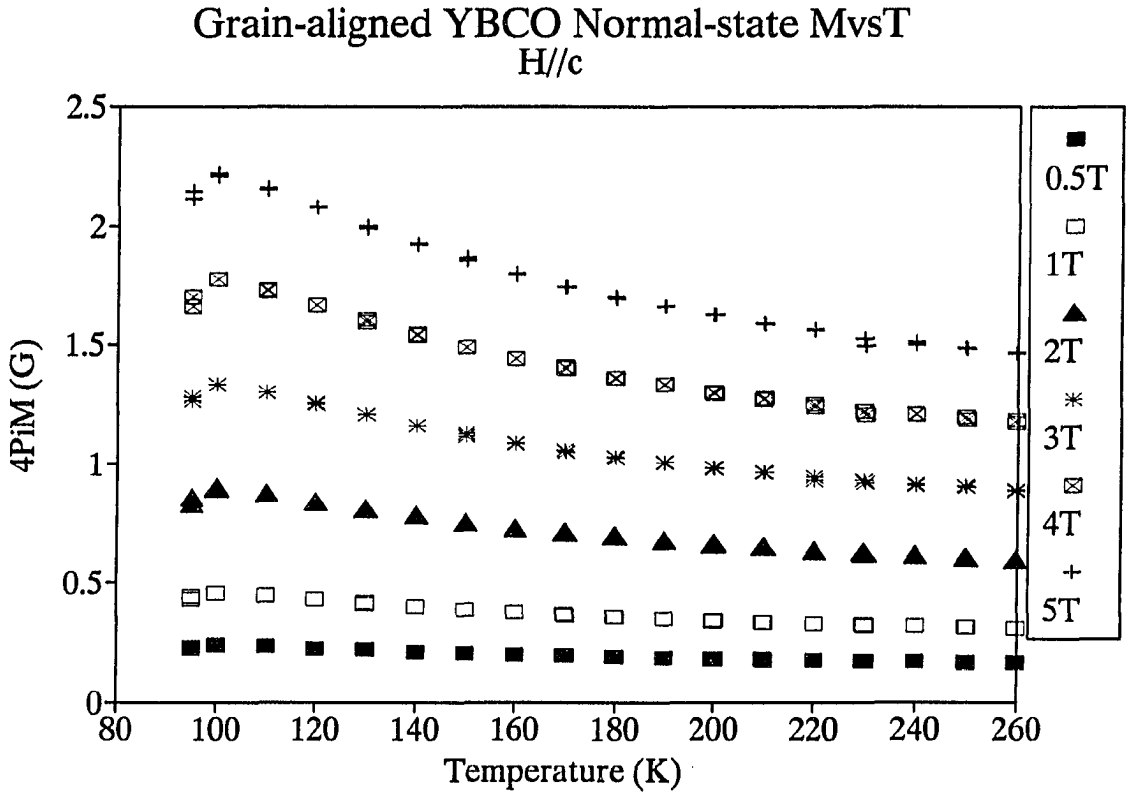

Fig. 3.7 Normal-state magnetization vs temperature data at various applied magnetic fields for grain-aligned YBCO

CHAPTER 4. RESULTS AND DISCUSSION

4.1. Thermodynamic Reversibility in the Fluctuation Regime

Grain-Aligned $YBa_2Cu_3O_{7-\delta}$

The temperature dependence of the free-energy curves derived from grain-aligned $YBa_2Cu_3O_{7-\delta}$ (YBCO) samples with H//c for magnetic fields up to 5 T and at temperature from 80 K to 100 K is plotted in Fig. 4.1. To find the curvature of these lines as given by Eq. (2.4), we fit a series of five points by a central point difference method and evaluate the curvature at the midpoint. Then one data point is deleted from the low-temperature end and one added on the high-temperature end to derive the curvature at the next point.

Results of magnetization-derived specific-heat data C_0-C_H shown in Fig. 4.2 illustrate the same essential features shown by direct C_p data. The onset of the jump in specific heat around 93 K changes very little for all fields up to 5 T. With the Ginzburg-Landau upper critical field H_{c2} being depressed at about 2 T/K [Welp et al., 1989], it might have been expected that the jump in specific heat would have been shifted down about 2.5 K. It is not. Furthermore, once the temperature is below 86 K, the specific heat is essentially independent of magnetic field. The main effect of the applied field is to suppress the magnitude of the jump in specific heat in the fluctuation regime rather than to suppress the temperature of the onset of the jump in C_p. In all three regards, the magnetization-derived specific heats are qualitatively the same as direct C_p results.

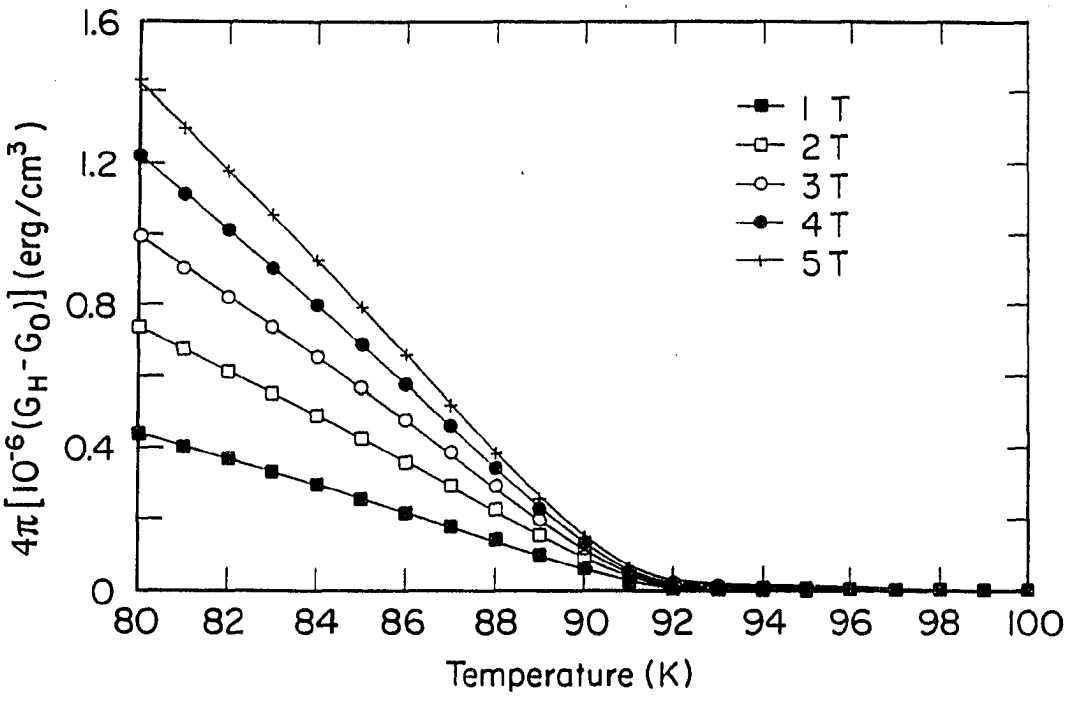

Fig. 4.1 Free energy curves of YBCO. The curvature of G_H-G_0 along the lines of constant H directly give C_0-C_H

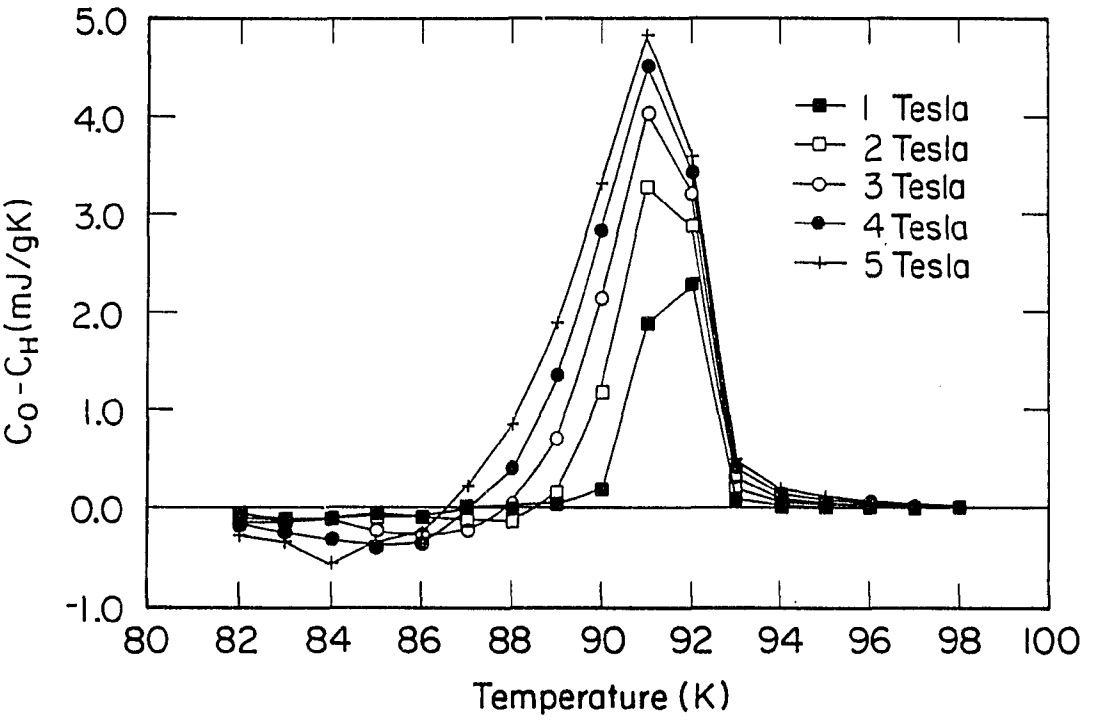

Fig. 4.2 Change in specific heat C_0-C_H vs T at various fields derived from YBCO magnetization data. The field reduces the magnitude of the jump, but it does not change the onset temperature near T_c more than a few tenths of a K. The specific heat is essentially independent of field below 86 K

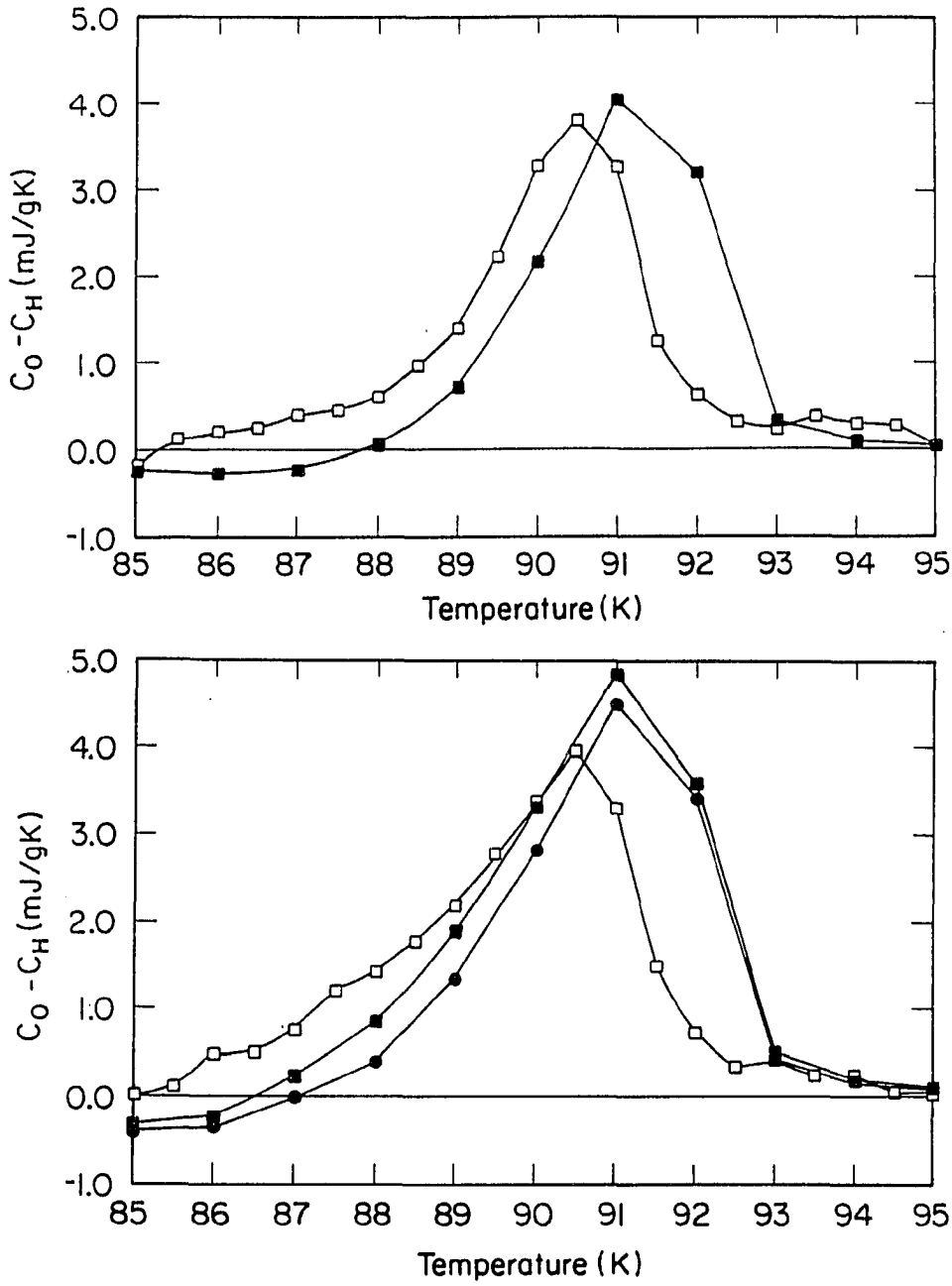

Fig. 4.3 Comparison of specific heat derived from magnetization (solid symbols) with direct C_p measurements (open squares). (a) shows the 3-T data and (b) compares the direct C_p measurements at 4.5 T with magnetization derived data at 4 T (solid circles) and 5 T data (solid squares)

A more direct quantitative comparison of magnetization-derived specific-heat data (open symbols) with the calorimetric data (solid symbols) of Salamon et al. [Salamon et al., 1988] is shown in Fig. 4.3. For the 3-T data on Figure 4.3(a), magnetization derived data shown by the solid squares differ from the direct C_p data by a shift of the peak position by approximately 1 K. This is probably a genuine difference in the T_c of the two samples. The magnitudes of the peaks and the integrated areas under the C_p versus T curves are quite comparable. In Figure 4.3(b), the magnetization data for 4 T (solid circles) and 5 T (solid squares) both have a peak height somewhat larger than the direct C_p data for 4.5 T, and again the position of the peak height is shifted to higher temperatures. There is very little doubt that these two rather different measurements are probing the same free-energy curves and that reversible thermodynamics applies to the fluctuation regime of YBCO.

$Tl_2Ba_2Ca_2Cu_3O_{10}$

Because there are no single-crystal samples of $Tl_2Ba_2Ca_2Cu_3O_{10}$, there cannot be a direct comparison between calorimetric and magnetization-derived values of C_0-C_H. There are, however, direct C_p data on a mixed-phase pallet that can be compared with magnetization data and the results show qualitatively the same effects as for YBCO.

For the $Tl_2Ba_2Ca_2Cu_3O_{10}$ and $Tl_2Ba_2Ca_1Cu_2O_8$, there are no extensive direct C_p data on single crystals of the mixture of these two materials, there are high-precision data on a pellet composed of a mixture of Tl(2:2:1:2) and Tl(2:2:2:3). A comparison of these direct C_p data on a mixed phase sample [Farrell et al., 1987] with the magnetization-derived specific heat of Fang et al. [Fang et al.,

1989] is shown in Fig. 4.4. For the magnetization-derived data, shown by the solid circles, the onset of superconductivity occurs at 125 K and the value of C_0-C_H rises to a peak of 38 mJ/gK at about 117 K. It then quickly falls and becomes zero so that the specific heat is nearly independent of magnetic field in the 1 - 5 T range for temperature below 108 K. The corresponding Tl(2:2:1:2) results were published elsewhere [Fang et al., 1987] and are very similar with the onset of superconductivity at 105 K and a peak in C_0-C_H at 99 K. For the direct C_p measurements, data were taken on a mixed Tl(2:2:1:2) and Tl(2:2:2:3) sample and the measurements were made at 7 T. The results, however shown by the dashed curve, are very comparable to the magnetization derived results. The presence of two phases gives a broader peak than the single-phase samples. but the qualitative features of the peak are the same. There is a peak in the specific heat at the transition temperature T_c, but at temperature below T/T_c=0.9, the specific heat is roughly independent of field. The integrated area under the two curves in Fig. 4.4 have a ratio of 1.4 which is just the ratio of the applied fields, 7 to 5.

Summary

In the region close to T_c, the rounding of the magnetization curve is observed in both the YBCO single-crystal results [Welp et al., 1989] and the grain-aligned results reported here are a direct reflection of the fluctuation observed in the specific heat. There may be sample inhomogeneity factors contributing to the 10-20 % level but the rounding of the magnetization predicts the size of the jumps in specific heat to be essentially the same as those observed in direct measurements. A carefully executed experiment to determine the magnetically derived specific-heat jump at 8 T has been reported by Triscone et al. [Triscone et

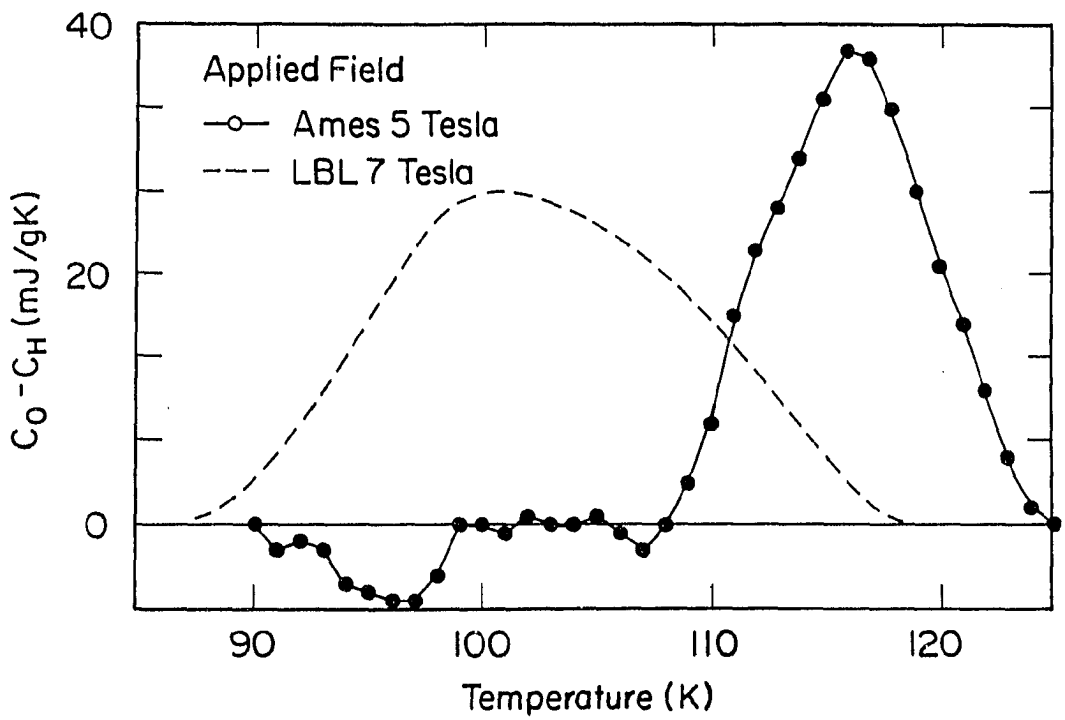

Fig. 4.3 Comparison of magnetically derived specific heat of Tl(2:2:2:3), shown by solid circles, with direct measurements for the mixed-phase Tl(2:2:1:2)-Tl(2:2:2:3) sample of Fisher at el. [Fisher et al., 1988] shown by the dashed line

al., 1989]. The results show a jump of about 60 % of the value reported here. Particularly important is that this sample has a very low paramagnetic background. There are quantitative differences sample to sample on these various measurements, but the results agree qualitatively.

Stated in a slightly different way, the samples are thermodynamically reversible so a free-energy surface can be defined. From the curvature of these free-energy surfaces, the field dependence of the specific heats can be calculated. In the case of YBCO, these values agree with direct C_p results quantitatively with less than 10 - 20 % difference and in Tl-based material, the agreement certainly agree qualitatively. Given the variations observed from sample to sample, this is probably as close an agreement as can be expected. Sample inhomogeneity, if it is present, certainly can contribute to rounding of the magnetization versus temperature curves. The data reported here suggests the rounding is a true reflection of fluctuations seen in the specific heat [Salamon et al., 1988].

4.2. Flux Creep and Specific Heat Jump in $YBa_2Cu_3O_{7-\delta}$: A comparative Study between Grain-Aligned and Melt Textured $YBa_2Cu_3O_{7-\delta}$

Flux Creep

A series of magnetic hysteresis and flux creep measurements were undertaken to compare and study the characteristics of effective pinning potentials for melt-textured and grain-aligned YBCO samples. First, magnetic hysteresis (Fig. 4.5) measurements show much larger $\Delta M = M_+ - M_-$ values for the melt-textured sample. For example, ΔM is about 39,500 gauss at T=10 K and

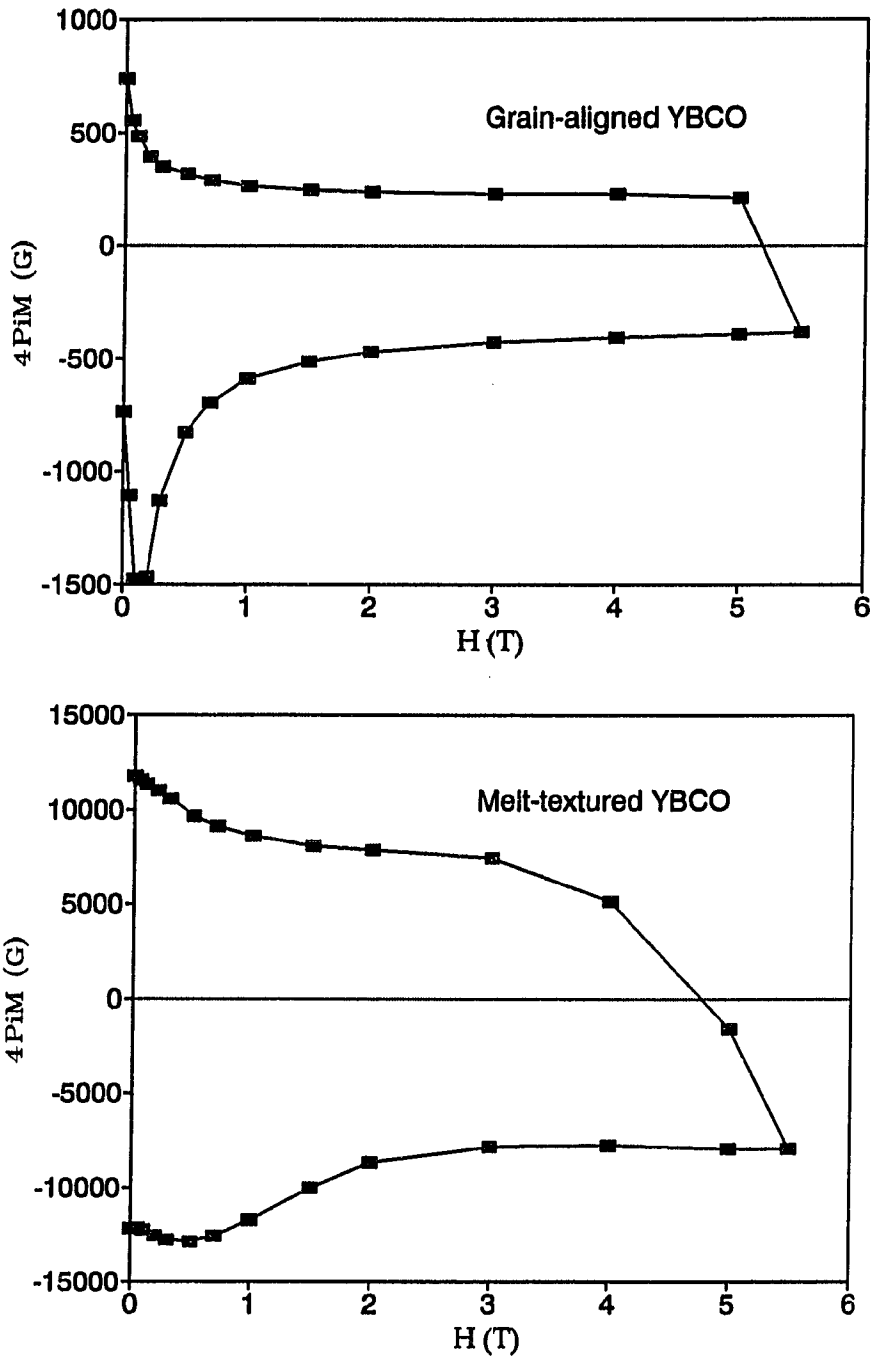

Fig. 4.5 Magnetic hysteresis plots of grain-aligned YBCO (top) and melt-textured YBCO (bottom) at T=10 K

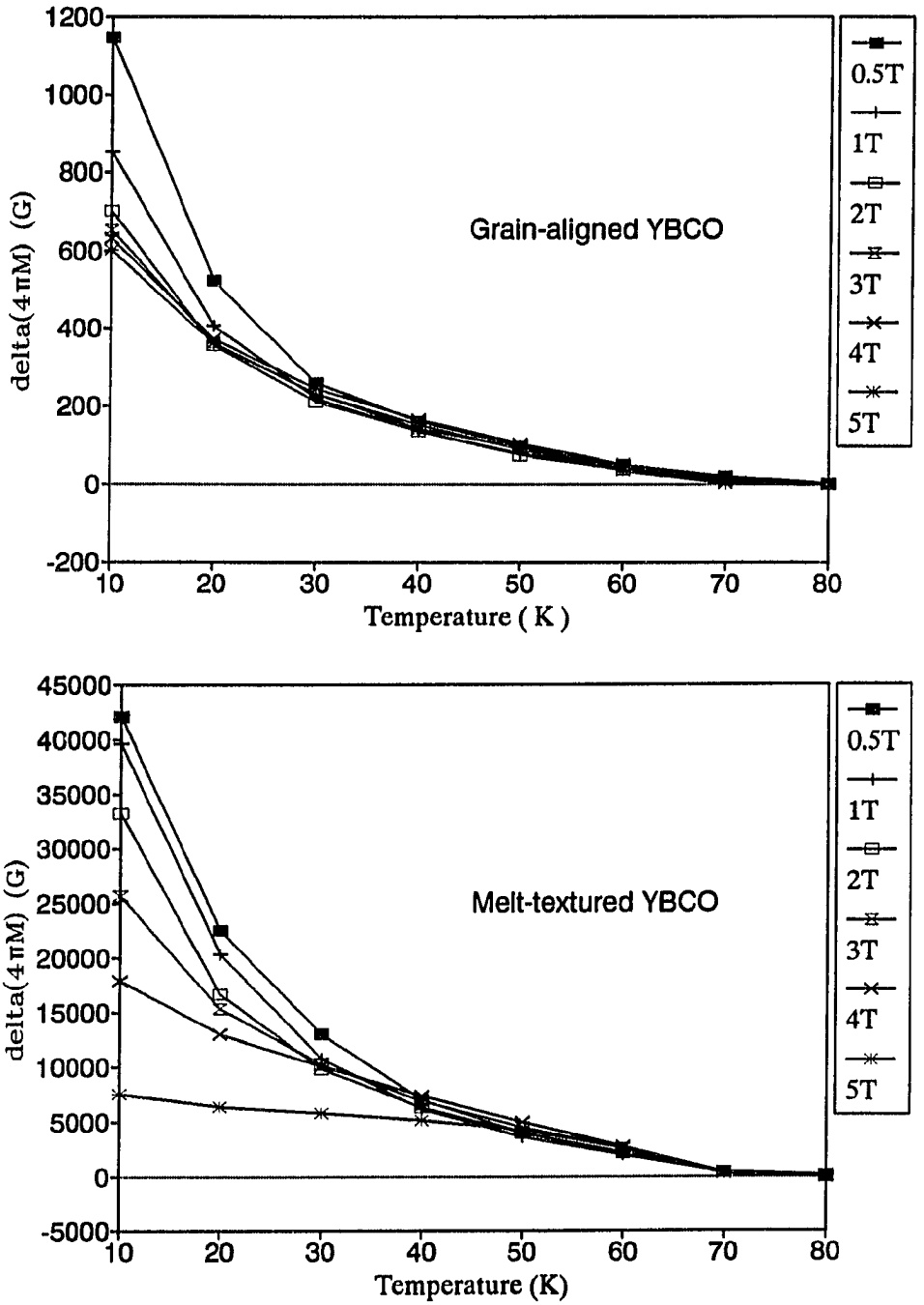

Fig. 4.6 ΔM vs T curves of grain-aligned YBCO (top) and melt-textured YBCO at various fields

H=1 T, while for the grained-aligned sample it is only 850 gauss (Fig. 4.6). Since ΔM is proportional to effective pinning potential, this could mean much higher values of effective pinning potential for melt-textured samples had the other parameters exhibited only marginal changes. From flux creep measurements, however, it was found that the flux creep rates for a melt textured sample is also quite large, and this contributes to decrease effective pinning potential. In fact, the increases in flux creep rates for the melt-textured sample were about enough to cancel out the contribution to effective pinning potential from large ΔM values.

To calculate the effective pinning potential U_o, Beasley's critical state flux creep model [Beasley et al., 1969] is used, where change of magnetic flux on a logarithmic time scale is given by

$$\frac{d\varphi}{d\ln t} = \frac{1}{3}\pi kT\rho^3 \frac{4\pi}{c}\frac{J_c}{U_o} \tag{4.1}$$

where ρ is the radius of a sample and c is the speed light that can be substituted by 10 in practical units (B in G, J_c in A/cm^2). We will assume a cylindrical shape, which is good approximation for both samples. Therefore, an expression for U_o can be found with the relation $4\pi M = \varphi/\pi\rho^2$, given as

$$\frac{dM}{d\ln t} = \frac{1}{30}\rho J_c \frac{kt}{U_o}. \tag{4.2}$$

With $J_c\rho = 15\Delta M$, we get an expression for effective pinning potential in terms of ΔM and flux creep rate:

$$U_o = \frac{1}{2}\Delta M kT \frac{dM}{d\ln t}. \tag{4.3}$$

Yeshurun and Malozemoff [Yeshurun and Malozemoff, 1988] as well as some others [Muller et al., 1987; Beasley et al., 1969] reported logarithmic time dependency of magnetization, while some of recent works [Y. Xu et al., 1989; Suenaga et al., 1991; Thompson et al., 1991; Svedlindh et al., 1991] suggested non-logarithmic time behavior, especially at high temperature and high field region. On the other hand, Weir et al. [Weir et al., 1991] proposed a logarithmic time decay with two distinctive linear regions based on surface pinning effects. In this work, deviation from logarithmic time decay of magnetization is also observed as shown in Fig. 4.7. This becomes apparent above 50 K high field ($H \geq 3$ T) region for the grain-aligned sample and 60 K high field for the melt-textured sample. The difference between two samples is related to the fact that the melt-textured sample has higher irreversible temperature than the grain-aligned.

We calculated the slope of flux creep in logarithmic time scale $dM/d\ln t$ using both earlier and later time windows, and we found these two sets of values agreed within 20 percent up to 60 K, 5 T for the grain-aligned sample and even lower for the melt-textured. Below this temperature and field for each sample, most of flux creep data fit quite well with the logarithmic decay model up to the highest field of 5 T. Occasional deviations of the initial one or two data points in this region is believed to be caused by the unstable nature of the initial magnetic field rather than intrinsic properties, since they tend to disappear with repeated measurements. In this paper, all the results are based on initial linear logarithmic data when there was a noticeable discrepancy in the flux creep rate between earlier and later time. 70 K high field data show clear deviation from linear logarithmic time decay. Applying Beasley's model in this region is quite risky, since the slope $dM/d\ln t$ decreases in time and even becomes saturated to 0 at

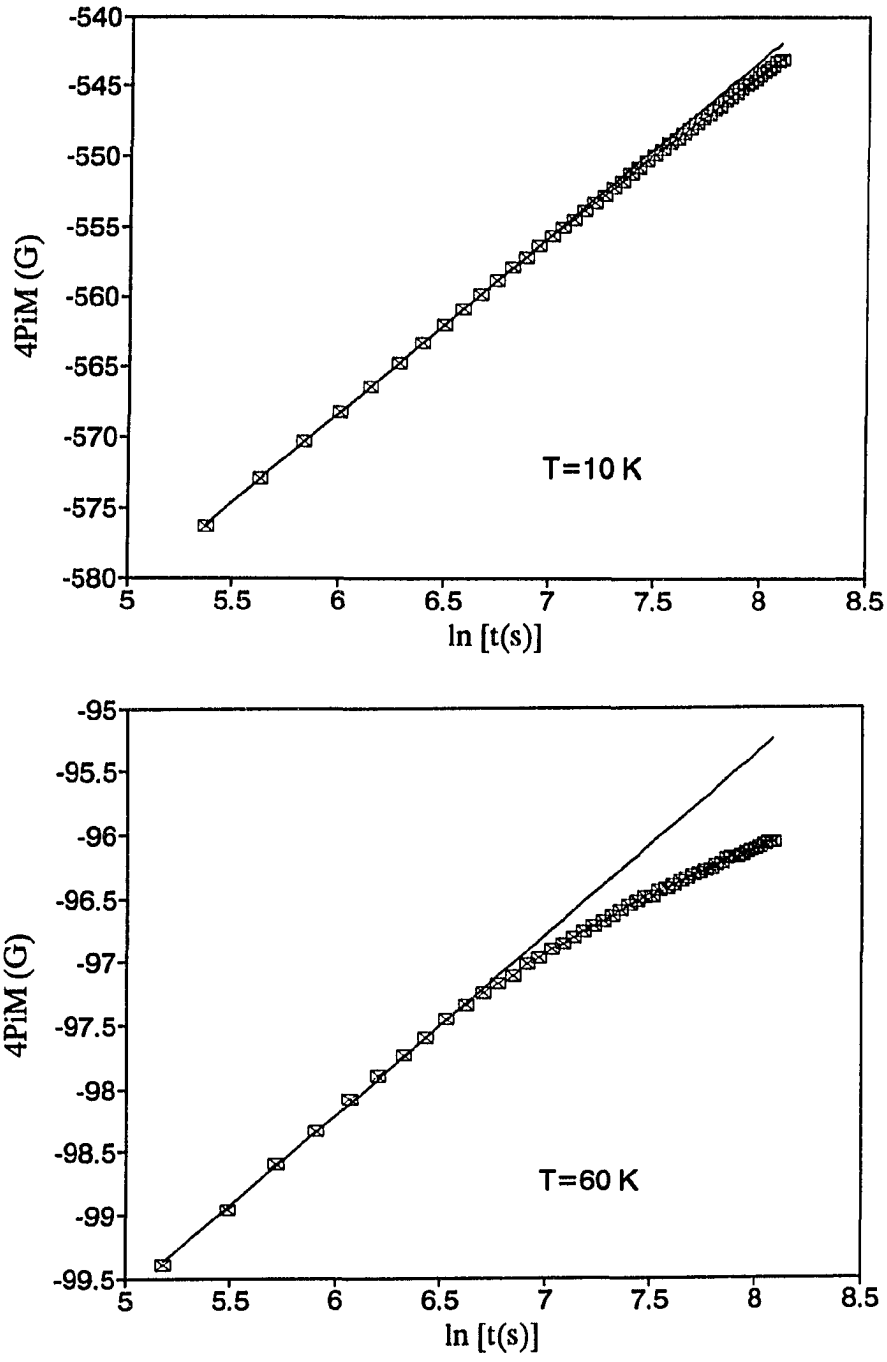

Fig. 4.7 Examples of the flux creep data for the grain-aligned YBCO at H=1 T. At the temperature of 10 K (top) the flux creep shows a good linear dependence on time, while at higher temperature of 60 K (bottom) a clear deviation from linear behavior is seen at long time scale

high magnetic field. For the purpose of comparison, however, the slope and effective pinning potential have been calculated based on initial linear region of $dM/d\ln t$ for 70 K data, and they have to be viewed with these limitations attached.

Resulting effective pinning potential values are quantitatively similar for both samples, as shown in Fig. 4.8. Both samples show peak values of U_0 around the temperature 50 K. At 10K, the peak values are around 100 meV, grain-aligned sample data showing slightly larger values at high fields ($H \geq 3$ T).

The melt-textured sample data shows some artifacts in low field creep measurements, as one can see at low temperature regime of 2 T and 3 T data in the same graph. This is due to the fact the sample is not fully penetrated because of the strong pinning in a melt-textured sample [Lan et al., 1991]. Measurements at fields smaller than 2 T showed the sample is only partially penetrated, even at higher temperatures. When sample is only partially penetrated by magnetic field, the above equations are not valid, and the flux creep rate appears to be smaller; this causes effective pinning potential values to be larger. The grain-aligned sample doesn't show this artifact, since its relatively weak pinning allows the sample to be fully penetrated over the whole range of H in our measurements.

Overall, the effective pinning potentials of these two samples show good agreement when the sample is fully penetrated. This suggests that the strong pinning in our melt-textured sample didn't contribute to change the effective pinning potential, and that although a melt-textured YBCO sample exhibits an order of magnitude stronger flux creep than a grain-aligned sample, weak links in a melt-textured sample are effectively eliminated.

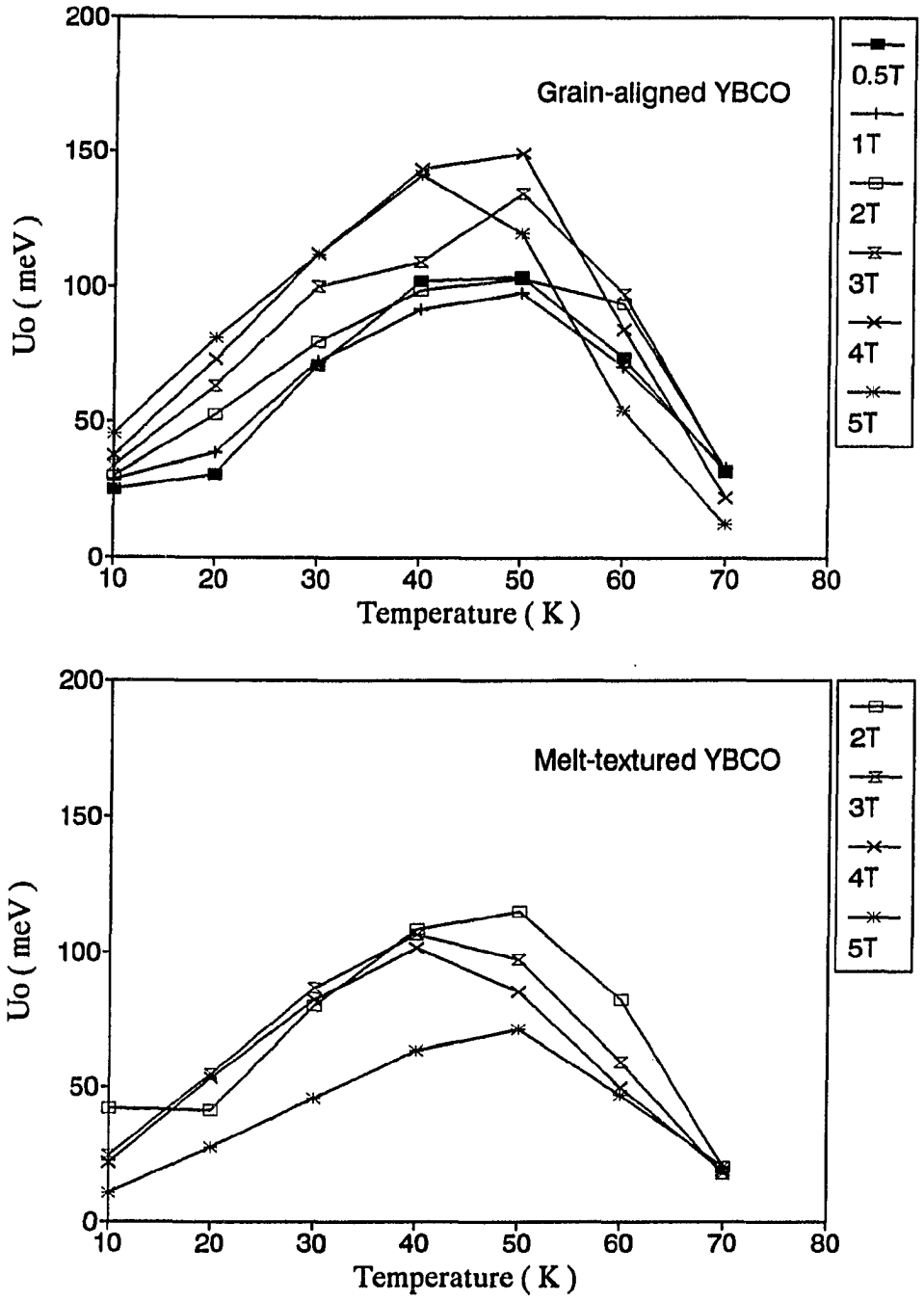

Fig. 4.8 Effective pinning potential U_0 vs temperature for the grain-aligned YBCO (top), and the melt-textured YBCO (bottom). Low field data for the melt-textured YBCO are not plotted here since the sample is not fully penetrated by the magnetic field due to its high pinning

Free Energy and Specific Heat Jump

The change in free energy G(H) with magnetic field H can be calculated by integrating equilibrium magnetization M over H [Athreya et al., 1988]. Since free energy is one of the fundamental thermodynamic quantities as well as one of a few parameters that directly relates magnetic properties of a superconductor with thermodynamic properties, it is of interest to construct the free-energy surface over H-T plane for both melt-textured and grain-aligned YBCO samples and compare them. Here, a problem we encountered was that the melt-textured YBCO sample has a very narrow reversible region below T_c at low magnetic fields. While it is possible to use the Bean model [Bean, 1962] to slightly extend the temperature window below the irreversible temperature by averaging field cooled and zero field cooled magnetizations, it is valid only a few degrees below T_c for the melt-textured sample before its zero field cooled magnetization starts to saturate. Therefore, the free-energy differences use 2 T free energy values as the reference values rather than zero field values are calculated. In this case, the change in free energy is given by the equation

$$G_H - G_{2T} = -\int_{2T}^{H} M dH', \text{ where } M = \frac{1}{2}\left(M^+ + M^-\right) \tag{4.4}$$

Fig. 4.9 illustrates the free-energy surfaces over the H-T plane for both sample melt-textured and grain-aligned samples. The free-energy surface of each sample shows rounding around T_c, and the curvature of this rounding decreases rapidly just several degrees of temperature below T_c. While the free energy for the grain-aligned sample is slightly higher than that of the melt-textured at a given

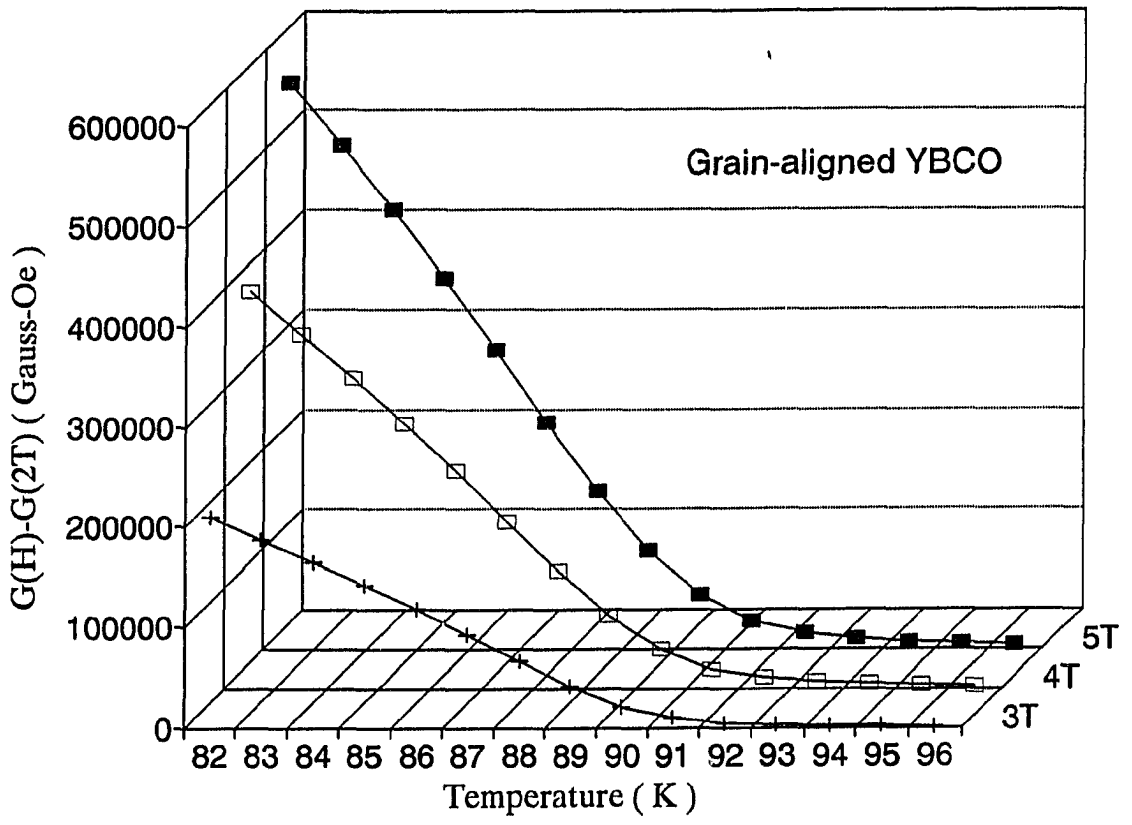

Fig. 4.9 (a) Free energy surface G_H-G_{2T} of the grain-aligned YBCO, where the 2T free energy data are used as reference values for a comparison with the melt-textured YBCO data

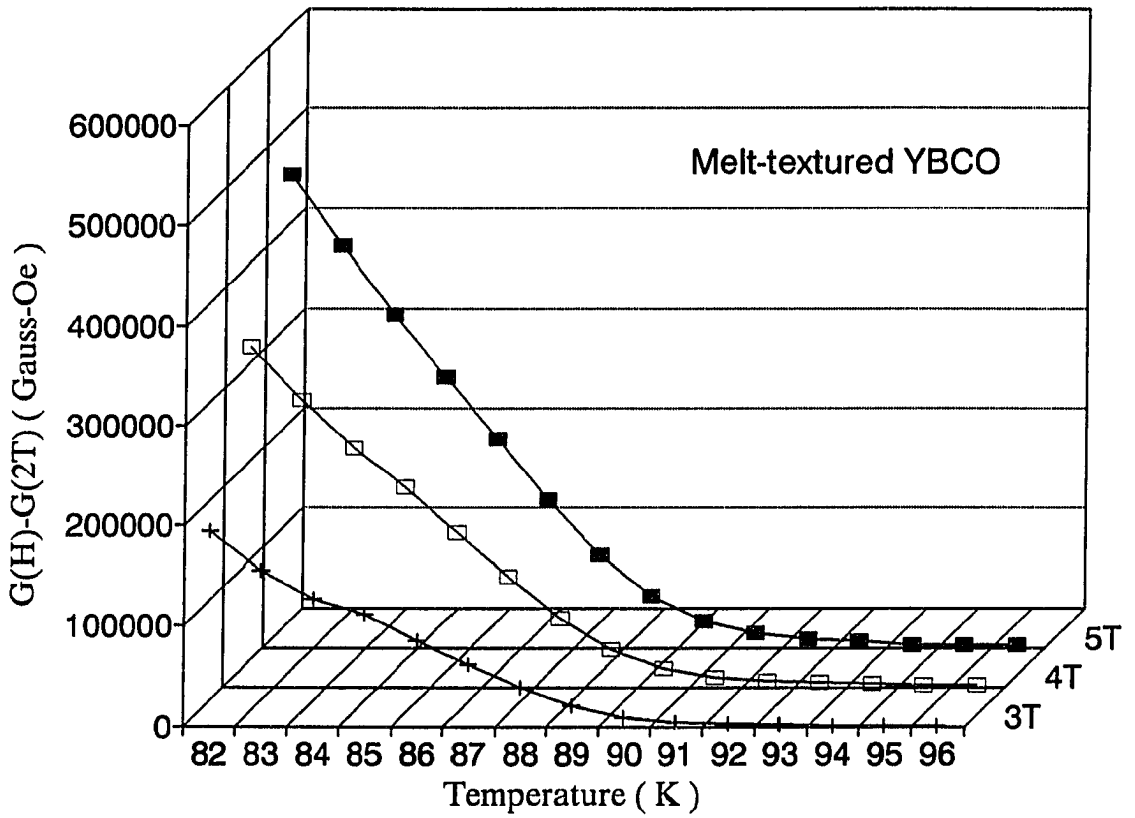

Fig. 4.9 (continued) (b) Free energy surface G_H-G_{2T} of the melt-textured YBCO, where the 2T free energy data are used as reference values

temperature, these curves almost completely overlap up to 6-7 K below T_c if one set of curves is shifted along the temperature axis by about 1 K, which is approximately the difference in T_c between the two samples.

The curvature of free-energy vs temperature is directly related to changes in specific heat by following thermodynamic relation

$$C_{2T} - C_H = T\frac{d^2}{dT^2}(G_H - G_{2T}) \tag{4.5}$$

As one can predict from the overlapping of curves in free-energy curves, calculated specific heat jumps near T_c for both samples show good agreement as plotted in Fig. 4.10. These values are calculated by five-point-central-difference sliding fit, as discussed earlier [Gohng and Finnemore, 1990]. All three peak values at 3 T, 4 T and 5 T agree within 10 % for both samples. Considering these specific heat jump values are results of double derivatives, which are very sensitive to even small noises in the free-energy curves, they show surprising similarities in peak values as well as in shapes. Therefore, we have found the thermodynamic properties of these two samples are quite comparable; the agreement in specific heat jumps being a good example.

The free energy per unit length of a vortex in the melt-textured sample is essentially the same as for the small single crystals inside the grain-aligned sample, suggesting the similar line energies for these rather different samples. Although the magnetization at temperatures much lower than T_c show great discrepancies between melt-textured and grain-aligned YBCO samples, in the thermodynamically reversible regime near T_c they become practically identical, displaying close thermodynamic properties.

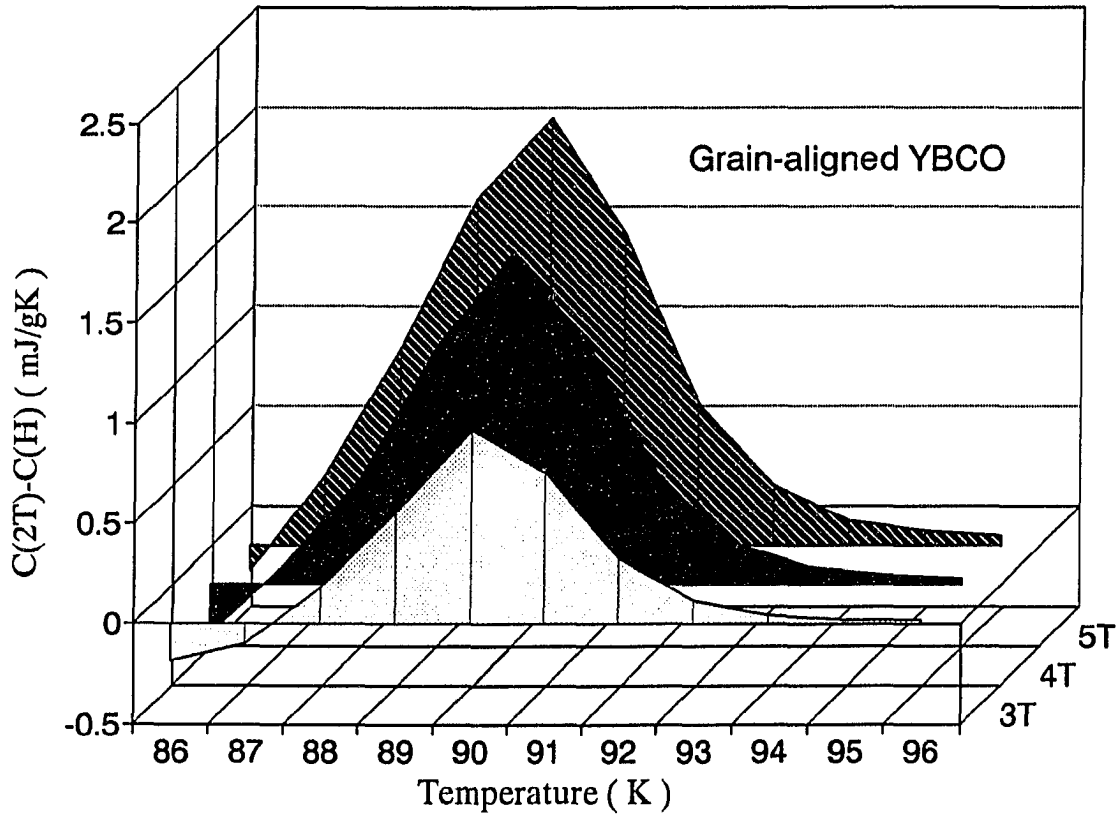

Fig. 4.10 (a) Specific heat jump C_{2T}-C_H of the grain-aligned YBCO, where the 2T specific heat data are used as reference values for a comparison with the melt-textured YBCO data

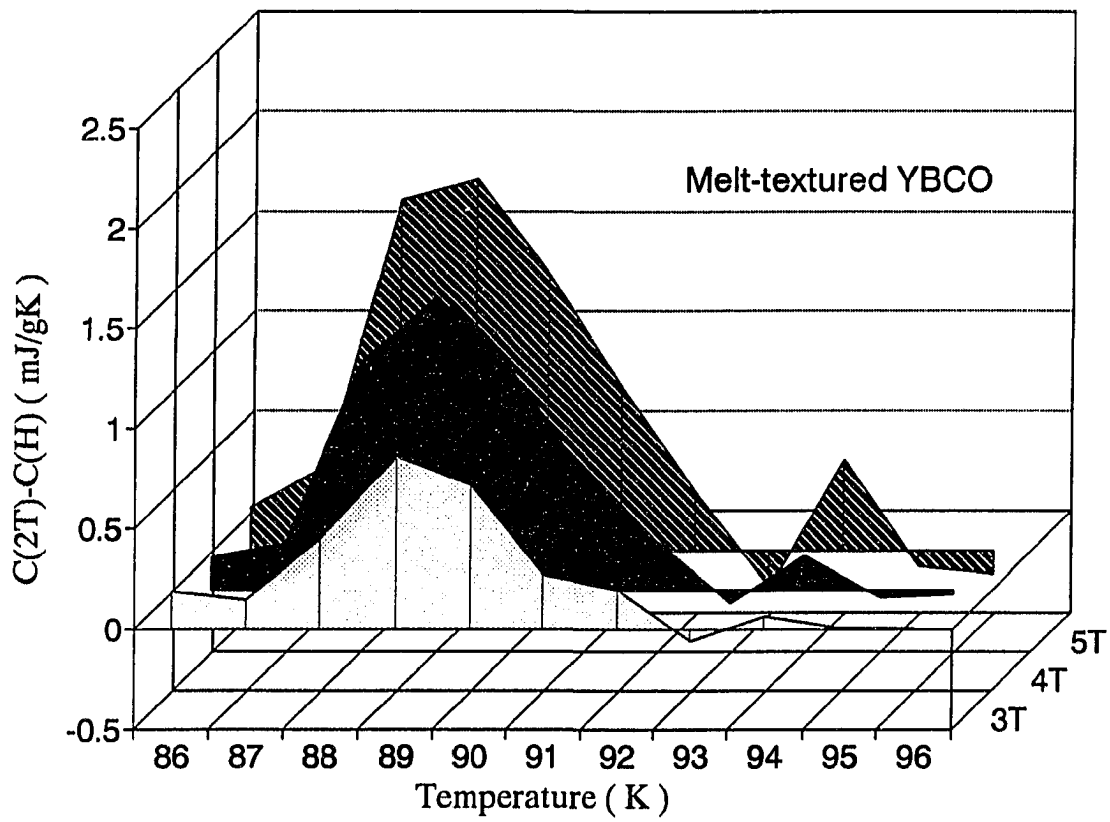

Fig. 4.10 (continued) (b) Specific heat jump C_{2T}-C_H of the melt-textured YBCO, where the 2T specific heat data are used as reference values

4.3. Critical Fields and Vortex Structure of $YBa_2Cu_3O_{7-\delta}$ Derived from Reversible Magnetization

Ginzburg-Landau Parameter and Critical Fields

M(H) data at each temperature in the region from 82 K to 90 K are constructed from a series of M(T) data (from which the background values were already subtracted) at various applied magnetic fields. This results in M(H) data free of background magnetization. These data were fitted to a Hao and Clem's equation, Eq. (2.36). When the magnetization is small compared to the applied field, the demagnetization effect can be neglected and the internal field H becomes equal to the applied field. These equations are written in dimensionless units, in which the magnetization and the applied field are given in units of $\sqrt{2}H_c$. When fitting the data, both κ and H_c are assumed as independent fitting parameters for the magnetization data taken at each temperature between 82 K and 89 K with the temperature interval of 1 K. Since the magnetization data are taken with H parallel to the c-axis, the fitting gives κ_c. Fig. 4.11 shows the results of fits to some of these data. The fits results in a relatively small change of κ_c over the observed temperature range. If all the M(H) data are fit to a curve using the average κ_c value of 72, it's a reasonably good fit as shown in Fig. 4.12. This agrees with the scaling behavior reported by Hao et al., however, this apparent scaling behavior is due to the κ_c being slowly varying function of temperature near T_c, and this small deviation is not easily seen on the scaled curve, as Hao et al. commented the fit gives good result with $\tilde{\kappa}_c \pm 5$ for their single crystal data.

Fig. 4.13 shows the calculated κ_c as a slowly decreasing function of temperature within 82 K to 88 K temperature region. $\kappa_c(T)$ decreases linearly from

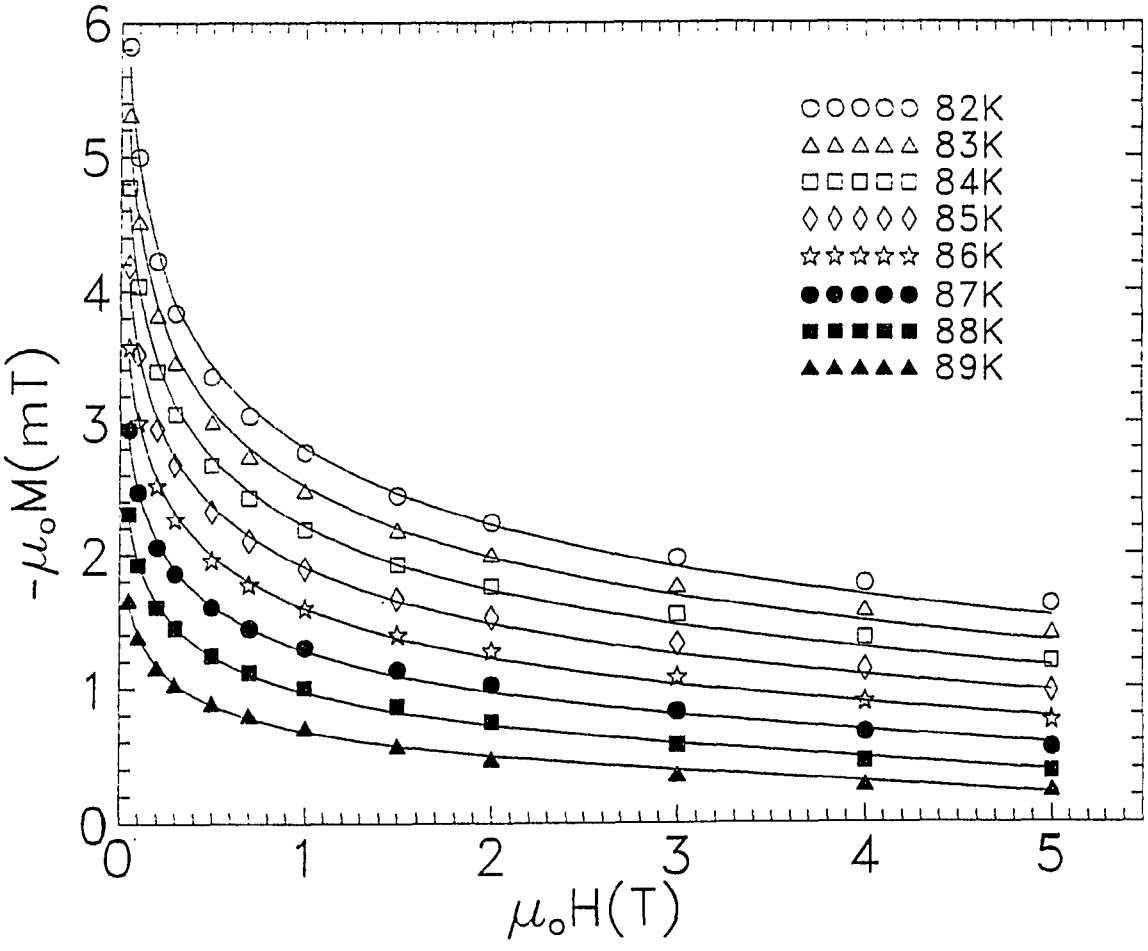

Fig. 4.11 Comparisons of the Hao-Clem fitting results, shown as curves, with the YBCO magnetization data at various temperatures

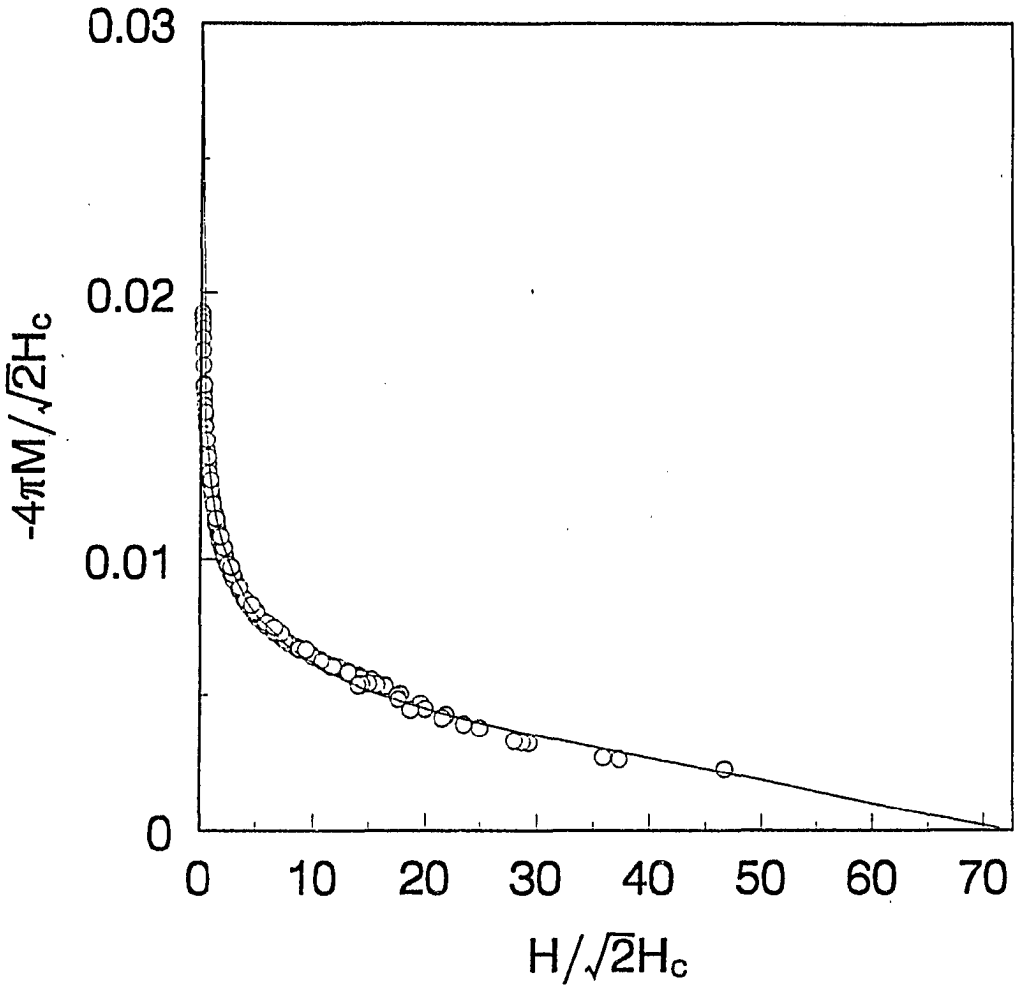

Fig. 4.12 The scaling behavior of the M(H) data shown in dimensionless units. In this figure, a series of M(H) data at different temperatures between 81 and 89 K are scaled by $\sqrt{2}H_c$ showing reasonably good agreement with the universal curve drawn for $\kappa_c = 72$

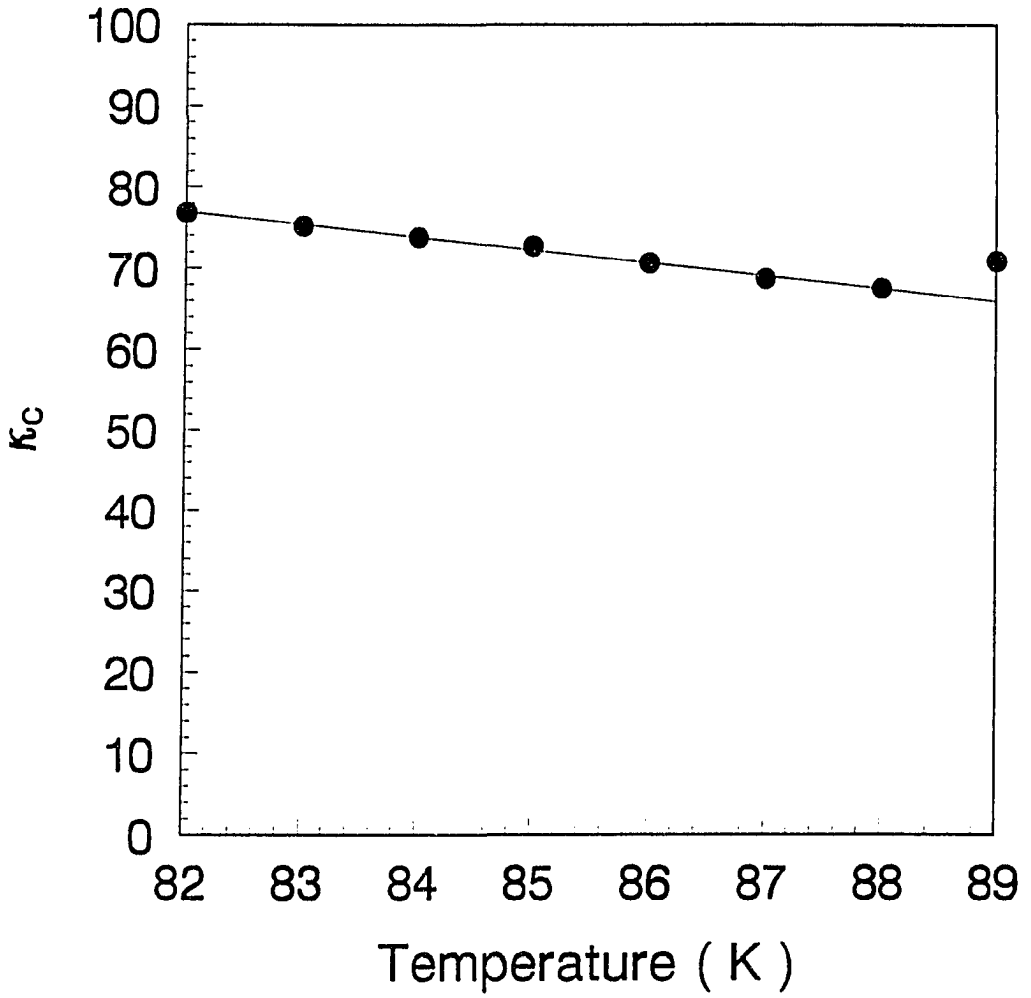

Fig. 4.13 Temperature dependence of the Ginzburg-Landau parameter κ_c, determined from Hao-Clem model fittings to M(H) data with H parallel to c-axis

76.9 at 82 K to 67.5 at 88 K. The slight increase of κ_c at 89 K is thought to be a result of the increasing fluctuation effects as the temperature approaches T_c.

Another parameter determined directly from this fitting is $H_c(T)$, which is shown in Fig. 4.14. $H_c(T)$ shows good linear behavior in T and the linear extrapolation of $H_c(T)$ yields T_c = 92.5 K. Fitting the data to the BCS temperature dependent $H_c(T)$ theoretical curve (which is nearly linear) calculated by Clem [Clem, 1966] as,

$$\frac{H_c}{H_c(0)} = 1.7367\left(1-\frac{T}{T_c}\right)\left[1-0.2730\left(1-\frac{T}{T_c}\right)-0.0949\left(1-\frac{T}{T_c}\right)^2\right], \qquad (4.6)$$

results in a slightly better fit, and it gives similar result of $T_c = (92.4 \pm 0.6)\,K$ along with $H_c(0) = (1.18 \pm 0.01)\times 10^4$ Oe. These T_c values are in good agreement with the $T_c = 92.5 \pm 0.1\,K$ determined as the onset temperature in the 5 Oe M vs T curve. The unusually high T_c value of 94.1 K from Hao et al's BCS fitting of $H_c(T)$ from the single crystal magnetization, may have been a result of forcing κ_c to be a constant in temperature when calculating $H_c(T)$.

$H_{c2}(T)$ can be calculated from a simple relationship

$$H_{c2} = \sqrt{2}\kappa H_c \qquad (4.7)$$

where both κ and H_c are functions of temperature. The result is shown in Fig. 4.15 and compared with the case of κ_c=72, which is the average κ_c value. The apparent linear temperature dependence of κ_c qualitatively agrees with the theoretical calculations of κ based on Maki-de Gennes theory for both clean [Eilenberger, 1967] and dirty [Caroli et al., 1965] limits, where the κ is approximately a linearly decreasing function of the temperature near T_c. However,

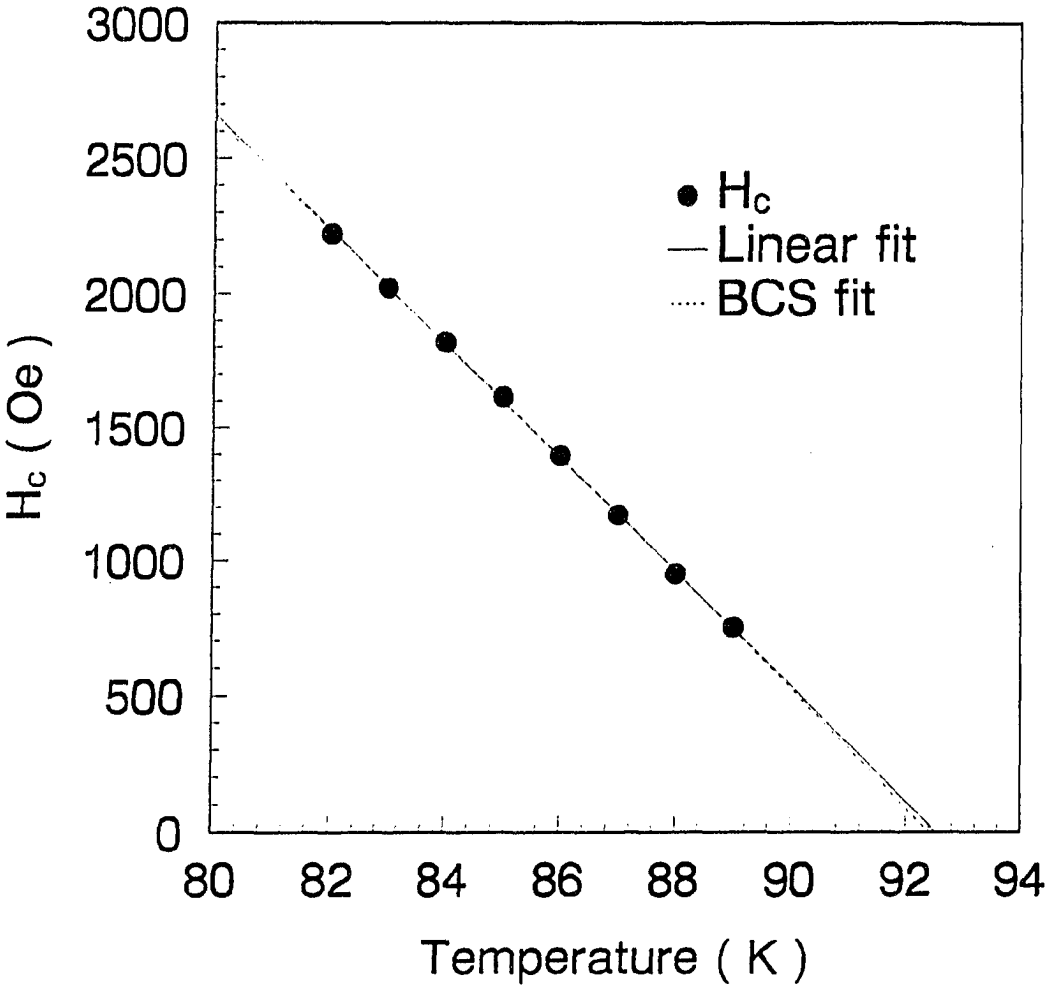

Fig. 4.14 Temperature dependence of the thermodynamic critical field H_c. Both BCS and linear fitting results are also shown in the figure. T_cs determined as the x-axis intercepts from both fittings are 92.4 K and 92.5 K, respectively

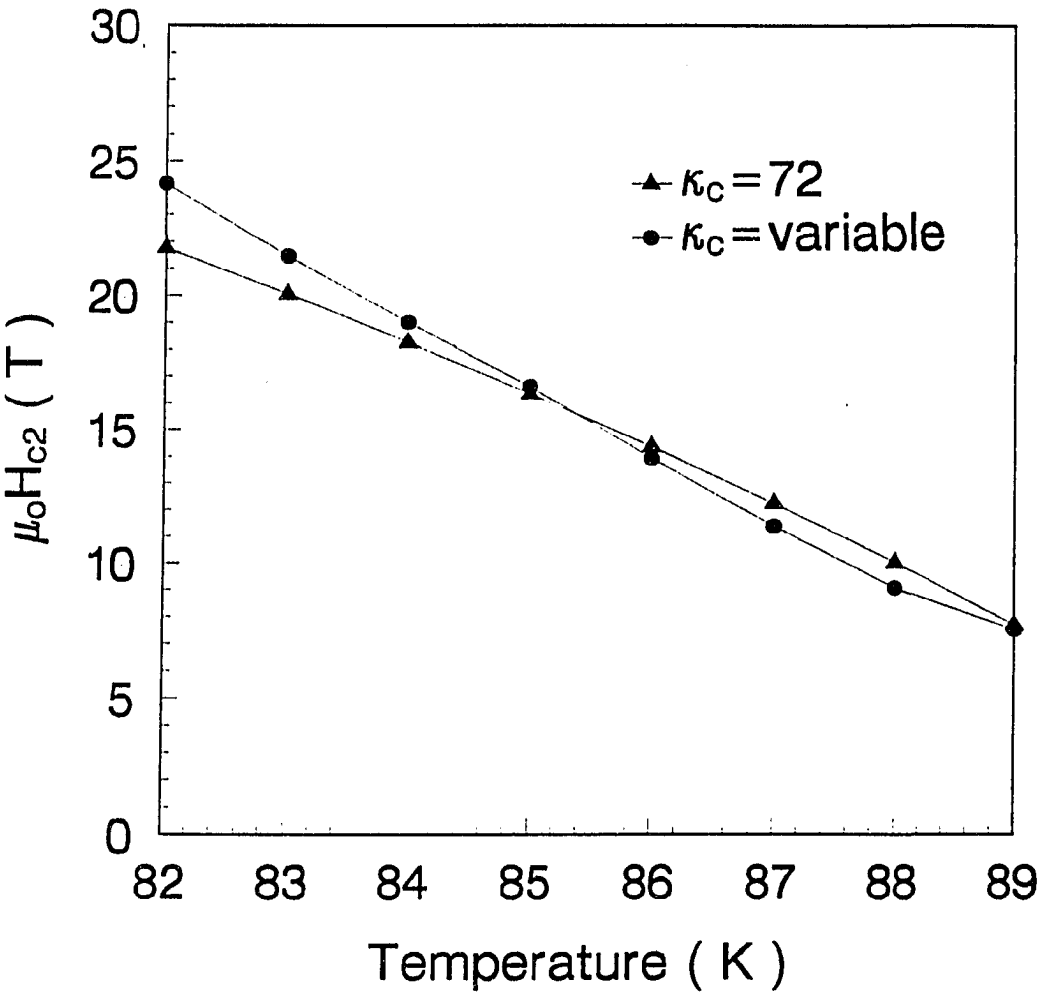

Fig. 4.15 Upper critical field vs temperature. Results determined from the Hao-Clem model fittings with both the fixed and the temperature dependent κ_c are compared

the slope of $-d\kappa_c/dT = 1.57/K$ is higher than both of the theoretical calculations. Along with this linear temperature dependence of κ_c, BCS fitting of $H_c(T)$ gives the slope of $-dH_{c2}/dT$ that gradually decreases from 2.26 T/K at T = 82 K to 1.90 T/K at T_c.

The penetration depth λ is related to H_c and κ by

$$\sqrt{2}H_c = \frac{\kappa\varphi_0}{2\pi\lambda^2} \tag{4.8}$$

with which $\lambda_{ab}(T)$ can be calculated from the $\kappa_c(T)$ and $H_c(T)$ results (here $\varphi_0 = hc/2e = 2.07\times10^{-7}\ G\,cm^2$ is the flux quantum). BCS calculations of $\lambda_{ab}(0)$ [Mühlschlegel, 1957] with these $\lambda_{ab}(T)$ data gives $\lambda_{ab}(0) = 1310 \pm 30\ \mathring{A}$ and coherence length of $\xi_{ab}(0) = 18 \pm 1\ \mathring{A}$.

Fluctuation and Upper Temperature Limit of the Hao-Clem Equation

With the rapid increase of fluctuation above 89 K, the M(T) data do not fit the Hao-Clem theory [Lee et al., 1989]. If the data are forced to fit the theory, values of $\kappa(T)$ diverges above 89 K. Fig. 4.16a is a magnified view of M(T) data near T_c where the crossover is observed. This is thought to be a same fluctuation effect observed in high field measurements of conventional superconductors [Tinkham, 1975]. Fluctuational diamagnetism grows as the applied field increases, and near T_c, where this fluctuational diamagnetism becomes dominant, the magnetization gets larger in magnitude for the higher applied field data. This makes a crossover inevitable somewhere near T_c.

Although it may require a complete analysis following detailed fluctuation models [Prange, 1970; Kurkijärvi et at., 1972; Lee and Payne, 1971] to describe

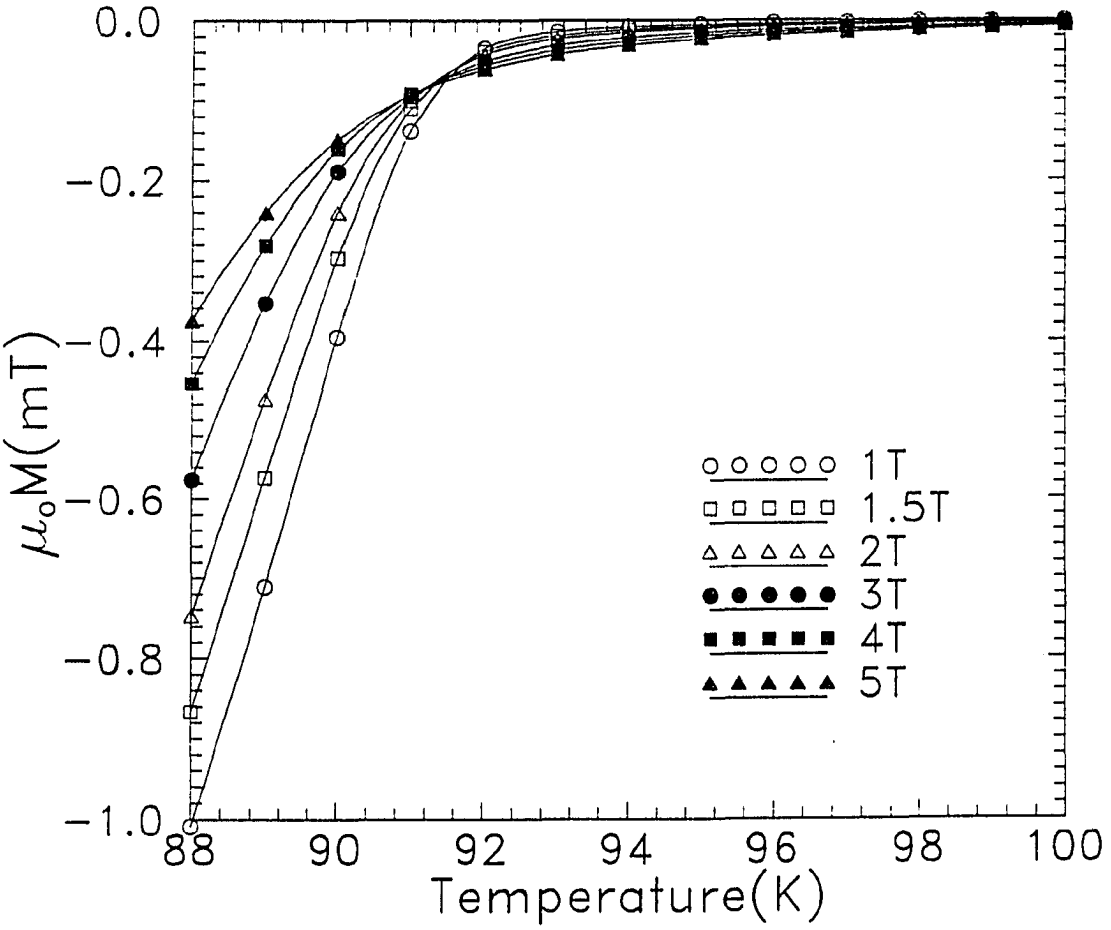

Fig. 4.16 (a) Crossover in magnetization vs temperature data due to the fluctuational diamagnetism near T_c

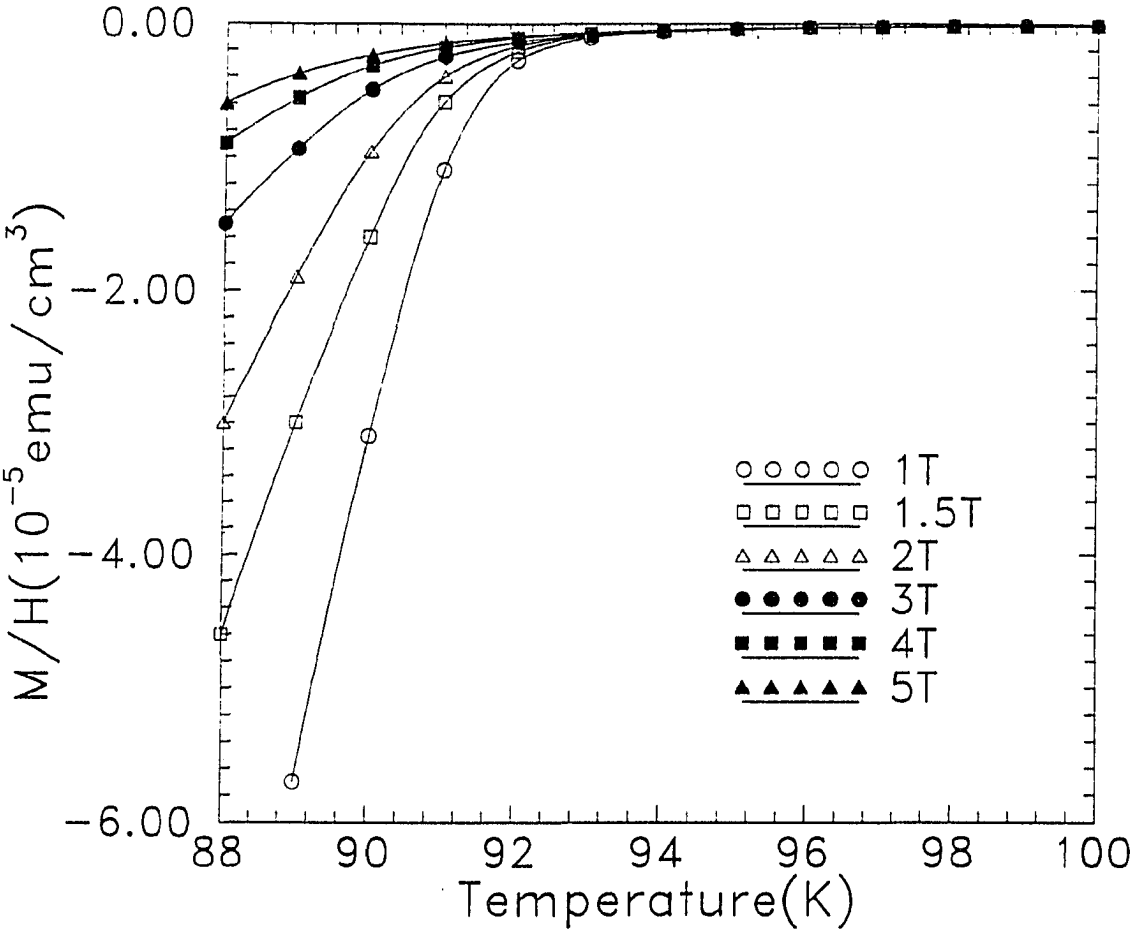

Fig. 4.16 (continued) (b) M/H vs temperature plots of the same data shown in (a). Notice the crossover disappears in this figure

the behavior of the crossover, a simple M/H vs T plot is sufficient to show there is indeed nothing special about the crossover. Fig. 4.16b shows the crossover has disappeared in M/H vs T plot. In case of YBCO, which shows 3D like fluctuation, the crossover is barely observable due to its relatively small fluctuational contribution. However, for $Bi_2Sr_2CaCu_2O_8$ and $Bi_2Sr_2Ca_2Cu_3O_{10}$ (BSCCO 2:2:1:2, 2:2:2:3) that show more 2D behavior [Farrell et al., 1989; Martin et al., 1989; Naughton et al., 1988], the crossover is observed in larger scale farther away from T_c [Kes et al., 1991; Kritscha et al., 1991], limiting the availability of Hao and Clem's model to the temperature region much lower than T_c. These larger scale crossovers, however, also disappear in M/H vs T plots.

Vortex Structure Derived from Magnetization Data

Once $\kappa(T)$ and $H_{c2}(T)$ values are known from the magnetization data, the Hao-Clem model allows the order parameter and the magnetic flux density function to be determined for a single vortex. The assumed trial form for the order parameter is

$$f = \frac{\rho}{\sqrt{\rho^2 + \xi_v^2}} f_\infty \,, \tag{4.9}$$

and this leads to

$$b_{0z} = \frac{f_\infty K_0\left(f_\infty \sqrt{\rho^2 + \xi_v^2}\right)}{\kappa \xi_v K_1(f_\infty \xi_v)} \tag{4.10}$$

for the magnetic flux density. Here, f_∞ and ξ_v are the variational parameters defined in Eqs. (2.33) and (2.34) and ρ is the distance from the vortex core in units

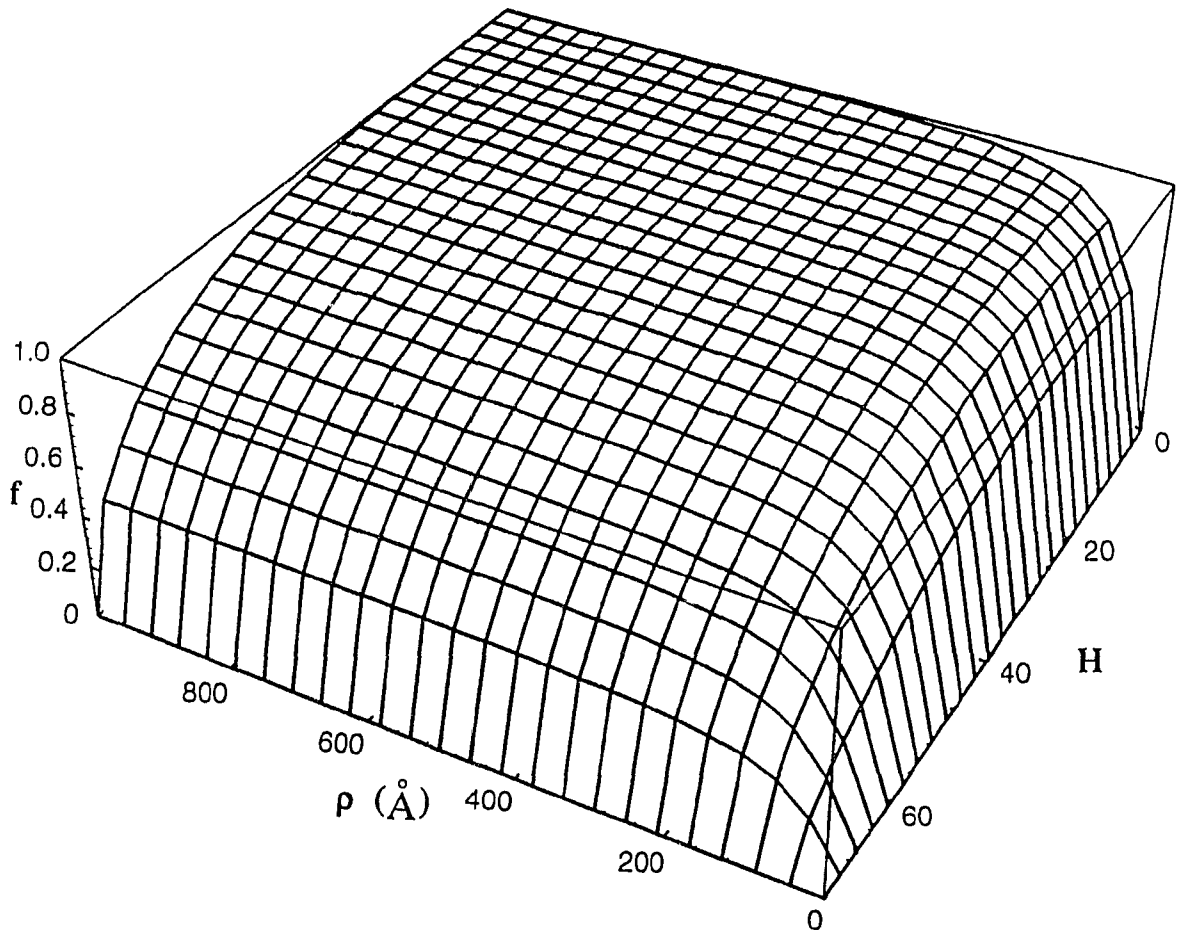

Fig. 4.17 Three-dimensional surface plot of the order parameter at T=85 K, constructed based on the Hao-Clem model fitting results. Applied field H is given in dimensionless unit for which the scaling factor is $\sqrt{2}H_c$(T=85) = 2283 Oe, and ρ is the distance from the vortex core

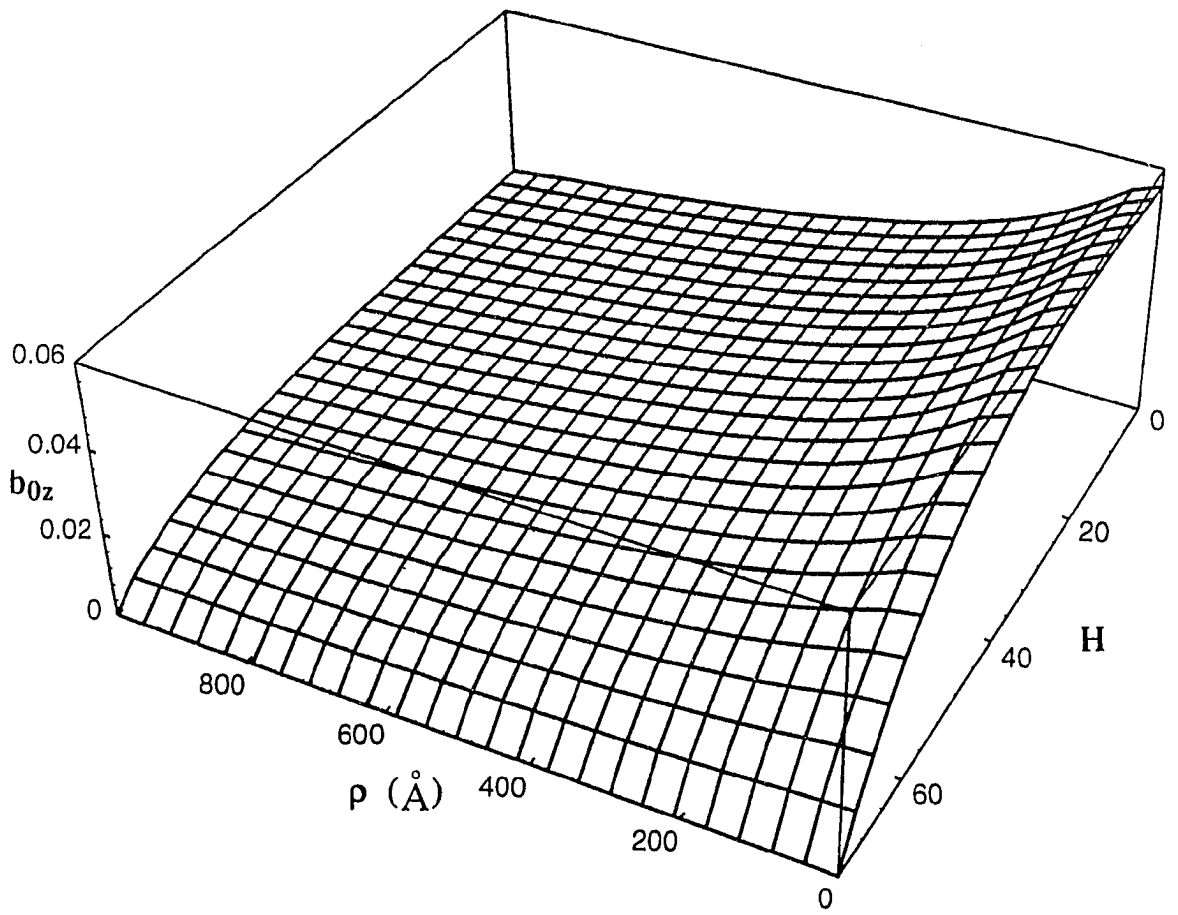

Fig. 4.18 Three-dimensional surface plot of the magnetic flux density at T = 85 K. constructed from the Hao-Clem model fitting. Applied field H is given in dimensionless unit for which the scaling factor is $\sqrt{2}H_c$(T=85) = 2283 Oe, and ρ is the distance from the vortex core

of λ. Fig. 4.17 and 4.18 are three dimensional plots of the order parameter and the magnetic flux density for an isolated vortex on the (H,ρ) plane based on our fitting result of κ_c = 72.7 and $H_{c2} = 1.66 \times 10^5$ Oe at T = 85K, where H is the applied field and ρ is the distance from the vortex. It is interesting to note that the suppression of the order parameter remains small until the applied field is very close to H_{c2} (Fig. 4.17).

In case of multiple vortices, a simple model of vortex structure is introduced by cutting the order parameter functions in the middle of vortex spacing where they intersect each other with the one in the nearest neighbor. Hao and Clem's order parameter function is independent of the specific vortex structures. Here we assumed hexagonal vortex structure, but any close-packed vortex structure will give reasonable vortex spacing within the accuracy of Hao and Clem's equation. The order parameter functions for an array of vortices at T = 88 K and H= 1 T, 3 T and 5 T are shown in Fig. 4.19. The suppression of the order parameter by the increasing applied field H is easily noticeable in this plot. With the predetermined κ_c(T) and H_c(T) values from the fitting to magnetization data, similar plots can be generated for the given temperature and applied field. Here the actual shape of the order parameter may not be accurate, because the shape of order parameter at the cut should be smoother. Still, this simple model describes the vortex structure reasonably well, and it allows us to calculate average behavior of order parameter with higher accuracy. Therefore, we introduced the average order parameter, defined as

$$\langle f \rangle = \frac{8}{a^2} \int_0^{a/2} f(\rho) \rho d\rho, \qquad (4.11)$$

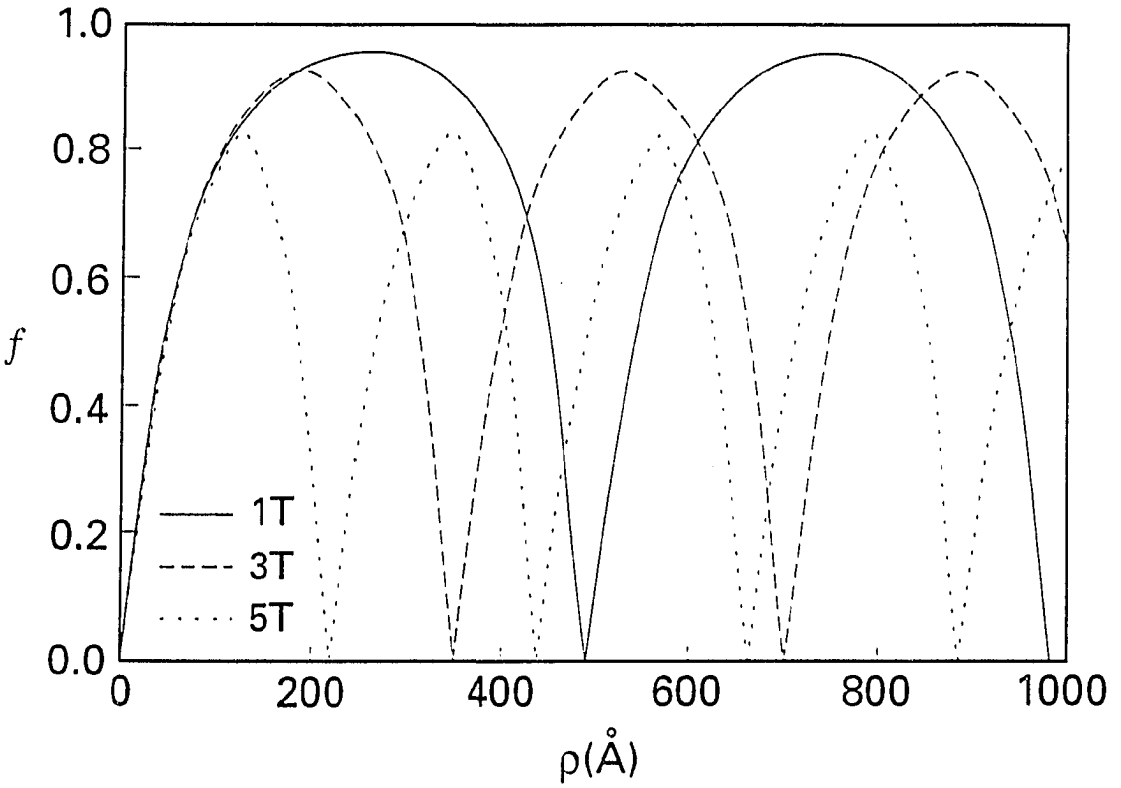

Fig. 4.19 A simple model of the vortex structure for the hexagonal lattice at T=88 K. The suppression of the order parameter at the applied field values of 1 T, 3 T and 5 T are shown

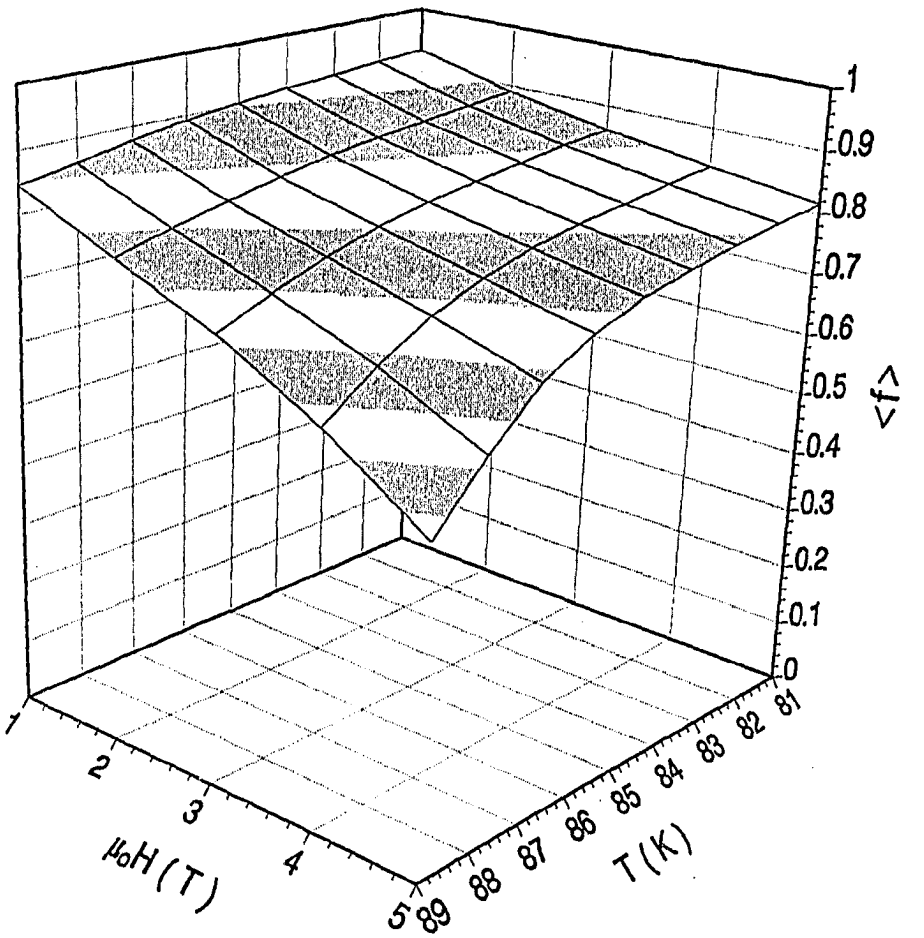

Fig. 4.20 A three-dimensional surface plot of the average order parameter on (H,T) plane. Each band on the surface represents 5 % segment in order parameter strength

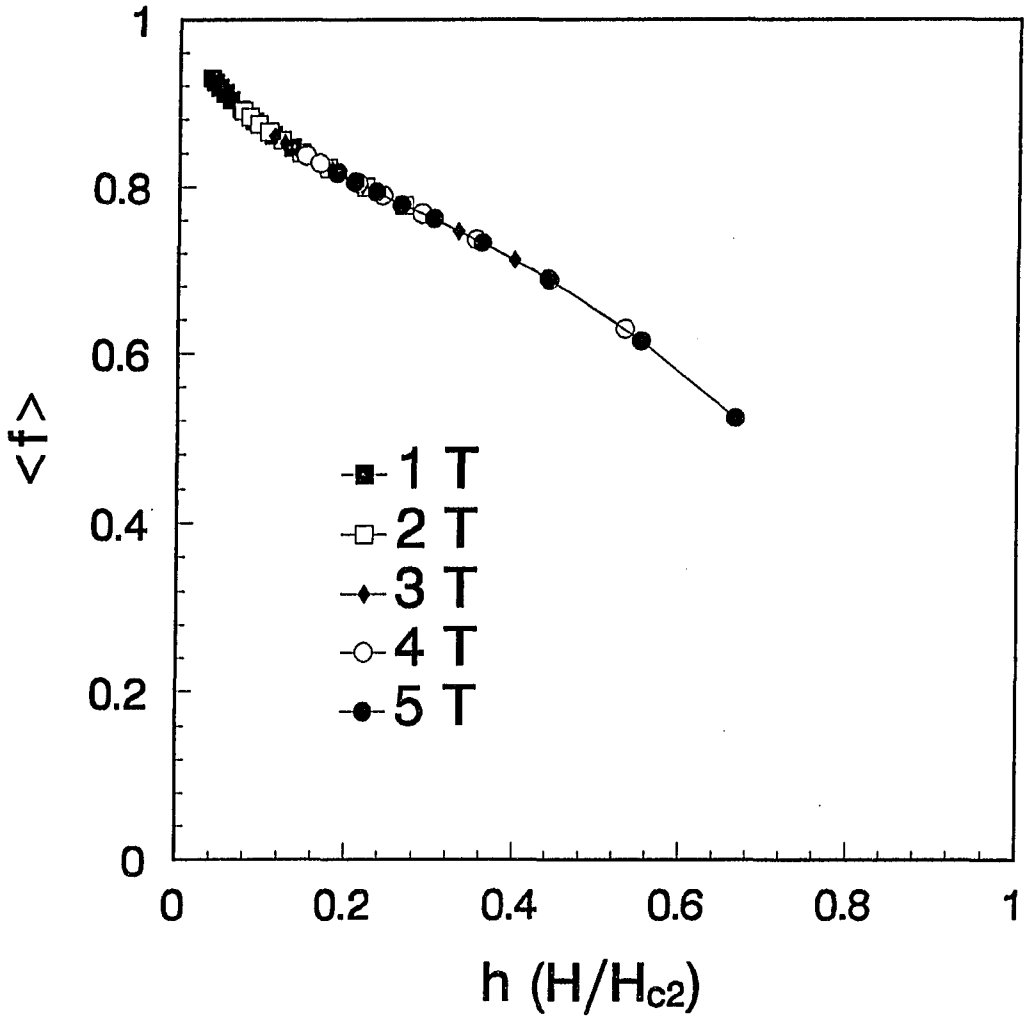

Fig. 4. 21 Plot showing universal behavior of the order parameter on a reduced field ($h = H/H_{c2}$) scale. The $\langle f \rangle(h)$ data for the temperature between 81 K and 89 K falls into a single curve

where a is the vortex spacing for hexagonal vortex structure. Fig. 4.20 is a three dimensional surface plot of $\langle f \rangle$ on the (H,T) plane, which shows the suppression of the average order parameters by 47.7 % at 89 K and 5 T. While there are more detailed theoretical models describing the vortex structure, like the work by Brandt [Brandt, 1972], in which a similar variational approach to Ginzburg-Landau equations was used to calculate the microstructure of the vortex lattice for fixed κ_c values, this plot has a special meaning, since it is based on true $\kappa_c(T)$ and $H_c(T)$ values for our YBCO sample. The average order parameter derived in this study also shows qualitative agreement with Brandt's $\kappa \geq 10$ case calculation. Fig. 4.21 shows the field dependence of $\langle f \rangle$, where $\langle f \rangle$ vs h curves at various temperatures falls into a single curve, representing the universal behavior of $\langle f \rangle$ on a reduced field ($h = H/H_{c2}$) scale.

$Bi_2Sr_2Ca_2Cu_3O_{10}$

Hao-Clem model fittings have been carried on c-axis aligned Bi(2:2:2:3) tape samples to compare with the results of YBCO. The Bismuth family superconductors, Bi(2:2:1:2) and Bi(2:2:2:3) are one of the most anisotropic superconductors and the reported experimental results on the values of H_c, H_{c2} and κ varies greatly [Kritcha et al., 1991; Mitra et al., 1989; Kang et al., 1988; Palstra et al., 1988]. Therefore, Bi(2:2:2:3) is classified as quasi 2-D anisotropic superconductor for which 3-D Hao-Clem model is not likely to be applied well. Nonetheless, we will try to use the model to extract the H_c and κ data.

The c-axis oriented Bi(2:2:2:3) sample used in this experiment was made in a form of silver wrapped tape, through a combination of drawing and rolling. Transmission electron microscopy (TEM) studies showed the high texturing of the

superconducting tape in which the c-axis of Bi(2:2:2:3) grains are aligned perpendicular to the tape surface and individual grains connect smoothly together with small angle boundaries of 6^0 or less.

The T_c of this sample determined as the intercept of the linear extrapolation of magnetization to a zero moment from M vs T data taken at 2 Oe is 107.5 K. Shown in Fig. 4.22 are the M vs T data at various fields after the background subtraction from the Curie-Weiss fittings to high temperature M vs T data, as discussed earlier. It is particularly interesting that the linear extrapolation of linear regions at various fields lead to almost the same T_c, regardless of the strength of the applied field. Therefore, determining H_{c2} from this method will lead to dH_{c2}/dT slope value of near infinity. By fitting the M vs H data to Hao-Clem equation Eq. (2.36), H_c, H_{c2} and κ_c values can be evaluated.

The attempts to fit the M vs H data to Eq. (2.36) with both H_c and κ_c as fitting variables, as in the case of YBCO magnetization data fitting, were not very satisfactory, since the κ value diverges near T_c. This is the phenomenon also noticed for YBCO samples near the T_c. However, the fact that the crossover in M vs T data occurs at much lower temperature below T_c for Bi(2:2:2:3) causes the κ_c values diverge at the temperature of crossover. Whether this is caused by the thermal fluctuation effect is not clear for the Bismuth family superconductors, because the crossover occurs typically at much lower temperature than YBCO. Recently, Bulaevskii et al. proposed a theory of the crossover for 2-D superconductors, which explains the crossover as a results of an entropy contribution to the free energy due to thermal distortions, and successfully described the magnetization curves near the crossover with the model [Bulaevskii et al., 1992].

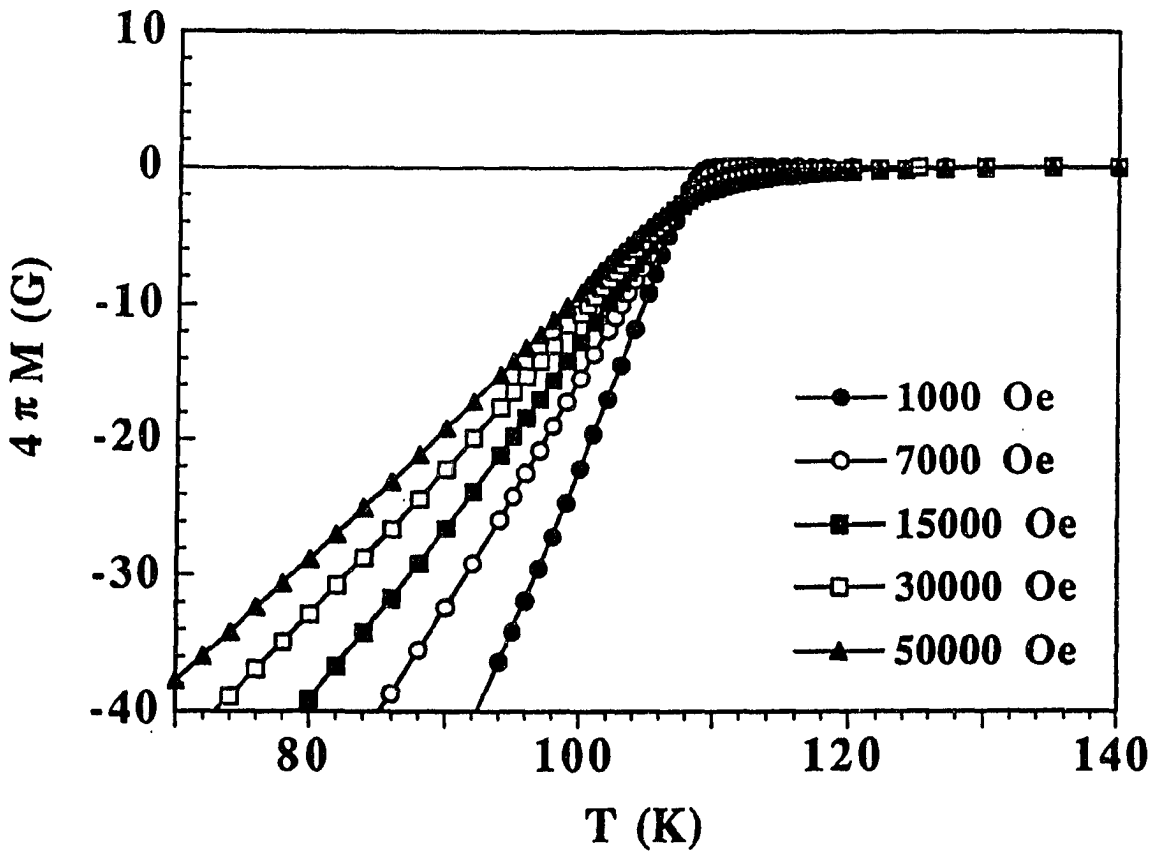

Fig. 4.22 Temperature dependence of background-subtracted magnetization of Bi(2:2:2:3) in various fields H applied to parallel to c-axis

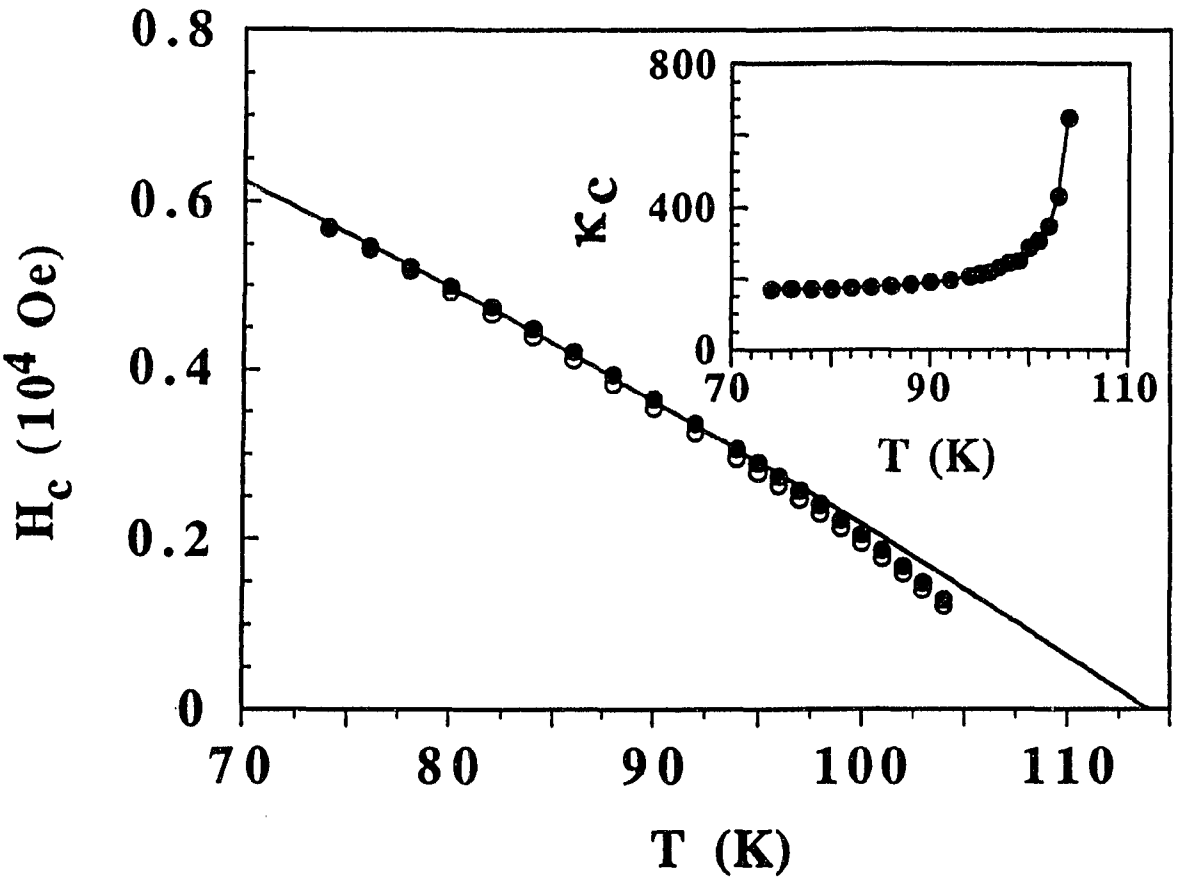

Fig. 4.23 H_c vs T for Bi(2:2:2:3) from the Hao-Clem model fit. The solid and open symbols correspond to the values derived with a constant κ_c(=170) and linearly varying κ_c respectively. The line shows a BCS fit to H_c(T) data with κ_c. The insert shows κ_c(T) data

Still, as we can see from Fig. 4.23, κ_c is nearly constant in the lower temperature region with a value of 170 at 74 K. The behavior of κ_c at higher temperature may reflect the quasi 2-D nature of the bismuth based oxide superconductor. Again, it should be pointed out that the Hao-Clem model is based on a 3-D anisotropic mean field theory which does not include the terms to count for the large scale crossover of quasi 2-D superconductors.

By using the near constant κ_c values at lower temperature region, $H_c(T)$ can be derived. We used the average value of κ_c = 170 of the temperature region between 74 and 80 K and the fitting result was plotted as solid circles in Fig. 4.23. The solid line in Fig. 4.23 shows a fit of $H_c(T)$ data to the BCS temperature dependent formula given by Clem [Clem, 1966], as shown in Eq. (4.6). The fitting yields $H_c(0) = 1.06\times10^4$ Oe with T_c =114 K. The fit is good up to around 96 K. One can easily see the discrepancy for the temperature above 100 K. This is due to the large fluctuation effect near T_c. It is also noted that the values of T_c derived here is higher than the values estimated as the superconducting onset from M vs T data with 2 Oe applied field. A similar increase in T_c from the fitting was also reported by Hao et al. [Hao et al., 1991], giving a T_c value of two degrees higher from the BCS fit of $H_c(T)$ data.

It is an interesting comparison to fit the M vs H data using the κ_c data that linearly decreases by 25 % from the value at zero temperature to T_c and gives the value of 170 at 74 K. This is equivalent to assuming the κ_c to behave similar to that of a conventional type II superconductor. The results of $H_c(T)$ data based on this set of κ_c values is shown in Fig. 4.23 as open circles. The $H_c(0)$ and T_c values from the similar BCS fitting results in $H_c(0) = 1.07\times10^4$ Oe and T_c = 112.9 K. It is noteworthy that the linearly decreasing κ_c changes $H_c(T)$ only slightly. If a

temperature dependence of $1-(T/T_c)^2$ were to be assumed for $H_c(T)$ data, $H_c(0)$ and T_c would become 1.00×10^4 Oe and 112.7 K respectively. In general all of these fittings give $H_c(0)$ results comparable to that of YBCO as calculated earlier or the result reported by Hao et al. [Hao et al., 1991], which are 1.18×10^4 Oe and 1.05×10^4 Oe.

H_{c2} can be calculated from the relation, $H_{c2} = \kappa_c\sqrt{2}H_c$ and the results are shown in Fig. 4.24., where solid circles correspond to the values obtained by using a constant value of κ_c of 107.4, and open circles represent the values from assuming κ_c linearly decreasing in temperature. Since H_{c2} is proportional to κ_c, the difference in $H_{c2}(T)$ at higher temperature region shows larger difference than $H_c(T)$. The slope, dH_{c2}/dT, calculated from the BCS fit of $H_c(T)$ yields the value of 3.68 at T_c when fixed κ_c value is assumed. The value $H_{c2}(0)$ can be evaluated from the equation [Fetter et al., 1969],

$$H_{c2} = 0.5758\left[\frac{\kappa_1(0)}{\kappa}\right]T_c\left(\frac{dH_{c2}}{dT}\right)_{T_c} \qquad (4.12)$$

where the $\kappa_1(0)/\kappa$ value is estimated as 1.26 in clean limit [Fetter and Hohenberg, 1969], and 1.20 in dirty limit [Werthamer et al.,1969]. The result gives $H_{c2}(0) = 2.97\times10^6$ Oe. The $\xi_{ab}(0)$ and $\lambda_{ab}(0)$ values can also be calculated from the equations

$$H_{c2}(0) = \frac{\varphi_0}{\pi\xi_{ab}^2(0)}, \qquad (4.13)$$

and from $\sqrt{2}H_c = \frac{\kappa\varphi_0}{2\pi\lambda^2}$. The results are $\xi_{ab}(0) = 10.5$ Å and $\lambda_{ab}(0) = 1940$ Å.

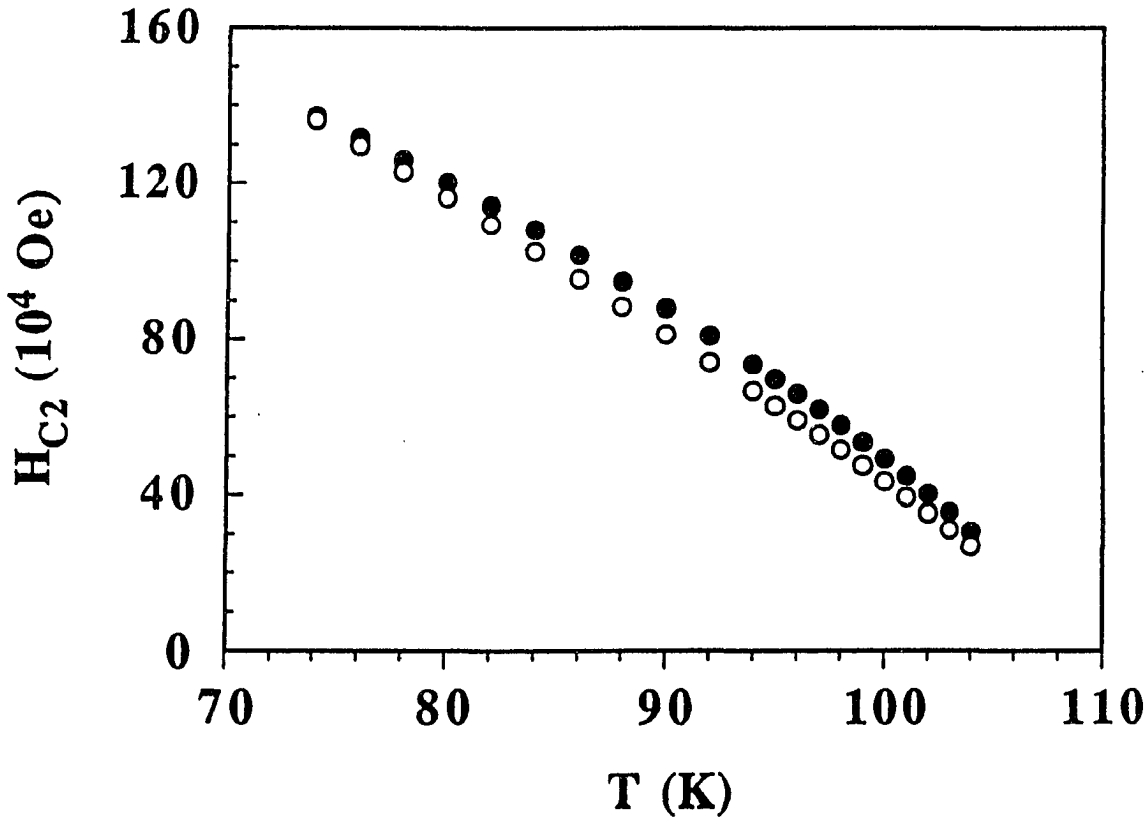

Fig. 4.24 H_{c2} vs T plots for Bi(2:2:2:3), where solid symbols correspond to the values derived with constant κ_c(=170) and open symbols represent the values with varying κ_c

Summary

Calculations of critical fields and the behavior of order parameter at various applied magnetic fields in the reversible regime have been studied for a grain-aligned YBCO sample with the orientation of H perpendicular to c. The results show the Hao and Clem's theory successfully describes M(H) data of this YBCO sample and provides accurate $\kappa_c(T)$ and $H_c(T)$ data. While Hao et al.'s initial work assumed κ_c as constant, this study also shows the temperature dependence of κ_c, which decreases linearly in temperature near T_c. The calculated $\kappa_c(T)$ values are 77.6 at 81 K with the slope of $-d\kappa_c/dT = 1.57/K$. This linear temperature dependence of $\kappa_c(T)$ is assumed for the region near T_c, and from which $H_{c2}(T)$ is determined along with the relation $\kappa_c(T) = H_{c2}(T) / \sqrt{2}H_c(T)$. The fluctuation effects on Hao-Clem model fitting to M(H) data of YBCO causes $\kappa_c(T)$ to diverge at the temperature region near 91.5 K where the crossover in M(H) occurs due to the increasing fluctuational diamagnetism. Similar phenomenon for the BSCCO(2:2:2:3) magnetization data is reported elsewhere [Li et al., 1992]. The better agreement between the Hao-Clem model and M(H) data for YBCO than for the BSCCO(2:2:1:2, 2:2:2:3) [Kes et al., 1991; Li et al., 1992] is considered to be related to the fact that the Hao-Clem model is based on 3-D model, for which YBCO is better qualified. Similar fittings for BSCCO(2:2:2:3) showed signs of strong fluctuational effect even 10 K below T_c [Li et al., 1992], which clearly shows the limitation of applying Hao-Clem model in describing the reversible magnetization of these superconductors. Still, we have shown that when used in the lower temperature region, fitting the magnetization data of Bi(2:2:2:3) to this model can lead to reasonably good results.

The order parameter function used in the Hao-Clem model is a trial function for a variational approach to the Ginzburg-Landau theory. While a trial function for this purpose isn't necessarily the one that provides microscopically accurate order parameter function, its spatial average behavior is in good agreement with the numerical solution of Ginzburg-Landau equations. Therefore, suppression of the average order parameter presented in this study provides reasonable values within the framework of Ginzburg-Landau theory. The results of this study provide the first available information of the behavior of order parameter along with the temperature dependent κ_c values, under the given temperature and the applied field, based on the measured magnetization data.

4.4 Grain Size Effect on Magnetization

Magnetization measurements were done on grain-aligned YBCO samples that were made by varying the final sintering temperature, as discussed earlier in Chapter 3. Four samples with different average grain sizes, which we will call as YBCO_A, B, C, D, have average grain sizes of 3.3, 12.7, 26.8 and 37.5 μ respectively.

It has been known that average twin spacing, d, of YBCO changes with its average grain size, D [Shaw et al., 1988; Chumbley et al., 1989], according to the equation of the form, suggested by Arlt et al. [Arlt et al., 1985] as

$$d = \sqrt{\frac{128\pi\gamma D}{ES^2}} \qquad (4.14)$$

where γ is the twin boundary energy per unit area associated with the creation of a twin plane, S is the orthorhombicity (which is defined as S = a/b - 1), and E is the elastic modulus of the material. Therefore, the twin spacing is expected to decrease as the square root of the grain size. Shaw et al. and Chumbley et al. also observed that the expected square root dependency of twin spacing on the average grain size indeed agrees qualitatively in their extensive polarized light microscopy and transmission electron microscopy (TEM) studies. Fig. 4.25 shows the results of relationship between the average twin spacing and the average grain size from Shaw et al.'s data. The error bars indicate the grain to grain variation in twin spacings observed in one sample. As one can see from the graph, considerable scatter is evident especially for the larger grain size samples. This enhanced variation in grain/twin spacing for the larger average grain size sample is also noticed in our 4 batches of samples in figures 3.4 and 3.5. Based on these results the average grain sizes of the samples in this work can be estimated as shown in the following Table 4.1.

Table 4.1. Estimated average twin spacing of YBCO samples

Sample ID	Average grain size (μ)	Average twin spacing (nm)
YBCO_A	3.3	45
YBCO_B	12.7	120
YBCO_C	26.8	180
YBCO_D	37.5	210

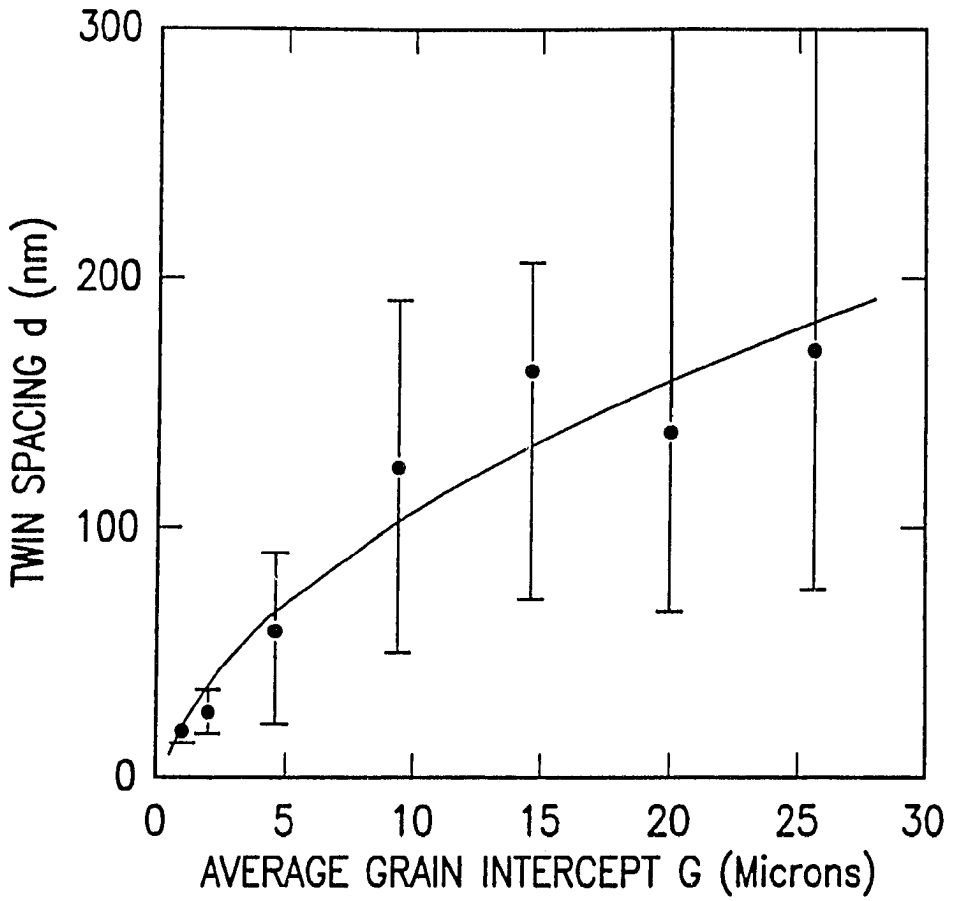

Fig. 4.25 Variation in twin spacing (d) with grain size (G). The line shows a fit of $d \propto \sqrt{G}$ [Shaw et al., 1989]

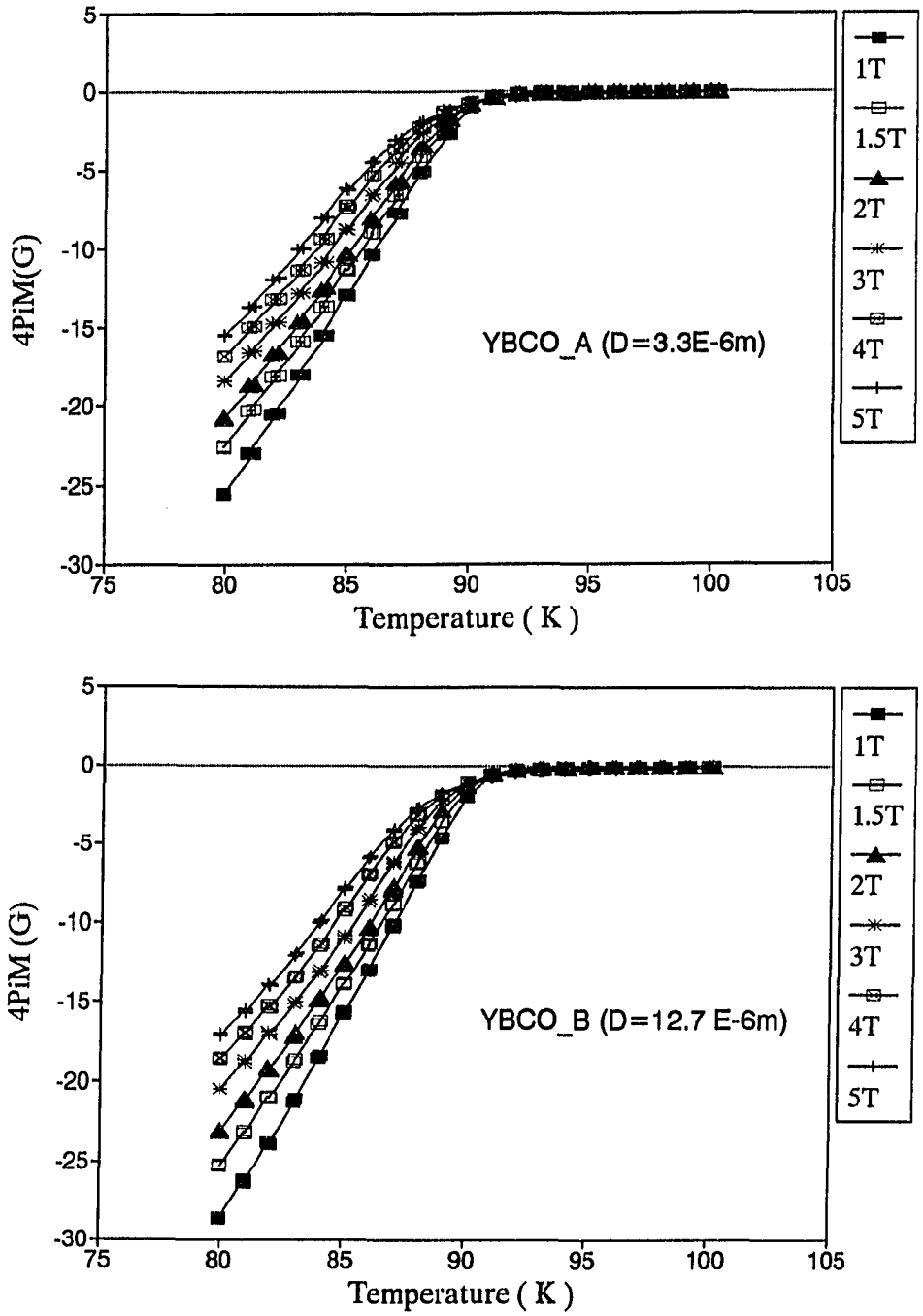

Fig. 4.26 (a) A comparison of the high field (H ≥ 1 T) M vs T data for YBCO_A (top), and YBCO_B (bottom)

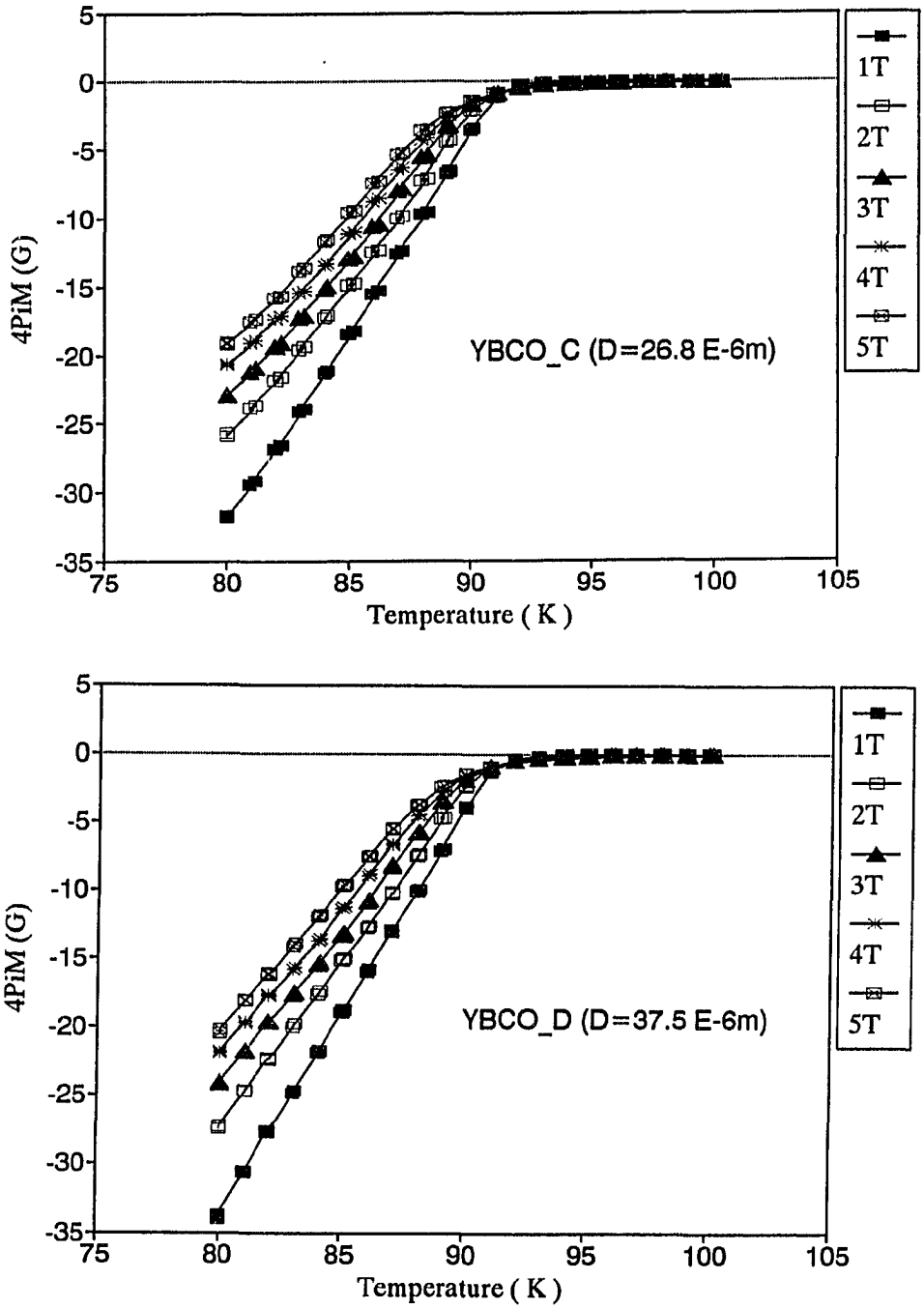

Fig. 4.26 (continued) (b) A comparison of the high field (H ≥ 1 T) M vs T data for YBCO_C (top), and YBCO_D (bottom)

The high field (H≥ 1 T) portion of M vs T measurement results are shown in figures 4.26a-b for above samples. The magnetization data show increased magnetization values for the larger grain size samples. The T_c also show slight decrease (≅ 0.5°) for the smaller grain size sample between the smallest (3.3 μ) and the largest (37.5 μ) average grain size samples. The smallest grain size sample shows poor grain alignment, since its extremely small grains include grains with sizes of less than 3 μ and even some sub micron sized grains.

Unfortunately, the sample cannot be ground to a smaller average grain size than several μ for better grain alignment, due to the fact that the penetration depth increases to the order of 1μ near T_c and most of the sample volume becomes 'transparent' to the applied magnetic field. Therefore, only the magnetization data for three large samples excluding the smallest average grain size sample have been used in calculating specific heat jumps.

Grain Size Effect on Free-Energy and Specific Heat Jump

Shown in Fig. 4.27a and 4.27b are free-energy surfaces G(H)-G(0) of the three YBCO samples with different grain sizes, calculated by integrating the M(H) data following Eq. (2.2), for H=3 and 5 T respectively. The G(H)-G(0) values show about 15 % decrease for YBCO_B (D_{av}=12.7 μ) compared to YBCO_D (D_{av}=37.5 μ) at T=80 K. The onset temperature of G(H)-G(0).is also lowered by about 0.3 degree for the smaller grain sample between the two. This agrees with the decrease in T_c between the two samples as discussed in Chapter 3. The origin of this decrease in T_c for the smaller grain seize sample, however, is not clear at the moment. On the contrary, the smaller grain sample is more easily oxygenated, and the fact that T_c of a grain-aligned YBCO sample is typically higher than a large single crystal is

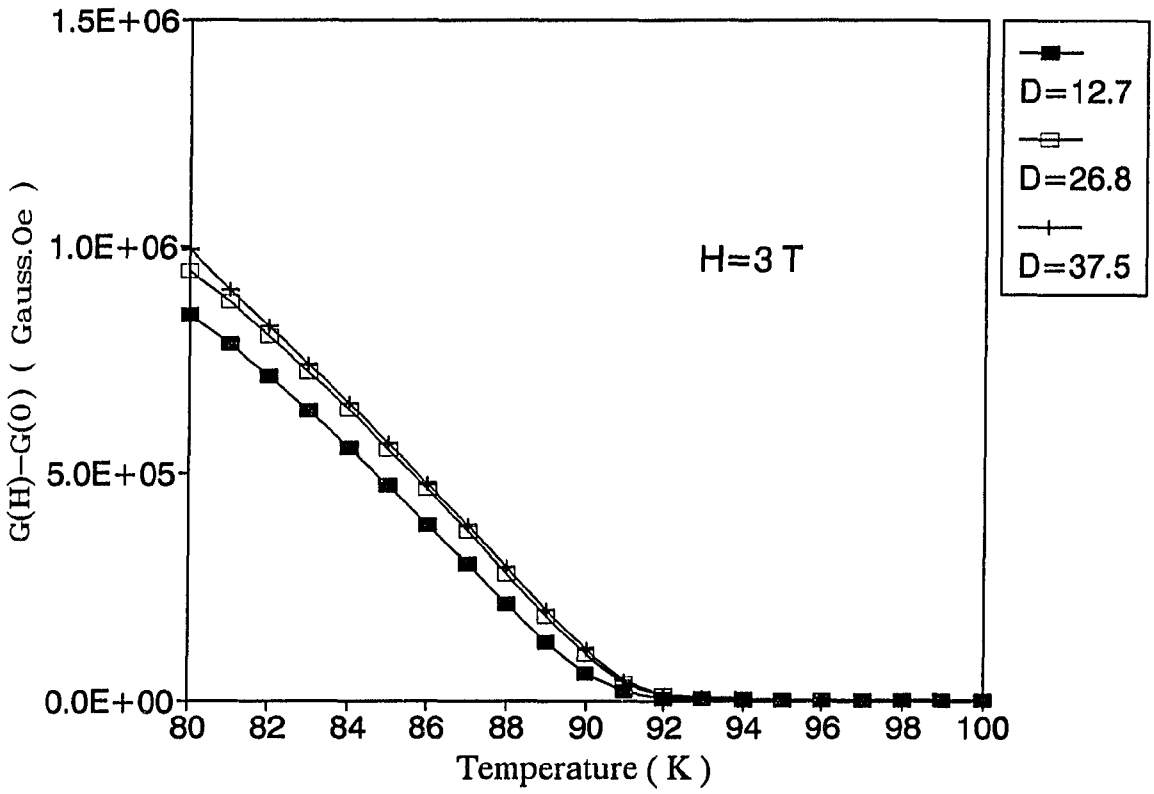

Fig. 4.27 (a) Comparison of free energy surface curves for samples with varying average grain sizes at H = 3 T

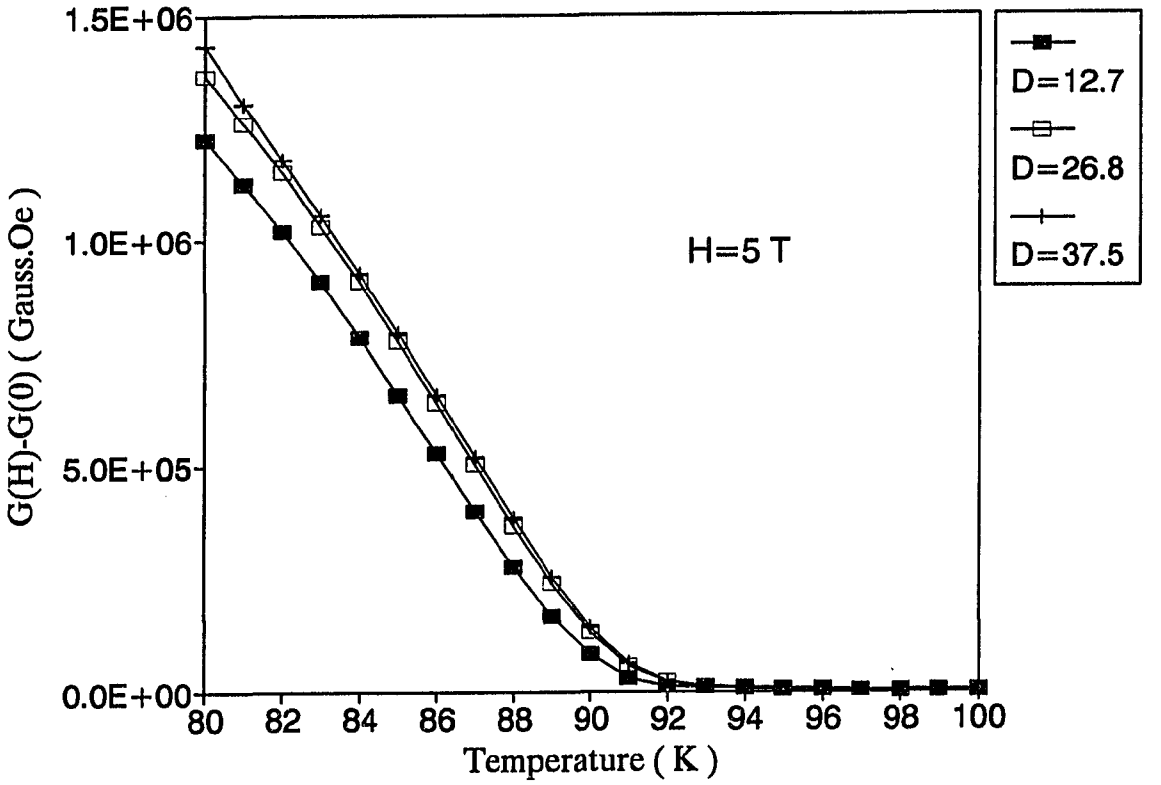

Fig. 4.27 (continued) (b) Comparison of free energy surface curves for samples with varying average grain sizes at H = 5 T

supposed to be caused by this ease in full oxygenation. This isn't the case for these four samples with varying average grain sizes.

The specific heat jump data can be calculated from the thermodynamic relation give by Eq. (2.4), and some of the high field results for the three samples are shown in Fig. 4. 28a-c for the comparison. As expected from the free energy data, onset temperature of the specific heat jump is also lower for smaller grain samples and the temperature for peak of the specific heat jump also moves to the lower temperature. While it is not significant, the specific heat jump values are smaller for the YBCO_C (D_{av}=26.8 μ) than YBCO_D. And for YBCO_B, the decrease in the peak value of specific heat jump is about 20 % from that of YBCO_D.

The decrease in C(0)-C(H) as well as G(H)-G(0) in the smaller grain sample is expected to reflect the following factors.. First of all, we can consider the effect of twin spacing on the order parameter. Since the twin boundaries work as pinning sites, the order parameter gets reduced in the twin boundaries. Therefore, a sample with narrower twin spacing causes the average order parameter to decrease and the free energy gets reduced as the twin spacing gets smaller.

Secondly, the grain size effect due to the increasing penetration depth of YBCO near T_c can also cause the G(H)-G(0) value appear smaller for the smaller grain size sample, because more % volume of smaller-grain sample will fall into the surface volume and becomes 'transparent' to magnetic field as the penetration depth becomes comparable to the size of the grain near T_c. A rough estimation predicts this effect becomes significant enough to alter the magnetization value around several degrees below T_c, since the penetration depth increases to be about 0.5 μ at 89 K, as shown in Fig. 4.29, from the Hao-Clem model calculation results

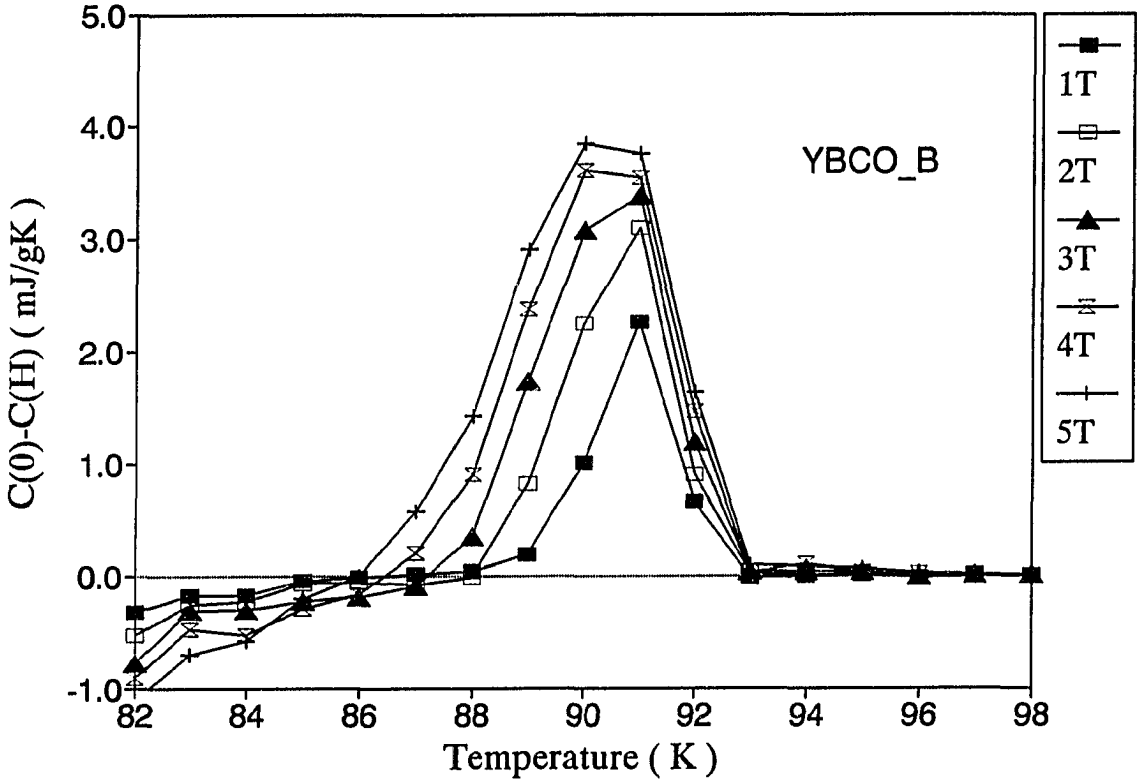

Fig. 4.28 (a) Specific heat jump C_0-C_H vs T curves for YBCO_B (D_{av} = 12.7μ)

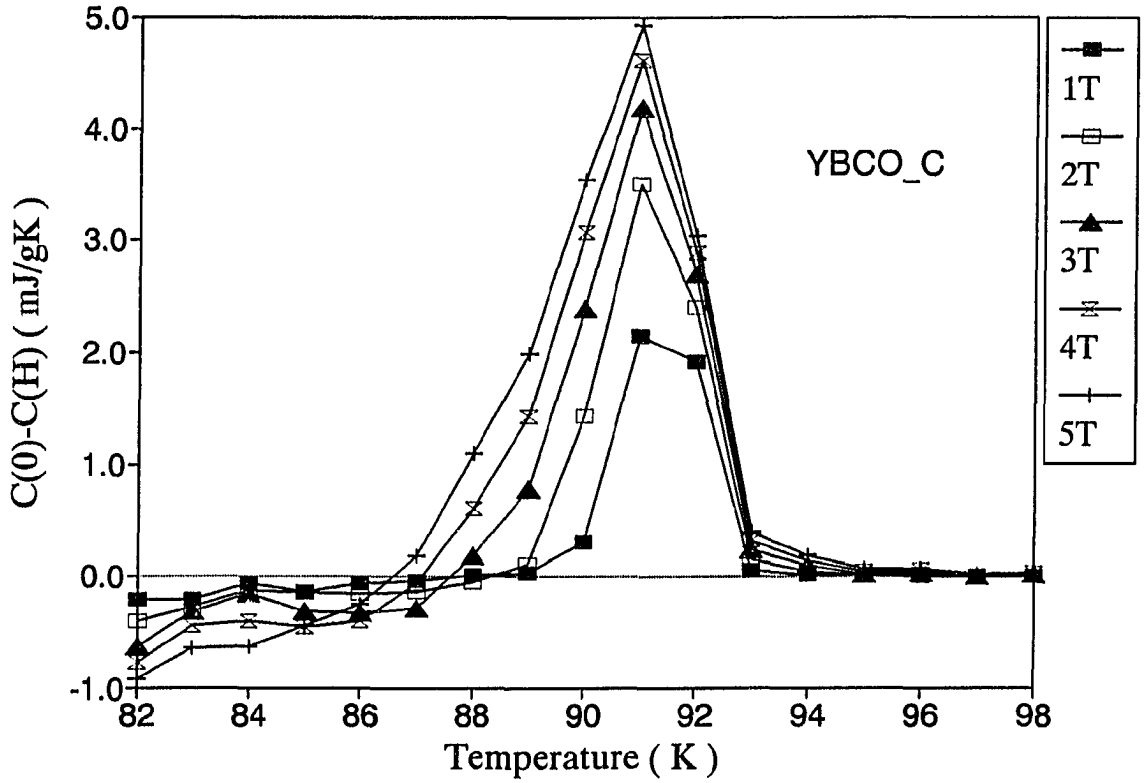

Fig. 4.28 (continued) (b) Specific heat jump C_0-C_H vs T curves for YBCO_C (D_{av} = 26.8μ)

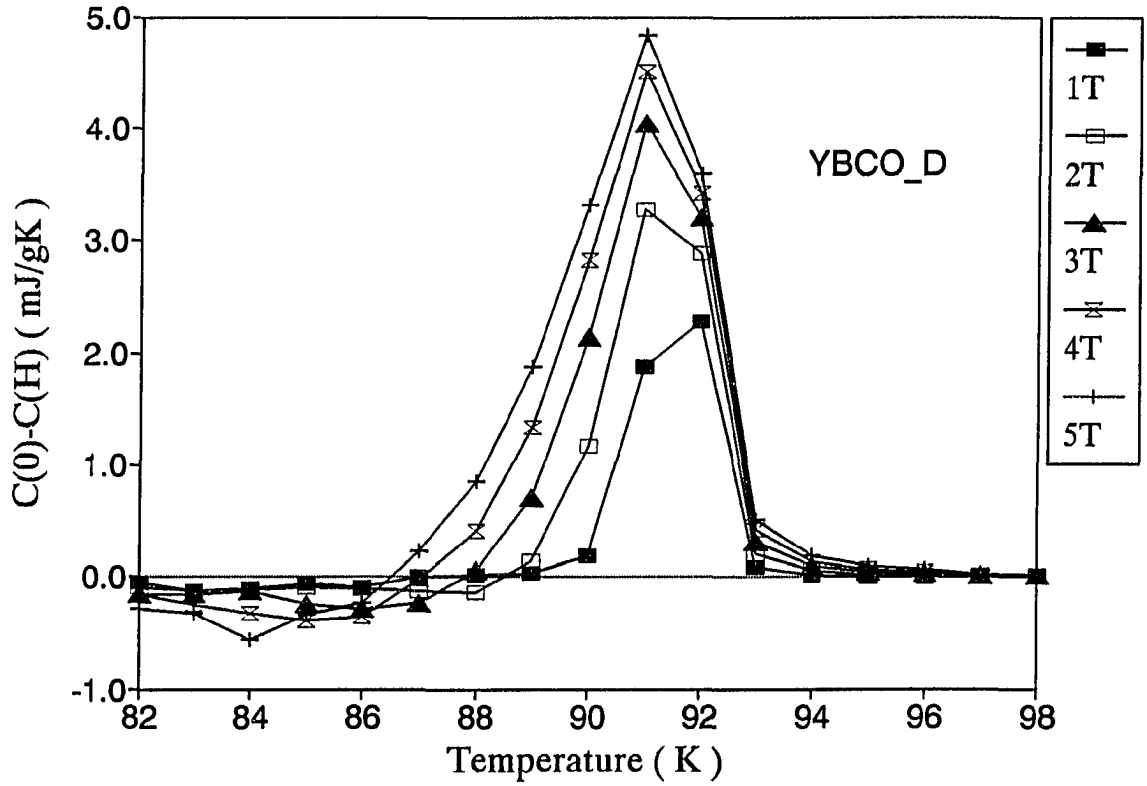

Fig. 4.28 (continued) (c) Specific heat jump C_0-C_H vs T curves for YBCO_D (D_{av} = 37.5μ)

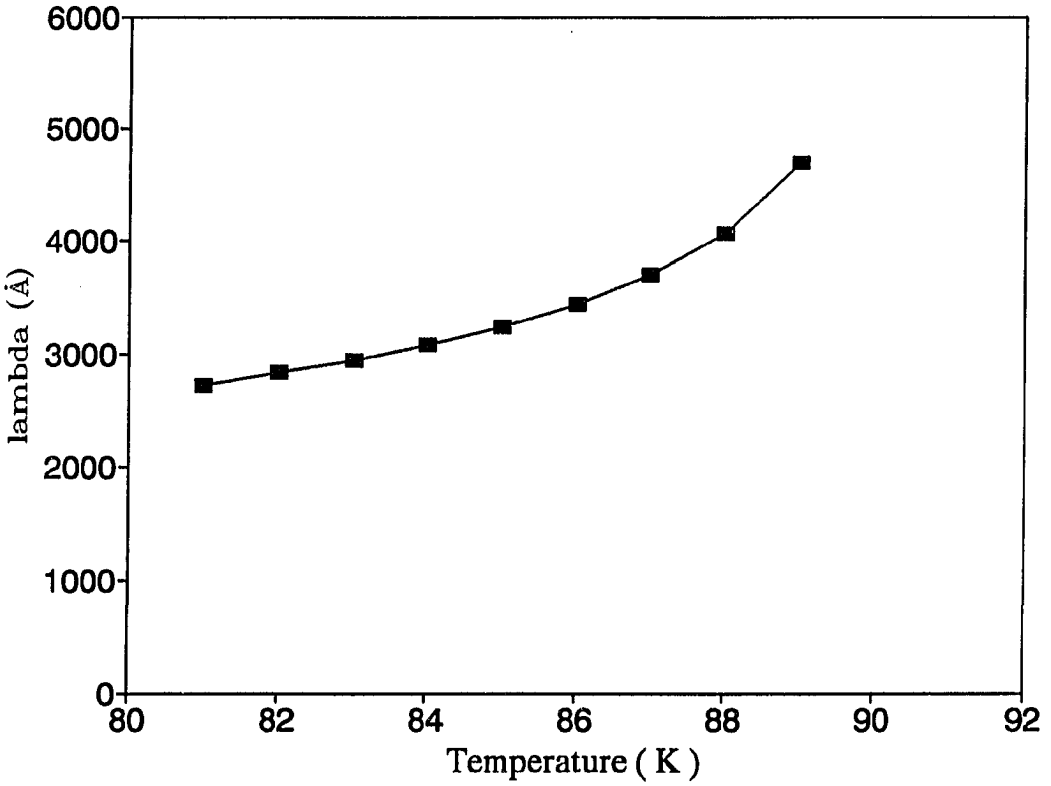

Fig. 4.29 Penetration depth λ_{ab} vs T plot from the Hao-Clem model fitting

in the earlier section.

Unfortunately, the results from this experiment alone cannot single out individual contributions from each of these factors. However, for the average grain sizes of the samples used in this experiment (the smallest being 12.7 μ) the effect from the twin spacing is believed to be the dominant factor.

CHAPTER 5. CONCLUSIONS

In this thesis, results from a series of studies on the magnetic properties of high-T_c superconductors have been presented. The main results of this work can be summarized as follows.

The curvature in magnetization vs. temperature data reflects the thermodynamic fluctuation near T_c. The thermodynamic reversibility holds in this temperature region and the specific heat jumps can be calculated from free energy curves. The effect of an applied field on the specific heat jump is to suppress its magnitude of it rather than suppressing its onset temperature. In the low temperature region of below 86 K, the specific heat is independent of magnetic field.

A comparative study of the grain-aligned YBCO and the melt-textured YBCO shows their free energy and specific jump values are about the same in spite of their quite different material structure and pinning strength. Calculations of effective pinning potentials from the Beasley model also agrees between the two materials.

Critical fields and temperature dependence the order parameter have been estimated by fitting the magnetization data to Hao and Clem's variational solution for the Ginzburg-Landau equation in the intermediate field region. It has been shown that taking the Ginzburg-Landau parameter κ as the second variable of the fitting rather than assuming it to be a constant provides physically preferable results in many aspects. The temperature dependence of κ in this region turned

out to be a linearly decreasing function of the temperature, which qualitatively agrees with Maki's results in the conventional superconductors.

The spatial averages of the order parameter have been calculated based on the Hao-Clem model and its behavior at various temperatures and magnetic fields has been presented in this study. The spatial average of the order parameter at 84 K and 5 T is still about 65 % of the value at T = 0, H = 0. In the order parameter vs. reduced field plot, a series of M(H) data for the different temperature values fall into a universal curve which shows a negative curvature at higher field region and a much larger positive curvature at the narrow low end field region. This is in qualitative agreement with E. H. Brandt's extreme type-II ($\kappa >> 1$) order parameter calculation.

The grain size effects on magnetization have been studied with the grain-aligned YBCO samples of various average grain sizes. The free energy gets lowered as the average grain size D decreases. As a result, the specific heat jump also decreases for the smaller grain size samples. The change in the twin spacing d, that has been known to depend on the grain size D by $d \propto \sqrt{D}$, is believed to be the main reason for the change in the free energy.

REFERENCES

A. A. Abrikosov, Zh. Eksp. Teor. Fiz. **32**, 1442 (1957).

P. W. Anderson, Phys. Rev. Lett. **9**, 309 (1962).

P. W. Anderson and Y. B. Kim, Rev. Mod. Phys. **36**, 39 (1964).

G. Arlt, D. Hennings, and G. de With, J. Appl. Phys. **58**, 1619 (1985).

K. S. Athreya, O. B. Hyun, J. E. Ostenson, J. R. Clem, and D. K. Finnemore, Phys. Rev. B **38**, 11846 (1988).

J. Bardeen, L. N. Cooper, and J. R. Schrieffer, Phys. Rev. **108**, 1175 (1957).

C. P. Bean, Phys. Rev. Lett. **8**, 250 (1962); Rev. Mod. Phys. **36**, 31 (1964).

C. P. Bean, Phys. Rev. Lett., **62**, 2857 (1989).

M. R. Beasley, R. Labusch, and W. W. Webb, Phys. Rev. **181**, 682 (1969).

J. G. Bednorz and K. A. Müller, Z. Phys. B **64**, 189 (1986).

M. A. Beno, L. Soderholm, D. W. Capone II, D. G. Hinks, J. D. Jorgensen, J. D. Grace, and I. K. Schuller, Appl. Phys. Lett. **51**, 57 (1987).

E. H. Brandt, Phys. Stat. Sol. **51**, 345 (1972).

L. N. Bulaevskii, M. Ledvij, and V. G. Kogan, preprint.

C. Caroli, M. Cyrot, and P. G. de Gennes, Solid State Commun. **4**, 17 (1966).

L. S. Chumbley, J. D. Verhoeven, M. R. Kim, A. L. Cornelius, and M. J. Kramer, IEEE MAG. **25**, 2337 (1989).

J. R. Clem, Ann. Phys. (N.Y.) **40**, 268 (1966).

J. R. Clem, Phys. Rev. B **43**, 7837 (1991).

P. G. de Gennes, *Superconductivity of Metals and Alloys*, (Benjamin, New York, 1966).

G. Eilenberger, Phys. Rev. **153**, 584 (1967).

M. M. Fang, J. E. Ostenson, D. K. Finnemore, D. E. Farrell, and N. P. Bansal, Phys. Rev. B **39**, 222 (1989).

D. E. Farrell, S. Bonham, J. Foster, Y. C. Chang, P. Z. Jiang, K. G. Vandervoot, D. J. Ram, and V. G. Kogan,Phys. Rev. Lett. **63**, 782 (1989).

D. E. Farrell, B. S. Chandrasekhar, M. R. DeGuire, M. M Fang, V. G. Kogan, J. R. Clem, and D. K. Finnemore, Phys. Rev. B **36**, 4025 (1987).

A. L. Fetter and P. C. Hohenberg, in *Superconductivity*, edited by R. D. Parks (Marcel Dekker, New York, 1969), p. 817.

R. A. Fisher, S. Kim, S. E. Lacy, N. E. Philips, D. E. Morris, A. G. Markelz, J. Y. T. Wei, and D. S. Ginley, Phys. Rev. B **38**, 11942 (1988).

R. M. Fleming, L. F. Schneemeyer, P. K. Gallagher, B. Batlogg, L. W. Rupp, and J. V. Waszczak, Phys. Rev. B **37**, 7920 (1988).

D. M. Ginsberg, in *Physical Properties of High Temperature Superconductors I*, edited by D. M. Ginsberg (World Scientific, Singapore, 1989), Vol. 1, chapter 1.

V. L. Ginzburg and L. D. Landau, Zh. Eksp. Teor. Fiz. **20**, 1064 (1950).

Junho Gohng and D. K. Finnemore, Phys. Rev. B **42**, 7946 (1990).

L. P. Gor'kov, Zh. Eksperim. i Teor. Fiz. **36**, 1918 (1959) [Soviet Phys. - JETP **9**, 1364 (1959)].

J. E. Greedan, A. H. O'Reilly, and C. V. Stager, Phys. Rev. B **35**, 8770 (1987).

P. Haldar, K. Chen, B. Maheswaran, A. Roig-Janicki, N. K. Jaggi, R. S. Markiewicz, and B. C. Giessen, Science **241**, 1198 (1988).

Zhidong Hao and John R. Clem, Phys. Rev. Lett. **67**, 2371 (1991).

Zhidong Hao, John R. Clem, M. W. McElfresh, L. Civale, A. P. Malozemoff, and F. Holtzberg, Phys. Rev. B **43**, 2844 (1991).

J. -L. Hodeau, P. Bordet, J. -J. Capponi, C. Chaillout, and M. Marezio, Physica C **153-155**, 582 (1988).

O. B. Hyun, S. C. Sanders, and D. K. Finnemore, J. Supercond. **2**, 529 (1989).

S. E. Inderhees, M. B. Salamon, J. P. Rice, and D. M. Ginsberg, Phys. Rev. Lett. **66**, 232 (1991).

S. Jin, R. Sherwood, E. Gyorgy, T. Tiefel, R, van Dover, S. Nakahara, L. Schneemeyer, R. Fastnacht, M. Davis, Appl. Phys. Lett. **54**, 584 (1989).

S. Jin, T. Tiefel, R. Sherwood, R. van Dover, M. Davis, G. Kammlott, R. Fastnacht, Phys. Rev. B, **37**, 7850 (1988).

J. H. Kang, R. T. Kampwirth, and K. E. Gray, Appl. Phys. Lett. **52**, 2080 (1988)

Y. B. Kim, C. F. Hempstead, and A. R. Strnad, Phys. Rev. Lett. **9**, 306 (1962).

Y. B. Kim, C. F. Hempstead, and A. R. Strnad, Phys. Rev. **129**, 528 (1963).

P. H. Kes, J. Aarts, V. M. Vinokur, and C. J. van der Beek, Phys. Rev. Lett. **64**, 1063 (1990).

V. G. Kogan, M. M. Fang, and S. Mitra, Phys. Rev. B **38**, 11958 (1988).

W. Kritscha, F. M. Sauerzopf, H. W. Weber, G. W. Crabtree, Y. C. Chang, and P. Z. Jiang, Physica C **179**, 59 (1991).

Y. Kubo, T. Ichihashi, T. Manako, K. Baba, J. Tabuchi, and H. Igarashi, Phys. Rev. B 37, 7858 (1988).

J. Kurkijärvi, V. Ambegaokar, and G. Eilenberger,Phys. Rev. B **5**, 868 (1972).

M. D. Lan, J. Z. Liu, P. Klavins, R. N. Shelton, (1991 APS March Meeting).

W. C. Lee, R. A. Klemm, and D. C. Johnson, Phys. Rev. Lett. **63**, 1012 (1988).

P. A. Lee and M. G. Payne, Phys. Rev. Lett. **26**, 1537 (1971).

Q. Li, M. Suenaga, J. Gohng, D. K. Finnemore, T. Hikata, and K. Sato., preprint.

K. S. Lichtenberger, Ph.D. Thesis, Iowa State University, 1991.

F. London and H. London, Proc. Roy. Soc. (London) **A149**, 71 (1935).

H. Maeda, Y. Tanaka, M. Fukutomi, and T. Asano, Japan. J. Appl. Phys. **27**, L209 (1988).

D. E. Mapother, Phys. Rev. **126**, 2021 (1962).

S. Martin, A. T. Fiory, R. M. Fleming, G. P. Espinosa, and A. S. Cooper, Phys. Rev. Lett. **62**, 677 (1989).

P. J. McGinn, W. Chen, and N. Zhu, To be published in Journal of Metals.

P. J. McGinn, *High-Temperature Superconductivity*, edited by John J. Pouch et al. (Trans Tech Pub., Aedermannsdorf, Switzerland, 1992)

W. Meissner and R. Ochsenfeld, Naturwissenschaften **21**, 787 (1933).

S. Mitra, J. H. Cho, W. C. Lee, D. C. Johnston, and V. G. Kogan, Phys. Rev. B **40**, 2674 (1989)

Bernhard Mühlschlegel, Z. Physik **155**,313 (1957).

K. A. Muller, M. Takashige, and J. G. Bendorz, Phys. Rev. Lett., **58**, 1143 (1987).

M. J. Naughton, R. C. Yu, P. K. Davies, J. R. Fisher, R. V. Chamberlin, Z. Z. Wang, T. W. Jing, N. P. Ong, and P. M. Chaikin, Phys. Rev. B **38**, 9280 (1988).

K. No, J. D. Verhoeven, R. W. McCallum, and E. D. Gibson, IEEE MAG. **25**, 2184 (1989).

H. Kamerlingh Onnes, Leiden Comm. **120b, 122b, 124c** (1911)

T. T. M. Palstra, B. Batlogg, L. F. Schneemeyer, R. B. van Dover, and J. V. Waszczak, Phys. Rev. B **38**, 5102 (1988).

A. B. Pippard, *Elements of Classical Thermodynamics* (Cambridge University Press, Cambridge, 1960).

R. E. Prange, Phys. Rev. B **1**, 2349 (1970).

D. Saint-James, E. J. Thomas, and G. Sarma, *Type II Superconductivity*, (Pergamon Press, London, 1969), p. 15.

M. B. Salomon, S. E. Inderhees, J. P. Rice, B. G. Pazol, D. M. Ginsberg, and N. Goldenfeld, Phys. Rev. B **38**, 885 (1988).

S. C. Sanders, O. B. Hyun, and D. K. Finnemore, Phys. Rev. B **42**, 8035 (1990).

P. Sevdlindh, C. Rossel, K. Niskanen, P. Norling, P. Nordblad, L. Lundgren, and G. V. Chandrashekhar, Physica C **176**, 176 (1991).

T. M. Shaw, S. L. Shinde, D. Dimos, R. F. Cook, P. R. Duncombe, and C. Kroll, J. Mater. Res. **4(2)**, 248 (1989).

Z. Z. Sheng and A. M. Hermann, Nature, **332**, 55 (1988).

M. Suenaga, A. K. Ghosh, Youwen Xu, and D. O. Welch, Phys. Rev. Lett., **66**, 1777 (1991).

J. R. Thompson, Yang Ren Sun, F. Holtzberg, Phys. Rev. B **44**, 458 (1991).

M. Tinkham, *Introduction to Superconductivity*, (McGraw-Hill, New York, 1975), p. 246.

G. Triscone, A. Junod, and J. Muller, Physica C **162-164**, 470 (1989)

M. Tuominen, A. M. Goldman, Y. Z. Chang, and P. Z. Jiang, Phys. Rev. B **42**, 412 (1990).

S. T. Weir, W. J. Nellis, Y. Dalichaouch, B. W. Lee, M. B. Maple, J. Z. Liu, and R. N. Shelton, Phys. Rev. B **43**, 3034 (1991).

U. Welp, W. K. Kwok, G. W. Crabtree, K. G. Vandervoort, and J. Z. Liu, Phys. Rev. Lett. **62**, 1908 (1989).

U. Welp, S. Fleshler, W. K. Kwok, K. G. Vandervoot, J. Downey, B. Veal, and G. W. Crabtree, Physical Phenomena at High Magnetic Field Conference at Florida State University (1991).

N. R. Werthamer, E. Helfand, and P. C. Hohenberg, Phys. Rev. **147**, 295 (1966).

M. K. Wu, J. R. Ashburn, C. J. Torng, P. H. Hor, R. L. Meng, L. Gao, Z. J. Huang, Y. Q. Wang, and C. W. Chu, Phys. Rev. Lett. **58**, 908 (1987).

Ming Xu, Donglu Shi, and Ronald F. Fox, Phys. Rev. B **42**, 10773 (1990).

Ming Xu, Donglu Shi, A. Umezawa, K. G. Vandervoort, and G. W. Crabtree, Phys. Rev. B **43**, 13049 (1991).

Youwen Xu, M. Suenaga, A. R. Moodenbaugh, and D. O. Welch, Phys. Rev. B **40**, 10882 (1989).

Y. Yeshurun and A. P. Malozemoff, Phys. Rev. Lett. **60**, 2202 (1988).

ACKNOWLEDGMENTS

I express my deepest gratitude to professor Douglas K. Finnemore for his guidance and encouragement. He has been a teacher in life as well as in science throughout my graduate school years. I also thank Jerry Ostenson for his help and valuable comments in the experiments. I would like to extend my thanks to Okbae Hyun for his help and advice in sample preparations, and for his friendship. I thank Ming Xu for the useful discussions we shared, Steve Sanders, Qiang Qian, Qiang Li, Karl Lichtenberger, and Junghyun Sok for their friendship and aids in various occasions.

I am thankful to my parents for their love and support. Although my mother passed away during my first year in graduate school, her prayers have been guiding me always. I thank my lovely wife Jonghwa, who probably deserves more credit than I do for this work, for her love and friendship. This work wouldn't have been possible without her encouragement and generous support.

Finally, I thank our heavenly father for allowing me to meet all these wonderful people, and for his abundant love.

This work was performed at Ames Laboratory under contract No. W-7405-ENG-82 with the U. S. Department of Energy. The United States government has assigned the DOE Report number IS-1625 to this thesis.